EUROPEAN AVIATION SAFETY AGENCY
AGENCE EUROPÉENNE DE LA SÉCURITÉ AÉRIENNE
EUROPÄISCHE AGENTUR FÜR FLUGSICHERHEIT

Research Project EASA.2010/2

CODAMEIN - Composite Damage Metrics and Inspection (high energy blunt impact threat)

easa.europa.eu

CODAMEIN

Composite **Da**mage **Me**trics and **In**spection

EASA.2010.C13

Final Report

Zoltan Mikulik and Peter Haase

12 March 2012

Bishop GmbH - Aeronautical Engineers
Blankeneser Bahnhofstraße 12
22587 Hamburg – Germany

Table of contents

List of figures

List of tables

List of acronyms

ACI	Airports Council International
ADL	Allowable Damage Limit
AMC	Acceptable Means of Compliance
BVID	Barely Visible Impact Damage
CAD	Computer -aided Design
CAE	Computer-aided Engineering, (Abaqus CAE: Abaqus Pre/Post-Processor)
CDT	Critical Damage Threshold
CFRP	Carbon Fibre Reinforced Plastics
CODAMEIN	Composite Damage Metrics and Inspection
CS	Certification Specification
DBH	Internal Naming of Bishop GmbH Engineering Drawings
DITS	Dynamic Impact Test System
EASA	European Aviation Safety Agency
FE/FEA	Finite Element / Finite Element Analysis
LVDT	Linear Variable Differential Transformer
NDT	Non-distructive Testing
OEM	Original Equipment Manufacturer
SHM	Structural Health Monitoring
ST	Shear Tie
UCSD	University of California San Diego
XWB	Extra Wide Body

Acknowledgements

This work was funded by European Aviation Safety Agency (EASA) under contract EASA.2010.C13 The research was supervised by Dr Simon Waite who provided technical guidance throughout the project.

The authors would like to express their gratitude to A. Prof. Hyonny Kim and Gabriella DeFrancisci of University of California San Diego whose invaluable technical contribution was critical for the success of this project. The support of Mike Stuart of Cytec is also acknowledged.

Finally, thank you to all EASA / FAA workshop and the CMH-17 Europe participants for their scientific comments and industry perspective inputs. Feedback received from Dr Mostafa Rassaian of Boeing Co. and Chantal Fualdes of Airbus is greatly appreciated.

Executive summary

The main objective of the research described in this report was to improve the understanding of high energy low velocity blunt impact damage on a representative aircraft structure. The simulated impact scenario represented a typical incident occurring during aircraft ground service operations.

A comprehensive literature review of existing CS-25 aircraft served as a foundation for establishing scale and complexity of a representative design of a hybrid composite-metallic fuselage panel. Design details were harmonised with the FAA / Industry / University joint research led by the University of California San Diego. The manufactured test panel consisted of five aluminium frames and four stringers.

An additional survey of the literature related to ground damages caused to aircraft at airports (e.g. during ground handling operations) assisted in establishing realistic impact conditions, such as vehicle mass and velocity, which provided the associated impact energy levels. According to this, a velocity of 1 m/s is common for a vehicle 1 m away from the fuselage. At the close vicinity, an approaching velocity of approximately 0.5 m/s was reported. Reasonable energy boundaries for a high energy blunt impact were found to be in a range between 1000 J - 3000 J.

The test fixtures for quasi-static tests were developed based on the results of numerical analyses of the test panel finite element models and the full fuselage barrel model. The numerical simulations clearly showed the requirement for flexible attachment of the panel in order to account for deformation of the surrounding barrel structure. The test program involved one test panel subjected to three load cycles, progressively increasing the maximum impactor displacement. Initialization of the damage occurred at the radius of the central shear and the associated failure initiation energy threshold was calculated to be 1270 J. With the subsequent load cycles, widespread delaminations formed in several locations which consequently resulted in a severe loss of load carrying capacity of the panel and a sudden fracture of five shear ties. After unloading, a visual examination of the outer skin side showed no apparent signs of impact.

The outcomes of this research demonstrated a potentially significant safety threat of high energy low velocity blunt impact on composite aircraft fuselages which may cause extensive internal structural damage with low detectability when performing visual inspection of the external surface. Based on the findings of this research, recommendations for amending airworthiness certification specifications EASA CS-25 (large aircraft) for composite fuselages are proposed.

1 Introduction

1.1 Background

Advanced carbon fibre reinforced polymer composite materials are now being used more extensively in the aerospace industry. The high stiffness to weight ratio and fatigue resistance make carbon fibre composites suitable for both military and large civil aircraft. One of the most important issues in changing from conventional metallic alloys to composite materials is to ensure that there are no compromises in the level of safety. Aircraft certification requires demonstration of the capacity of structures with manufacturing flaws and structures damaged during aircraft service to carry loads as described in AMC 20-29, with scheduled inspections as appropriate. One specific area of interest is the blunt impact of ground vehicles with an aircraft's fuselage and the boundary between Category 2/3 damages (of Certification interest) and Category 5 damages (which should be obvious, reported and outside the immediate Certification process).

The aviation industry has acknowledged the risks associated with serious ground operation incidents and accidents. Consequences of these events result in aircraft damage, delays and financial cost to the industry. Direct costs are those related to the actual cost of repairing the damage and indirect costs include lost revenue, lost work time, disruption of the flight schedule and consequent negative customer feedback. In 2000, the Airports Council International (ACI) reported that US$3 billion in losses were caused by airport ground vehicles hitting aircraft, hitting each other or other objects around the airport (Pringle 2010). Narrowing down the focus on aircraft damage during ground operations, it has been reported that 50% of the major damage was caused by baggage vehicles while 60% of the minor damage was caused by collision of aircraft with ground vehicles (International Air Transport Association, 2005).

The latest composite fuselage aircraft, such as Airbus A350 XWB and Boeing 787, present new challenges regarding certifications, airworthiness, damage tolerance, inspections and maintenance. With these aircraft, special knowledge, experience and training is required. Ground incidents will take place as more of these aircraft are introduced in service. In fact, the first incident of a Boeing 787 has already occurred prior to introducing this aircraft type to the regular commercial service. All Nippon Airways admitted that its first Boeing 787 suffered some slight surface damage to its composite engine inlet cowl after it hit a passenger boarding bridge (Govindasamy, 2011). This highlights the necessity to investigate typical impact scenarios of composite fuselage structures exposed to ground impact in order to improve knowledge on the extent of resulting damage, damage initiation energy threshold, developed damage mechanisms and in-service detectability. One of the particular concerns is that damage generated in composite fuselages can be more difficult to visually detect (when inspecting the outer skin surface) compared to metallic counterparts. Furthermore, if detected, the associated hidden damages may be somewhat different, and potentially more extensive, than that expected in metallic structure. Therefore, for personnel involved in unintentional impacts of composite hulls, it is easier to make an erroneous assumption that no significant damage was generated after what appeared to be a relatively minor incident (e.g. horizontal stabiliser example in Waite, 2006).

1.2 Aim and objectives of the research

The main objectives of the CODAMEIN (Composite Damage Metrics and Inspection) project are:

1. To improve understanding of high energy low velocity blunt impact damage on hybrid composite-metallic aircraft structures
2. To investigate key impact parameters that produce significant impact damage with no or minimal visible damage to the impacted surface.
3. To complement the existing research on high energy low velocity blunt impact
4. To perform a first series of tests to develop recommendations regarding composite-metallic structure damage tolerance and detection.

2 Literature review

2.1 Impact damage of composites

2.1.1 Classification of impact damage by impact velocity

Composite structures are susceptible to impact damage that may not be visible via a surface inspection. The resultant damage and structural response is dependant on the impact velocity and energy. A *low velocity impact* event can be a result of dropped tools or in-service damage with a velocity in the range of 4 - 8 m/s and energy of up to 50 J. It can initiate significant internal damage that is undetectable by visual inspection and is referred to as barely visible impact damage (BVID). While BVID is subjective by nature, it is often defined as damage visible within a range of 1 m, or damage causing a specific permanent indentation. The depth of the residual indentation caused by BVID varies in the literature. For instance, the National Physical Laboratory in the UK defines BVID as damage causing 0.5 mm indentation (Gower, Shaw and Sims 2005), while a depth of 1.27 mm – 2.54 mm (0.05 inch – 0.10 inch) is reported in the NASA publication (McGowan and Ambur 1997). Various aspects of BVID have been studied including publications by Pook, Benak and Gould (1990) who showed that toughened resin composites have a better resistance to BVID; and Kuman and Rai (1993) who studied delamination damage caused by steel and aluminium projectiles. Furthermore, investigations on the influence of impactor shapes indicated the most extensive delamination damage is caused by a blunt hemispherical impactor (Mitrevski, Marshall and Thomson 2006). Several researchers also studied the response of honeycomb sandwich panels subjected to BVID (Tomblin et al. 1999; Meo, Vignjevic and Marengo 2005). According to their work, low velocity impact can produce widespread core damage which can significantly reduce the residual strength.

The above classical assumptions of BVID suggest that the impact energy is relatively low. However, in this research, high energy low velocity blunt impact damage is studied. It is important to highlight that high energy low velocity blunt impact damage is more extensive in scale; however, it may also be barely visible (especially at the impacted external surface of the fuselage). It is a common misunderstanding to always associate BVID with low energy levels and small scale damage. Therefore, in this report, a low energy BVID is referred to as the classical BVID while in other cases it will be referred to as the visible or non-visible high energy low velocity blunt impact damage.

The second category of impact is the *intermediate impact*. It is defined as an impact with a velocity of up to 70 m/s which can be due to runway debris at take-off and landing or caused by a bird strike. A *high velocity impact* is a ballistic impact, thus it is mostly relevant in military applications, while a hyper velocity impact is reserved for impact velocity of 30 - 70 km/s experienced in space applications. Cantwell and Morton (1989) studied the deformation difference for low and high velocity impact. Their work indicated that in the case of low velocity impact, in which the elastic energy absorbing capability is an important factor, the structural geometry determines the impact response. In contrast, under high velocity impact conditions, the projectile generates a localised target response which is insensitive to geometrical parameters.

2.1.2 Classification of impact damage by severity for composite aircraft structures

Since accidental damage of composite structures cannot be completely eliminated, these should be designed to function safely, despite the presence of flaws. Designing for damage tolerance includes selecting damage resistant materials (in particular resin systems), identifying sources and types of damage, knowledge of damage propagation mechanisms and criticality of damage. Damage tolerance of composite aircraft structures depends on design details such as lay-up, frame and stringer pitch, attachment details, crack arrest features, structural redundancy, etc. By understanding damage, being able to predict the evolution of damage in advanced composites and being able to detect critical damage, one can design a structure that can safely withstand given levels of damage that can be detected within regular inspection intervals.

As illustrated in Figure 1, the AMC 20-29 (2010) categorises damage types for composite aircraft structures into five categories as:

Category 1 is allowable damage that may go undetected by scheduled inspections. This includes classical low energy BVID, allowable manufacturing defects or in-service damage that does not cause degradation of the ultimate load carrying capacity over a reliable service life of the aircraft.

Category 2 is defined as a damage that can be reliably detected by scheduled or directed inspections. Typical examples of this category of damage include visible impact damage, deep scratches, detectable delamination or debonding. The resulting residual strength of the composite structure caused by this damage has to be sufficiently above the limit load level for the chosen inspection interval.

Category 3 is damage detectable within a few flight cycles by ramp personnel. Large visual impact damage or damage easily detected by a pre-flight walk-around inspection belongs in this category. The design of the aircraft for Category 3 damage requires features that provide a sufficient damage tolerance capability that retains limit load levels for a short time detection interval.

Category 4 is discrete damage known by the pilot that limits flight manoeuvres. It includes damage due to bird strike, tyre burst or severe in-flight hail.

Category 5 is severe damage of the aircraft caused by ground or flight conditions not covered by design criteria. This may include severe impact of a ground vehicle with an aircraft fuselage, flight overload conditions, in-flight loss of aircraft parts, hard landings or high energy blunt impact. The criticality of this category is highlighted by the fact that in some scenarios there are no clear visual indicators of damage.

Often, impacts, such as ground vehicle impact, can generate Category 2 or 3 damage, which must be managed within the Certification process, e.g. using substantiated scheduled inspections for detection, and immediate repair action when detected. However, such impact may also result in large obvious Category 5 damage, which must be reported, and repaired immediately. Category 5 damage is considered to be outside the immediate aircraft design Certification process, although the need to report such damage is identified as a requirement in documents such as AMC 20-29. Therefore, it becomes necessary to understand the boundaries between Category 2/3 and Category 5, respectively.

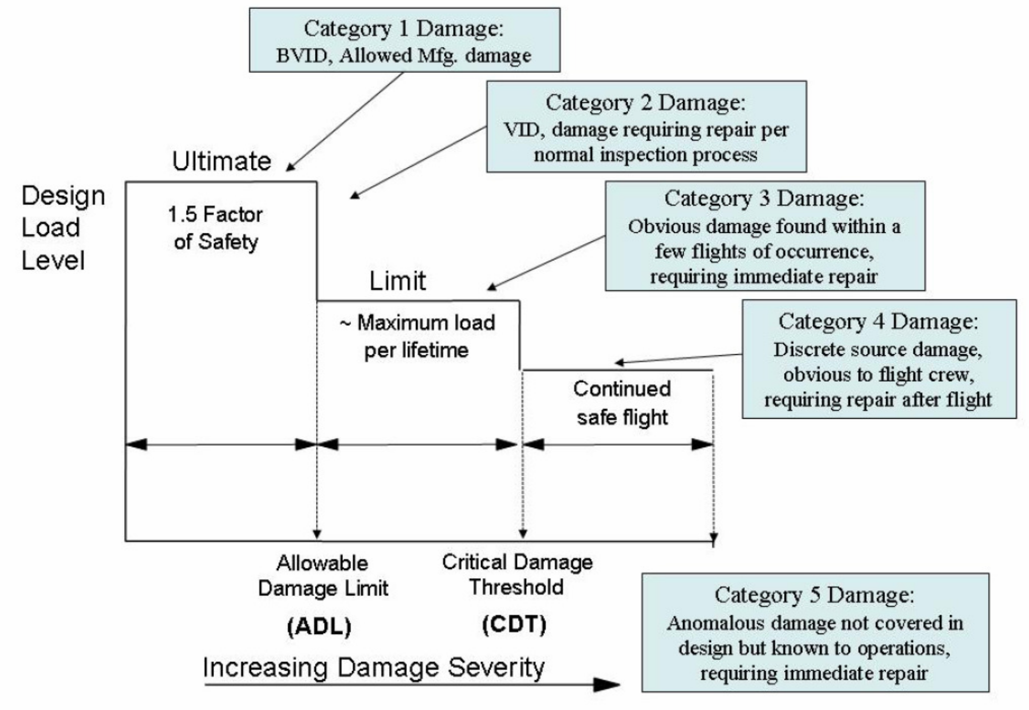

Figure 1. Design load levels vs. damage severity (AMC 20-29 2010)

2.2 *Ground handling operations*

2.2.1 Overview of ground handling operations

Ground handling deals with very complex operations as illustrated in Figure 2. The range of operations and equipment required for a common commercial flight can be summarised as (Ashford, H.P., Stanton, M., Moore, C.A. 2002):

- Ramp services – marshalling, supervision, start-up, aircraft towing
- On ramp aircraft services – ground power supply, maintenance, re-fuelling, wheel check, cleaning, de-icing
- Onboard services – cleaning, catering, in-flight entertainment servicing, modification of seat configuration
- External ramp services and equipment – passenger boarding / passenger steps, catering loaders, cargo loaders, mail and baggage loading

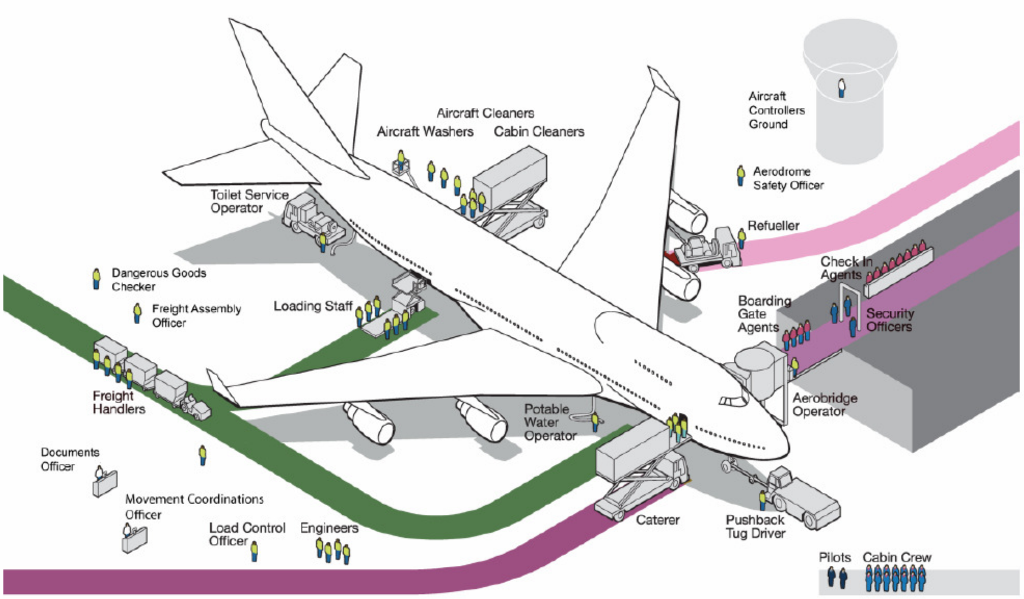

Figure 2. Complexity of ground handling operations (Australian Transport Safety Bureau 2010a)

The nature of complex operations combined with a lack of safety and damage awareness results in a number of incidents during cargo movement while loading the aircraft or docking of mobile stairs around the aircraft doors.

2.2.2 Ground handling incidents review

The most comprehensive review of ground operations incidents was found to be provided by the Australian Transport Safety Bureau (2010a). According to this report, between January 1998 and December 2008 in Australia, there were 398 ground occurrences reported involving large civil aircraft. Out of these, around 70 per cent were related to ground operations and 25 per cent of all incidents reported aircraft damage. A breakdown by location, shown in Figure 3, indicates that 28 per cent of all ground incidents occurred at the gate. This includes high energy low velocity blunt impacts when an aircraft was being prepared for take off or after landing before passenger disembarking or baggage / cargo unloading.

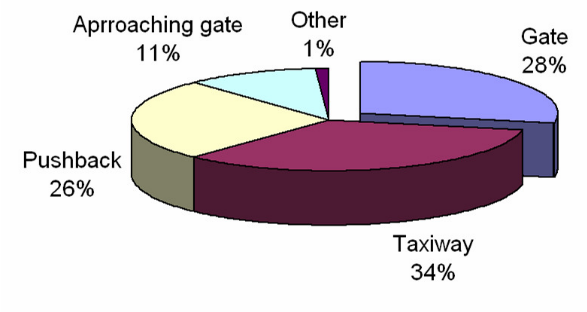

Figure 3. Ground operations incidents by location

While aircraft were parked at the terminal gates, 45 per cent of all incidents resulted in aircraft damage. The most frequently occurring damage was generated by ground vehicles. A summary of the types of vehicles that collided with aircraft at the gates, provided in Table 1, clearly indicates a high frequency of damage caused by cargo loaders and mobile stairs. It was also reported (Australian Transport Safety Bureau 2010a), that about half of these occurrences resulted in a damage of door surrounds while the remaining half resulted in damage of other parts of the aircraft (wing, empennage or engine).

Table 1. Ground vehicle incident summary by vehicle type

Vehicle causing damage	Number	Per cent
Cargo or container loader	8	24.2
Mobile stairs	8	24.2
Catering truck	4	12.1
Aerobridge	3	9.1
Passenger lifter	3	9.1
Belt loader	3	9.1
Tug	2	6.1
Baggage trolley	1	1.3
Fuel truck	1	1.3
Total	**33**	**100.0**

On June 1, 2010, an Airbus A320 (VH-VQL) was impacted by a cargo loader in Sydney, Australia (Australian Transport Safety Bureau 2010b). The 3.5 ton loader unexpectedly accelerated towards the fuselage from a distance of about 2.7 m. A primary impact resulted in a 0.8 mm deep score in the fuselage skin. The force of the impact resulted in a movement of the aircraft tail and a secondary impact between the fuselage and a passenger push-up stairs. The secondary impact resulted in a 0.5 mm dent in the fuselage skin.

Impact damage is commonly repaired by an external patch as shown in Figure 4. Repair patches can be found in the vicinity of the contact areas between a ground vehicle or aerobridge and the fuselage; however, patches were also observed a significant distance away from doors.

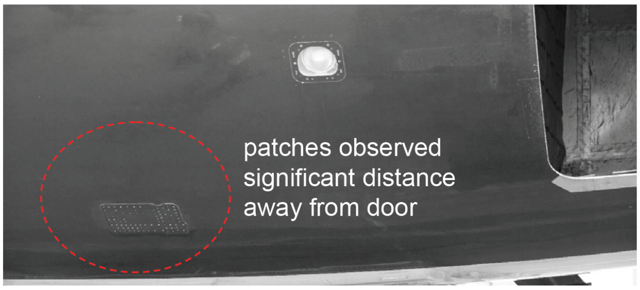

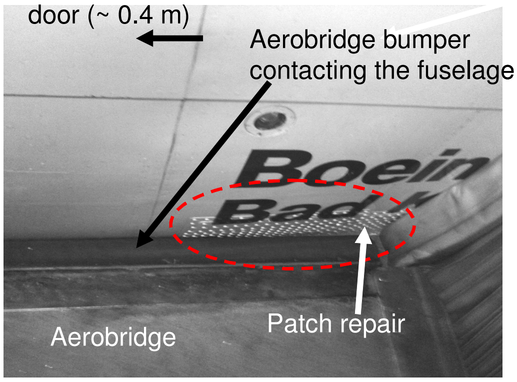

Figure 4. Repair patches around doors

In some cases, especially due to aerodynamic requirements, internal repairs are needed. However, these generally incur a higher maintenance cost. As detailed in this section, door surrounds are damage prone areas due to common impact events during ground operations. Furthermore, door cut-outs are areas of high stress concentration and therefore, these must be reinforced by additional doublers or by the use of high strength materials such as titanium. A review of design features and materials used in CS-25 large aeroplanes is provided in Section 2.3.

2.2.3 Blunt impact energy level survey

Ground handling equipment and vehicles pose risks for impact and damage of aircraft fuselages. Different types of ground vehicles with different roles are found at airports. As detailed in the previous sections, impact damage is often caused by cargo loaders, mobile stair vehicles, belt loaders or aerobridges.

The typical approaching velocity of ground service vehicles was investigated by Kim (2010). The results from a video analysis, shown in Figure 5, assisted in determining the velocity range of a belt loader during normal operation. According to this analysis, a velocity of 1 m/s is common for a vehicle

1 m away from the fuselage. At close vicinity (about 100 mm), the approaching velocity was measured to be approximately 0.5 m/s.

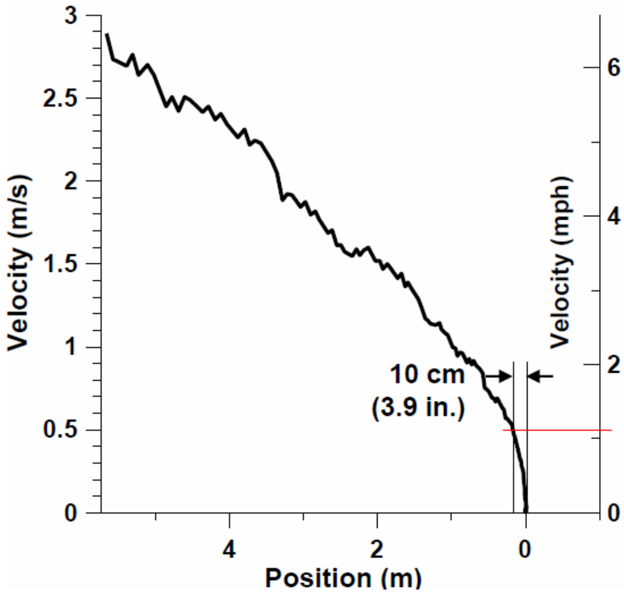

Figure 5. Velocity of a ground vehicle approaching an aircraft

In case of accidental impact, the kinetic energy is directly driven by the mass of the vehicle and its velocity. A review of technical specifications of belt loaders and mobile stair vehicles for narrow and wide body aircraft indicated that depending on size, vehicle type, servicing capacity and engine type, the vehicle mass was in a range of 2500 kg to 5500 kg (TUG Technologies 2011, NMC-Wollard 2011).

Considering data from the 2010 Sydney airport incident (Australian Transport Safety Bureau 2010b) and assuming that the unexpected vehicle acceleration resulted in an impact with the fuselage at 1 m/s, the resulting kinetic energy is:

$$E_k = \frac{1}{2}mv^2 = \frac{1}{2}\times 3500\times 1^2 = 1750J$$

Furthermore, realistic extreme boundaries for the impact energy in ground service vehicle incidents can be given by considering an incident of a 2000 kg vehicle at 0.3 m/s (lower limit) and impact of a 5000 kg vehicle at 1.2 m/s (upper limit). These assumptions give a blunt impact energy level range between 90 J and 3600 J.

Alternative guidelines can be obtained from the results of Kim et al. (2010). In this work, a composite stringer-reinforced panel was quasi-statically tested using an OEM rubber bumper. Test result observations reported large deformations in the panel, delamination between the skin and the stringers, shear tie fracture and continuous cracking. However, no permanent deformation or externally visible damage was found. From the load-displacement curve, it was estimated that about 700 J of energy was needed to generate such a damage of the panel. In the subsequent test program (Kim 2011) that incorporated larger three-frame composite panels, approximately 955 J and 2500 J for the first and second loading, respectively, was required to generate wide spread internal damage without any obvious external permanent deformation.

In conclusion, based on the available incident data and test results, an expected blunt impact energy level to generate characteristic failure modes found in ground service vehicle incidents was estimated to be about 1000 J – 3000 J. There are several key parameters that affect the type and size of internal and external damage such as panel configuration, impactor type and boundary conditions.

2.3 Design and materials of CS-25 aircraft fuselages

In order to establish a credible design of the test panel, an extensive review of the design and materials in CS-25 aircraft fuselages was conducted. The review focuses on the geometry and sizing of frames, stringers, overall fuselage size and design features found around door surrounds.

According to Niu (1999), the average frame pitch for civil aircraft ranges from 457 mm (18 in) to 558 mm (22 in). Examples given in Roskam (2002) show that most civil transport aircraft have a frame pitch of around 508 mm (20 in). Some reports suggest that the current state-of-the-art aircraft have an extended frame pitch. Norris and Wagner (2005) report that the A380 fuselage frame pitch was extended to 635 mm (25 in) from the standard Airbus frame spacing of 533.4 mm (21 in).

2.3.1 Airbus

Airbus A320 family

The Airbus A320 family is a family of short-to-medium range, narrow-body, commercial airliners which includes the A318, A319, A320 and A321. The fuselage diameter for all versions of this family is 3.96 m (Airbus-A320-Familie 2011). The differences in fuselage configuration for the A319 to A321 are summarised in Table 2 (Gerzanics 2003). According to this, it is estimated that the frame pitch of the A320 family is 533.4 mm (21 in).

Table 2. Size of the A320 family aircraft

Aircraft type	A319-100	A320-100	A321-100
Fuselage length [m]	33.84	37.57	44.51
Difference to A320 [m]	-3.73		+6.94
Difference to A320 [number of frames]	-7		+13

The A320 family aircraft have Z-profile stringers that are riveted to chemically milled skin panels (Warwick 1986). Airbus estimated that it saved 800 kg by using composite materials. The sections made of composites, shaded in Figure 6, include primary structures - fin, vertical tail plane and movable trailing edge devices. In these structures aramid fibre, glass fibre and carbon fibre reinforced plastics (CFRP) are used. The A320 is the first subsonic aircraft to incorporate composite primary structures (Airbus A320 single-aisle medium-range airliner 2011).

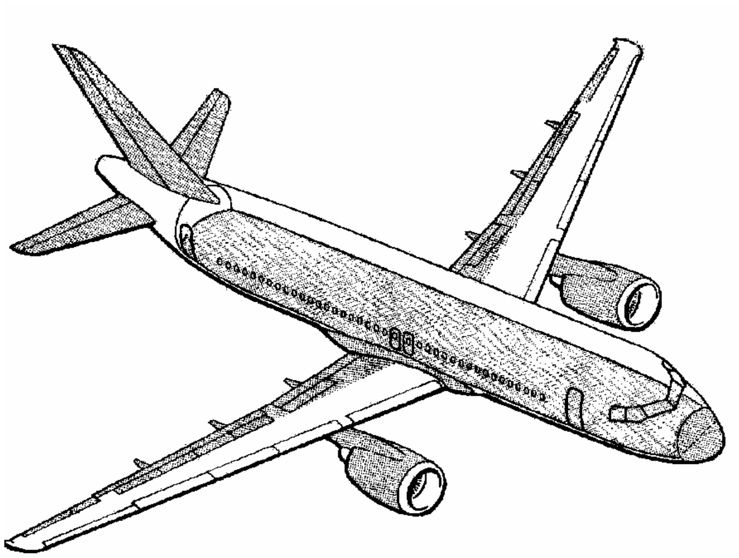

Figure 6. Composite materials in the A320 (Warwick, 1986)

Figure 7. An A320 fuselage shell (taken from www.premium-aerotec.com)

Airbus A330 / A340 family

Only limited information has been found in the public domain on the fuselage design of the A330 / A340 family. The fundamental design and diameter was taken from previous A300 / A310 aircraft types. The fuselage has a diameter of 5.64 m and is made from aluminium alloys (Airbus A330 2011). The frame pitch in this family is 533.4 mm (21 in) (Kingsley-Jones 2003). The aft fuselage around the main passenger door on the Airbus A340 is shown in Figure 8. The figure shows typical stringer – frame junctions and riveted skin panels. Additionally, the increased skin thickness around the door surrounds is visible.

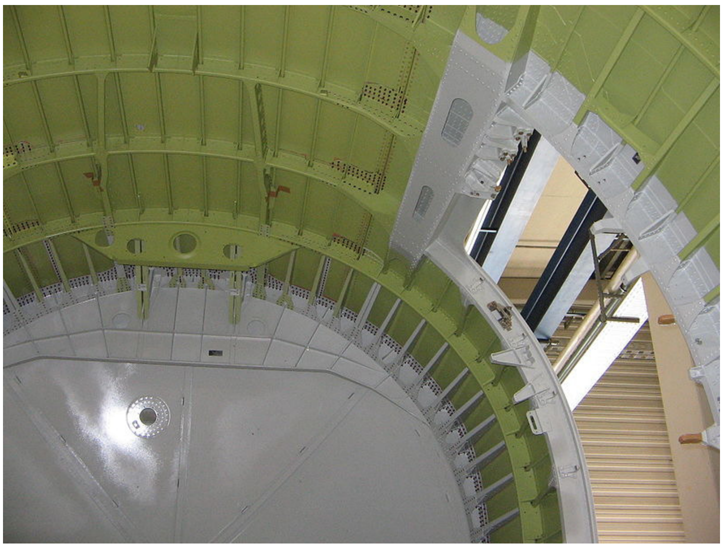

Figure 8. Fuselage of the A340 (taken from http://de.wikipedia.org)

Airbus A350 / Airbus A350 XWB

The Airbus A350 XWB is a wide-body aircraft with a maximum outside fuselage diameter of 5.97 m (Airbus A350 2011). It has gone through several major design revisions. The initial design of the A350 XWB featured metallic frames as illustrated in Figure 9. The presentation by John Leahy (chief commercial officer) (Leahy 2006) indicated that the frames, ribs, floor beams and gear bays are made of aluminium or aluminium-lithium alloys which accounted for 20% of the total weight of the aircraft.

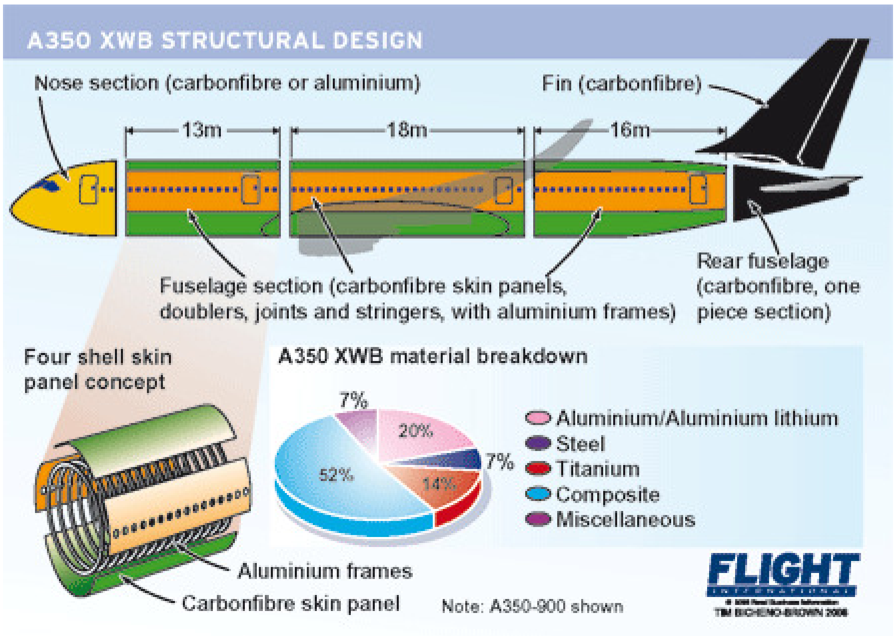

Figure 9. Initial design of Airbus A350 XWB (taken from www.aviationnews.eu)

Following criticism from public and from aircraft operators, Airbus switched to a composite frame design (Hamilton 2007). Other reports from 2007 also suggested a key change from metallic to carbon fibre fuselage frames, although the fuselage crossbeams remained metallic (Kingsley-Jones 2007). An illustration of the A350 XWB design revision is shown in Figure 10.

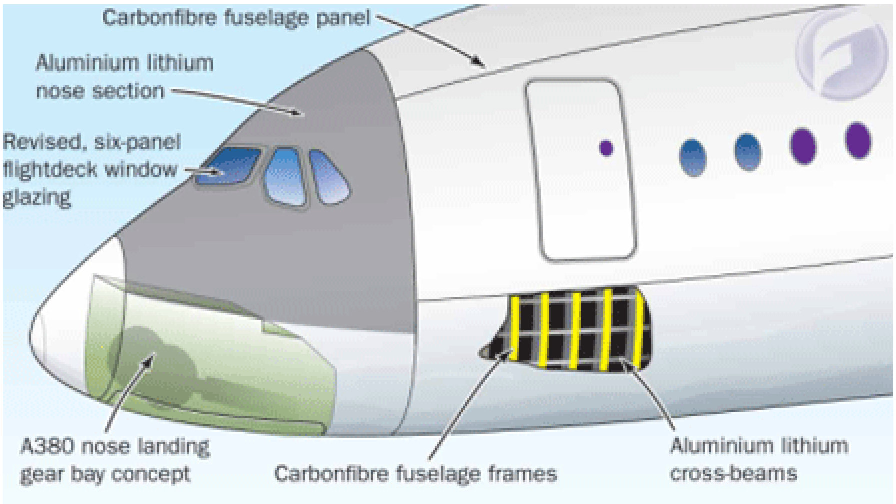

Figure 10. The A350 XWB design revision (taken from www.flightglobal.com*)*

Subsequently, Airbus also reversed an earlier decision to use metal stringers in favour of bonding CFRP stringers to the skin panels (Airbus A350 XWB update 2010). This reduced the number of fabricated parts and fasteners. Airbus has opted to clothe a pre-fabricated fuselage skeleton with large carbon fibre composite panels. Stringers and most frames are made from CFRP, although certain frames in high load areas are made from titanium so that the crashworthiness criteria can be met. An illustration of the latest A350 fuselage design is shown in Figure 11.

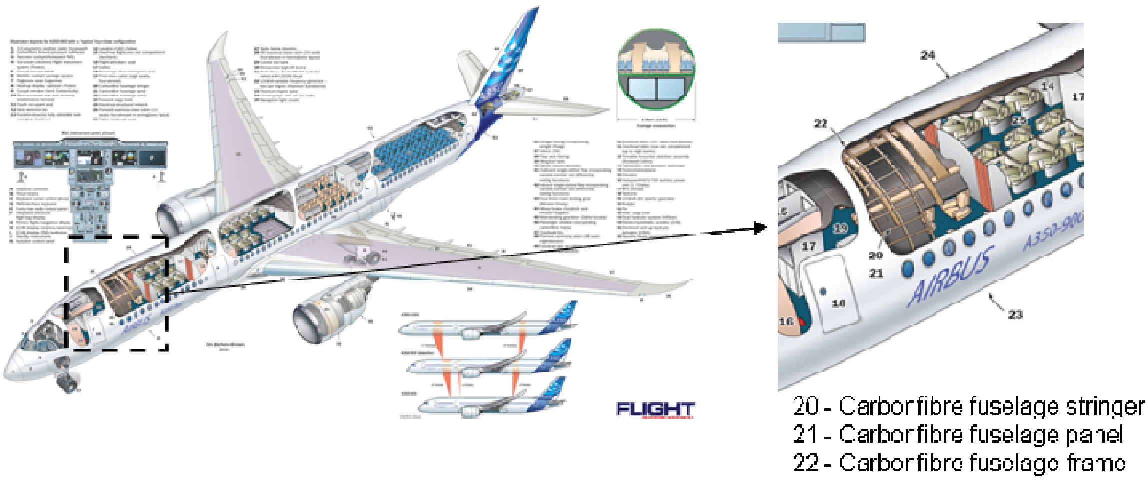

Figure 11. Airbus A350 XWB (taken from www.aviationexplorer.com)

According to the Airbus A350 XWB update (2010), titanium accounts for 14% of the weight of the aircraft. It is used for highly loaded frames, door surrounds, landing gear, engine pylons and in sections that require reinforcement to withstand high-velocity bird strike impacts. Door frames are manufactured by Premium AEROTECH GmbH who provides further reference on the use of titanium in passenger and cargo door surrounds as shown in Figure 12 (Airbus A350 XWB – work packages Premium AEROTEC 2011). Information on the use of titanium and composite materials in the A350 XWB design is additionally available from the Airbus website (2011). This reveals that the A350 XWB fuselage panels, frames, stringers, window frames, clips, and doors are made from CFRP, with a hybrid door frame structure consisting CFRP and titanium.

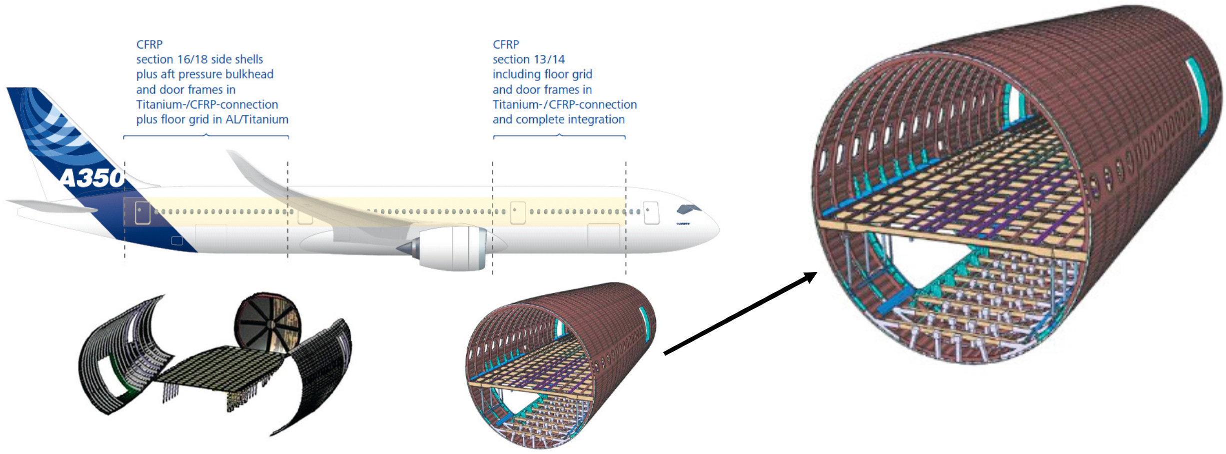

Figure 12. The use of titanium in the Airbus A350 XWB (taken from www.premium-aerotec.com)

The A350 fuselage is manufactured using a multi-panel construction method comprising of fuselage sections built from four composite panels: two long side panels joined by much shorter upper and lower panels. Depending on the location in the aircraft fuselage, the stringers are either Omega- or T-shaped and are straight or curved (Composites World 2010). Instead of being moulded as part of each panel, omega-profile carbon fibre stringers are manufactured separately and bonded to the skin panels (Burchell 2009). Omega-shape stringers for the A350 XWB are produced by Alliant Techsystems and CNIM Group. Examples of these stringers, shown in Figure 13, show extended flange width areas that provide a flush surface for the attachment of composite clips.

Figure 13. Omega-profile stringers of the Airbus A350 XWB (taken from www.cnim.com)

The fuselage frames and skin panels are not bonded together. These joins are made with a mix of thermoplastic clips and special fasteners. Based on the difference in fuselage length and number of frames between the -900 and the -1000 versions, which is 7 meters and an additional 11 frames, the frame pitch is estimated to be 635 mm (Aviation explorer website 2011). Weight is also saved in the window frames, which, in metal, normally have a T-section profile. Carbon fibre construction allows this to be pared to a lighter L-profile while retaining the same strength (Burchell 2009).

Airbus A380

The A380's fuselage has an elliptical cross section which is 7.14 m wide and 8.41 m high (Airbus A380 2011). While most of the fuselage is made of aluminium, composite materials comprise more than 20% of the A380's airframe (Roberts 2007). As presented in Figure 14, carbon-fibre reinforced plastics, glass-fibre reinforced plastics and quartz-fibre reinforced plastics are used in wing trailing edge devices, fuselage sections (such as the undercarriage and the rear end of the fuselage) and empennage (Norris 2005).

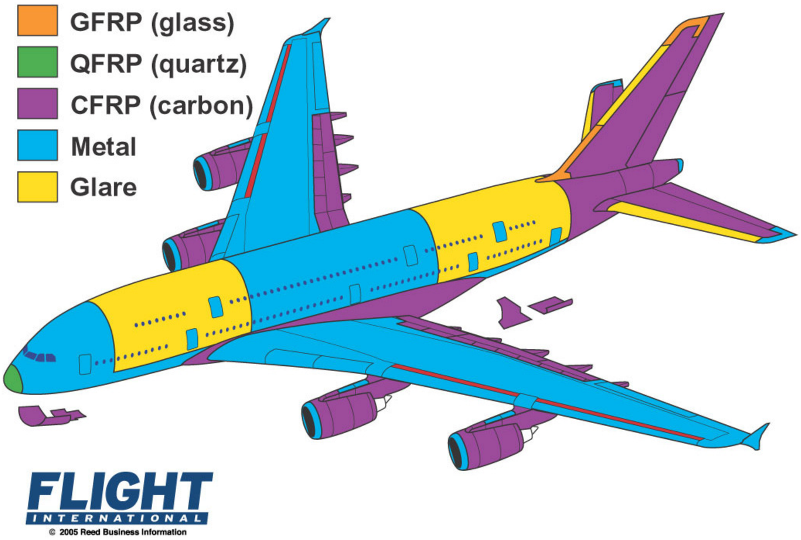

Figure 14. Materials used in the Airbus A380 aircraft (Norris 2005)

Glare material is made up of alternating layers of aluminium sheets and glass fibre reinforced film, and, in current applications, ranges in thickness from the 0.25mm-thick Glare 2A used for buttstraps, to the 0.375mm thick Glare 4A/B used for skin panels. Aluminium-copper (Al-Cu) 2024 and 2524 alloys are used for the skin of the cockpit and adjacent Section 12 as well as the extremely large centre Section 15. The lower skin panels of Section 13 (forward fuselage) and Section 18 along the belly are made up of aluminium 6013. Door cut-outs are strengthened with local doublers made from titanium and aluminium alloys (Norris 2005).

Not including Glare, composites make up 22% of the A380 by weight. Aluminium comprises of 61%, Glare 3% and titanium and steel 10%, with miscellaneous materials making up the balance (Building to fly 2003). Glare is used for the upper fuselage shells, crown and side panels, and is being studied for possible use in later models on the empennage leading edge because of its good bird strike capability. Advanced aluminium alloys are used for the centre upper fuselage section, where their fatigue resistance and damage tolerance make them suitable for increased residual strength and preventing crack growth (Building to fly 2003). The 7040-T7451 plate alloy was selected for several fuselage applications, such as integrally machined main frames, cockpit window frames, beams, and fittings. Alloy 2024-T432 extruded profiles were chosen for many fuselage frames due to their weight and material usage efficiencies (Key to Metals website 2011).

Extruded frames are installed in the lateral panels between both decks and the whole upper shell. Machined frames are positioned in highly loaded areas such as the complex centre fuselage lower shells, the wing root area, door cut-out surrounds and the nose section. The A380's frame pitch is 635 mm (25 in) (Norris and Wagner 2005).

2.3.2 Boeing

Boeing 737

Nine series of the Boeing 737 were produced, designated from 737-100 to 737-900. The fuselage length ranges from 27.66 m (737-100) to 40.68 m (B737-900) while in all series the width is constant and measures 3.76 m (The Boeing 737 technical site 2010).

A typical material used in the construction of the Boeing 737 fuselage is Aluminium 2024-T3, which possesses superior fatigue characteristics and is used for the skin panels. According to published data, the fuselage skin thickness of a pressurised, narrow-body aircraft such as the Boeing 737 is in the order of 1 mm – 1.6 mm (0.040 in – 0.0625 in) (Lindeman 2006, ARFF website 2006). The thickness of the skin in the fuselage is usually smaller than that used in the wing. The metallic skin panels are fastened to the stringers and the frames.

Aluminium 7075-T6, a high strength alloy, is used for all other structural members, including frames, under-floor beams and stringers (ARFF website 2006). As presented in Figure 15, the aircraft is made up of interlocking semi-circular metallic pieces called *chords*. Once they are put together they form the frame. The frame pitch is approximately 508 mm (20 in) and the stringer pitch ranges between 152 mm (6 in) and 178 mm (7 in). A standard Boeing 737 stringer attachment drawing, shown in Figure 16, indicates that the fuselage design consists of omega-profile stringers while the frames have a Z-profile (Jormac Aerospace, 2011).

Exit doorways and cargo hatches are potential weak points in this fuselage. In order to strengthen these sections, huge re-enforcing sheets, called *bear straps*, are assembled around the door surrounds. There are eight bear straps in the 737 which are bonded to the skin.

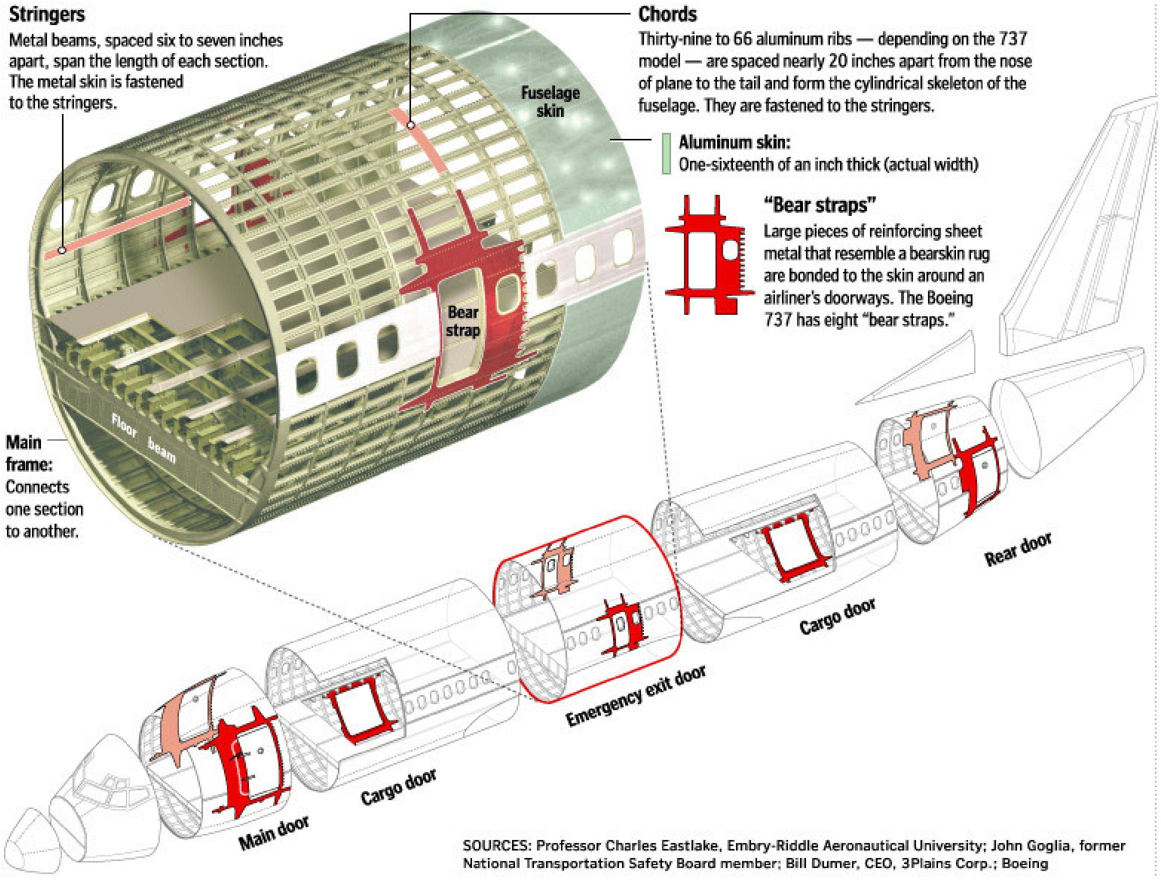

Figure 15. Boeing 737 fuselage construction (Lindeman 2006)

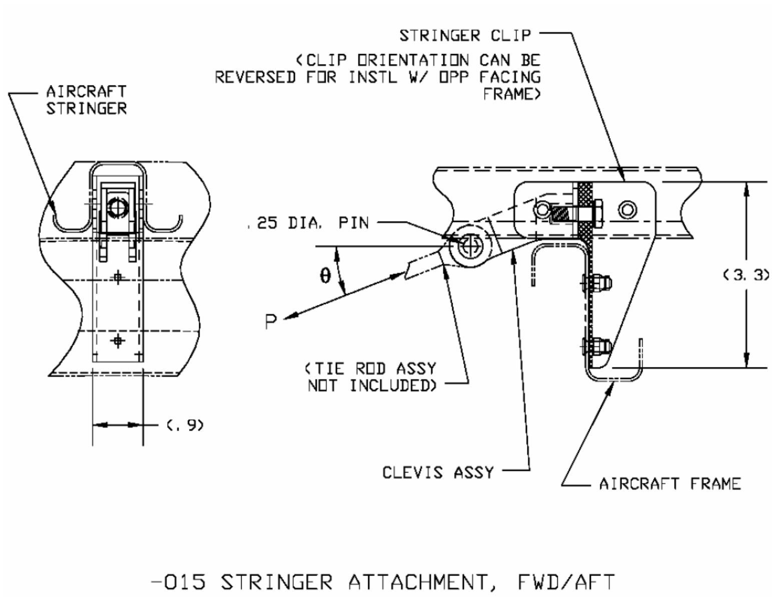

Figure 16. Standard Boeing 737 stringer attachment (Jormac Aerospace 2011)

Boeing 747

The fuselage of this aircraft type is of approximately circular section over most of its length, with the forward fuselage having a nominal diameter of 6.4 m (21 feet) where the cross-section is constant. The fuselage is of conventional skin, stringer and frame construction, riveted throughout, generally using countersunk flush riveting for the skin panels. The fuselage of the 747 is completely metallic (Boeing 747 2011, Charles 1990). The skin panels are approximately 1.8 mm - 2.2 mm thick. These are joined using vertical butt joints and horizontal lap joints. The horizontal lap joints used three rows of rivets together with a cold bonded adhesive.

According to Calawa et al. (1994), the stringers found on the 747 are roughly 76.2 mm (3 in) wide, 38.1 mm (1.5 in) high and have an approximately 25.4 mm (1 in) inner dimension of the hat. The four main types of stringers, shown in Figure 17, are straight, contoured, joggled and offset. They are made of 7075 aluminium alloy and have a thickness from 1.27 mm to 3.175 mm (0.050 in to 0.125 in).

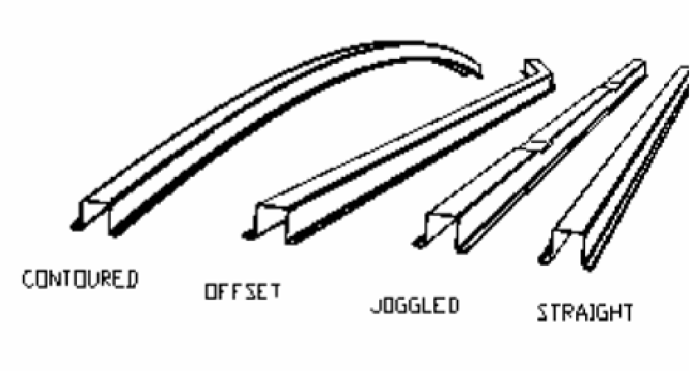

Figure 17. Stringer types on the Boeing 747 aircraft

Further references shown in Figure 18 - Figure 20 additionally depict design features of the 747 including stringers with omega- or Z-cross sections and C- or Z-profile frames (Cutler 2005). Based on the illustration shown in Figure 19, the height of the C-profile frames is 150 mm. The fuselage frames are spaced at 508 mm (20 in) intervals (Luchtzak website 2006) and the stringer pitch ranges from 203 mm to 254 mm (8 in to 10 in) (Seo 1984). According to Harrison (1968), the 747-100 has the normal frames made from light weight aluminium alloy while the door frame doublers are made from titanium.

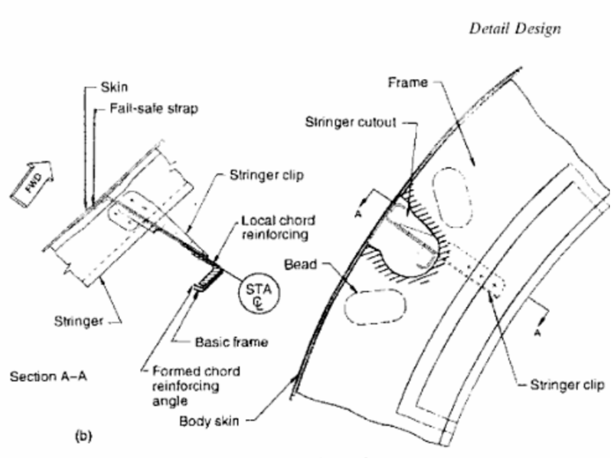

Figure 18. Fuselage sections of the Boeing 747 aircraft (www.answers.com/topic/fuselage, Cutler 2005)

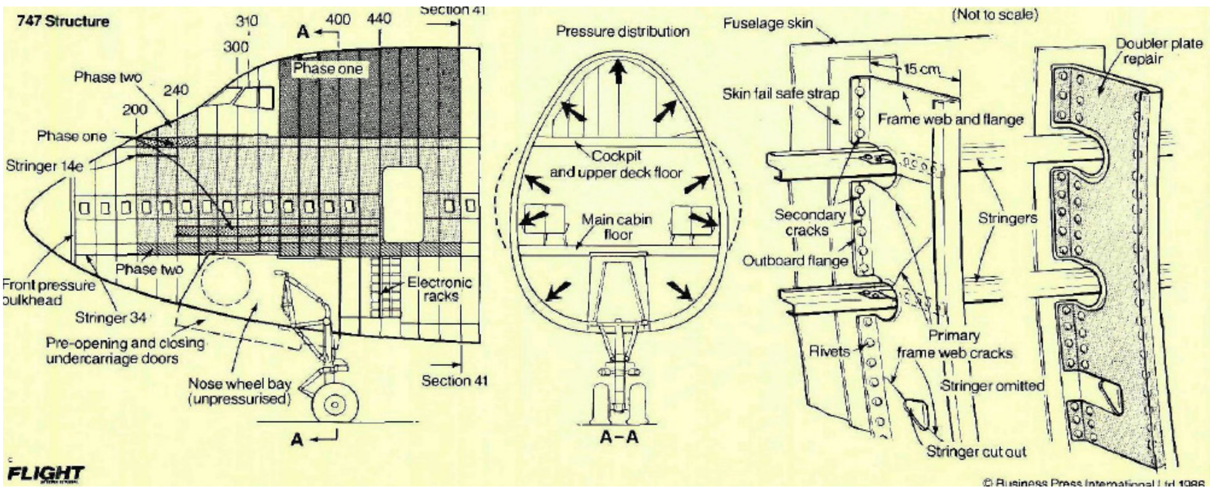

Figure 19. Fuselage design of the Boeing 747 (from Flight International, 1 March 1968)

Figure 20. Boeing 747 fuselage (taken from www.answers.com/topic/fuselage)

Boeing 777

The Boeing 777, which had its maiden flight in 1994, is a long range, wide-body airplane with a fuselage barrel diameter of 6.20 m. The airplane has the identical fuselage dimensions for its -200, -300 series and the freighter version 777F (Boeing 777 2011).

From a structural-weight standpoint, the 777 is primarily an aluminium airplane. Seventy percent of the overall structure is made of aluminium, including the wing box and the fuselage. The use of aluminium alloys and other materials is illustrated in Figure 21. Despite the predominance of aluminium, the 777 does contain significantly more composite materials by weight than earlier Boeing aircraft. Nine percent of the 777's structural weight is made of advanced composite materials, primarily in secondary structures such as flaps, rudders, engine nacelles and landing gear doors.

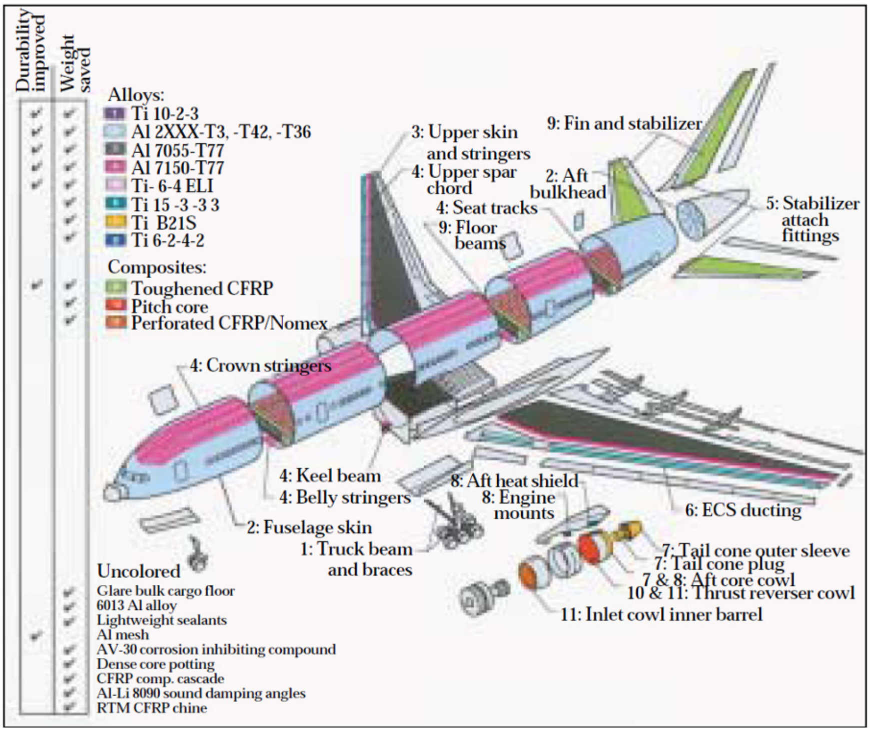

Figure 21. Breakdown of materials on the 777 (Smith 2003)

The 777 has tougher, stronger, and more corrosion-resistant fuselage stringers which are made of higher-strength aluminium 7150. The skin durability was also improved due to the properties of the new material used in the 777, aluminium 2524. Titanium alloys are used extensively in interface areas. In addition, titanium replaced many steel components in the landing gear and engine strut area in an effort to reduce weight and improve corrosion resistance (Smith 2003).

The fuselage construction of the 777 is shown in Figure 22. According to Birtles (1998), Boeing selected a Z-profile stringer design to avoid corrosion from trapped moisture. Based on a visual observation from Figure 22, an average stringer pitch is believed to be approximately 230 mm.

The 777 represented a breakthrough in material applications for large commercial aircraft which created a greater opportunity for innovation for the subsequent aircraft developed by Boeing, the 787.

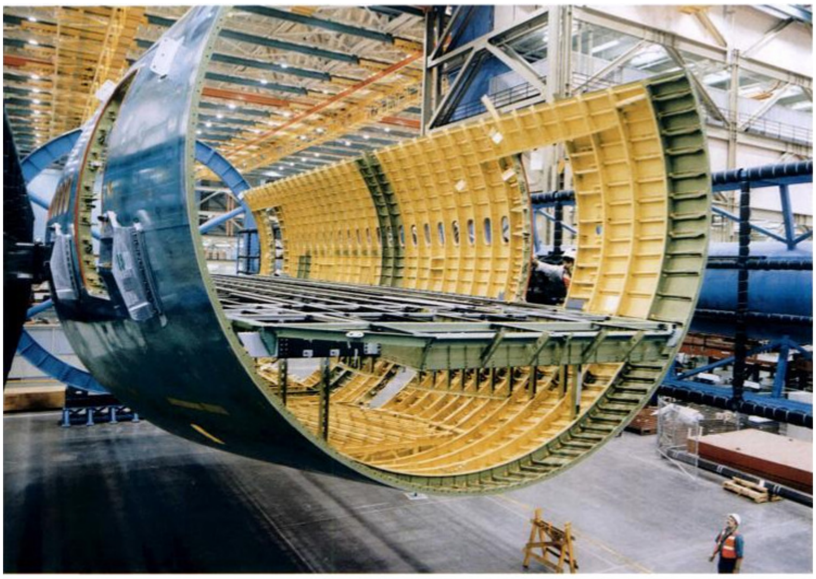

Figure 22. Fuselage construction of the 777 (Birtles 1998)

Boeing 787

The Boeing 787 is made from a total composite content of 50% by weight, including the integration of an all-composite fuselage, wings and tail. Remaining materials are 20% aluminium, 15% titanium, 10% steel and 5% other materials (Boeing 787 Dreamliner 2011). Figure 23 shows a composite fuselage section of the 787 with co-cured stringers that have an omega profile. According to Ostrower (2009), each 787 barrel section contains 80 stringers that run the length of the fuselage. Assuming a regular distribution along the barrel which has a diameter of 5.77 m (Wide-body aircraft 2011), the stringer pitch can be calculated to be approximately 227 mm.

Figure 23. Composite fuselage section of the Boeing 787 (Boeing 787 Dreamliner 2011)

Similar to the A350 XWB, the 787 fuselage has titanium door-frames for cargo and passenger doors (RTT News 2009) which are shown in Figure 24. The average frame pitch is reported to be approximately 610 mm (24 in) (Airliners website 2008).

Figure 24. Titanium components for the Boeing 787door frames (B787 door frames 2011)

2.3.3 Additional general summary of CS-25 fuselage designs

Based on further discussions with the aircraft manufacturers and University of California San Diego (UCSD), the following general summary can be provided:

Materials

By weight, about 50% of the latest airplanes, such as Airbus A350 XWB and Boeing 787, are made of CFRP (skin, stringers, and frames). These have titanium door frames.

The CS-25 category airplanes made by Airbus and Boeing until mid-to-late 1990s primarily consist of metallic (mostly aluminium) frames, stringers and skin.

Geometry

Frame cross sections have generally Z- or C-profiles with a height of 85 - 100 mm, thickness 2 – 3 mm, flange width of approximately 25 mm.

Z-profile stringers: height of about 30 mm, thickness of 2 mm and flange width of approximately 15 mm.

Omega-profile stringers: height in a range of 25 - 35 mm, thickness of 1.5 - 2.0 mm, head width of 25 mm and total foot width between 100 mm - 130 mm.

Depending on location, the skin thickness was reported to vary from 1.0 to 2.6 mm.

Frame pitch

Main fuselage pitch ranges between 457.2 mm – 533.4 mm (18 - 21 in), latest aircraft have an extended frame pitch of 610 mm – 635 mm (24 - 25 in).

Stringer pitch:

150 mm - 250 mm

3 Methodology

3.1 Panel design

The literature review and input from the UCSD were key inputs to establish a credible baseline design for the hybrid test panel. Although the UCSD research project focuses on monolithic composite panels, in this project a hybrid design concept was selected. This increased the level of agreement with the design features of modern CS-25 fuselage designs at the passenger and cargo door surrounds.

An isometric view of the panel is shown in Figure 25. The four-bay test panel has overall dimensions of approximately 1930 mm by 1830 mm (refer to Appendix A). It consists of four composite stringers that are co-cured to the skin panel. Skin, shear ties (clips) and stringers are made from aerospace grade carbon fibre reinforced unidirectional tape (X840 Z60 12k) and plain weave fabric (X840 Z60 PW) prepreg, procured from Cytec Industries Inc. Stacking sequences of all composite parts are summarised in

Table 3.

The omega-profile stringers were designed to have a height of 38.1 mm (1.5 in.), a nominal thickness of approximately 2.2 mm, a head width of 25.4 mm and a total foot width of about 178 mm. In order to retain commonality with the panels tested by UCSD, the stringer pitch was selected as 304.8 mm (12 in.).

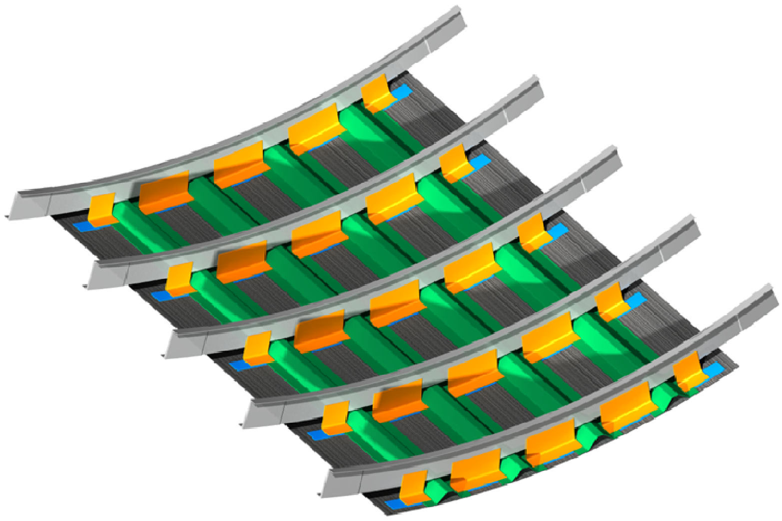

Figure 25. 3D model of the CODAMEIN fuselage panel

Table 3. Stacking sequence of composite parts

Skin				Shear Tie			
Ply	**Material**	**Nominal ply thickness [mm]**	**Ply orientation**	**Ply**	**Material**	**Nominal ply thickness [mm]**	**Ply orientation**
1	Fabric	0.25	0/90	1	Fabric	0.25	+-45
2	UD	0.15	0	2	Fabric	0.25	0/90
3	UD	0.15	45	3	Fabric	0.25	+-45
4	UD	0.15	90	4	Fabric	0.25	0/90
5	UD	0.15	-45	5	Fabric	0.25	+-45
6	UD	0.15	0	6	Fabric	0.25	0/90
7	UD	0.15	45	7	Fabric	0.25	0/90
8	UD	0.15	90	8	Fabric	0.25	+-45
9	UD	0.15	-45	9	Fabric	0.25	0/90
10	UD	0.15	-45	10	Fabric	0.25	+-45
11	UD	0.15	90	11	Fabric	0.25	0/90
12	UD	0.15	45	12	Fabric	0.25	+-45
13	UD	0.15	0				
14	UD	0.15	-45				
15	UD	0.15	90				
16	UD	0.15	45				
17	UD	0.15	0				
18	Fabric	0.25	0/90				
Stringer				**Shim**			
Ply	**Material**	**Nominal ply thickness [mm]**	**Ply orientation**	**Ply**	**Material**	**Nominal ply thickness [mm]**	**Ply orientation**
1	Fabric	0.25	0/90	1	Fabric	0.25	0/90
2	UD	0.15	0	2	UD	0.15	0
3	UD	0.15	45	3	UD	0.15	45
4	UD	0.15	-45	4	UD	0.15	-45
5	UD	0.15	90	5	UD	0.15	90
6	UD	0.15	45	6	UD	0.15	45
7	UD	0.15	-45	7	UD	0.15	-45
8	UD	0.15	0	8	UD	0.15	0
9	UD	0.15	0	9	UD	0.15	0
10	UD	0.15	-45	10	UD	0.15	-45
11	UD	0.15	45	11	UD	0.15	45
12	UD	0.15	90	12	UD	0.15	90
13	UD	0.15	-45	13	UD	0.15	-45
14	UD	0.15	45	14	UD	0.15	45
15	UD	0.15	0	15	UD	0.15	0
16	Fabric	0.25	0/90	16	Fabric	0.25	0/90

Five metallic frames are mechanically fastened to the skin via 25 composite shear ties. The frames are machined from Aluminium Al 7075-T6 which is identical to the material used in the Boeing 737 fuselage frames and stringers (ARFF website 2006). The frame cross section was designed with a Z-profile with a height of 108 mm, a thickness of 2.54 mm and a flange width of 25.4 mm. The frames are uniformly spaced by 457.2 mm (18 inches).

A comparison of reviewed CS-25 fuselage designs with the final design of the test panel is provided in Table 4. The main deviation between the panel and reviewed data appears to be the stringer pitch. However, the selected spacing was commented to be in a reasonable range during discussions between the UCSD and aircraft manufacturers. Therefore, the panel design selected for this project represented the best compromise in terms of realistic representation of a typical CS-25 fuselage construction combined with the existing research of UCSD.

Table 4. Size of the A320 family aircraft

Aircraft type	Fuselage diameter [m]	Skin material	Frame material	Frame profile	Frame pitch [mm]	Stringer material	Stringer profile	Stringer pitch [mm]	Additional remarks
A320	3.96	Aluminium	Aluminium	*N/A*	533	Aluminium	Z	*N/A*	Highly loaded parts of the fuselage are made from titanium or steel
A330/A340	5.64	Aluminium	Aluminium	*N/A*	533	Aluminium	*N/A*	*N/A*	
A350	5.97	Composite	Composite	T, L *(Window)*	635	Composite	T, Omega	*N/A*	Frames in highly loaded areas are made from titanium
A380	Width 7.15 Height 8.40	Aluminium, Glare	Aluminium	*N/A*	635	*N/A*	*N/A*	*N/A*	Door cut-outs reinforced with doublers made from titanium and aluminium alloys
B737	3.76	Aluminium	Aluminium	Z	508	Aluminium	Omega	152 - 178	
B747	6.40	Aluminium	Aluminium	Z, C	508	Aluminium	Omega, Z	203 - 254	Door frames are made from titanium
B777	6.20	Aluminium	Aluminium	*N/A*	508	Aluminium	Z	230 *(estimated)*	Titanium is used in the interface areas
B787	5.77	Composite	Composite	*N/A*	610	Composite	Omega	227 *(estimated)*	Door frames are made from titanium
CODAMEIN Panel	5.59	Composite	Aluminium	Z	457	Composite	Omega	305	

3.2 Manufacturing

The test panel was manufactured following manufacturing procedures from the existing research project of UCSD. Ply patterns were developed using FiberSim software and all plies for the skin, stringers, shims, and shear ties were cut using a commercial cutter.

Firstly, the skin plies were laid onto the curved tool. The stringer moulds were accurately positioned on the skin plies. In order to avoid the onset of delamination growth at the radii of the stringer-to-skin interface (often referred as a noodle region), a folded continuous tape strip was placed against the silicone stringer mould to create a smooth radius transition, as presented in Figure 26.

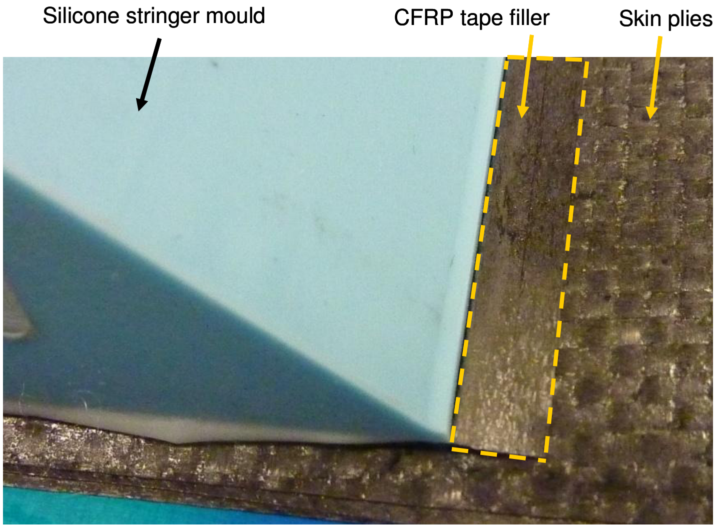

Figure 26. Stringer-to-skin interface detail

Subsequently, the stringer and shim plies were laid up and the panel was cured in an autoclave following the material supplier's recommended curing cycle. A second curing was used to manufacture the shear ties laid up on an L-shaped tool. The curved skin panel with co-cured stringers was then trimmed followed by drilling of the fastener holes using specially developed drill jigs. The shear ties were then fastened to the skin using Hi-Lok fasteners. Lastly, the CNC-manufactured aluminium frames were bolted on. The final panel is shown in Figure 27.

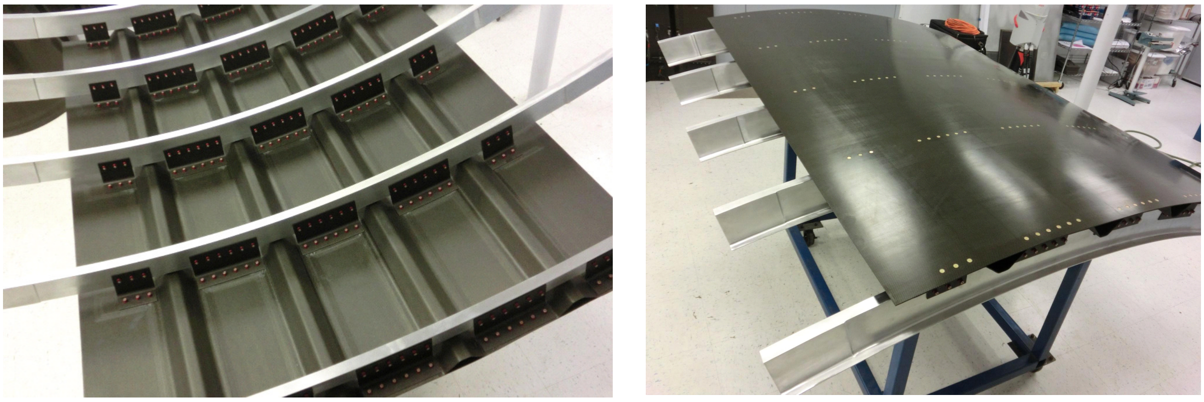

Figure 27. CODAMEIN test panel

A dimensional inspection was conducted using a laser tracker as shown in Figure 28. The quality control procedure highlighted several minor non-conformances with the supplied engineering drawings. It was found that in the assembly stage, due to the panel's flexibility, the radius decreased while stringer moulds slightly shifted during curing. Discrepancies with the engineering drawings were assessed and found not have a minimum influence on the expected test results (e.g. global deformation of the test panel, initiation and growth of damage).

Figure 28. Dimensional inspection of the panel using a laser tracker

3.3 Test methods review and selection

Test methods considered in this study and their advantages and disadvantages to replicate typical conditions during a high energy blunt impact of a ground service vehicle are summarised in the following sections.

3.3.1 Dynamic Impact Test System (DITS)

DITS is a system that is able to throw objects at a controlled speed and direction, which makes it possible to perform several tests with the same impact conditions. By using this system, repeatability is guaranteed.

General characteristics and boundary conditions:

- Impact velocities from 2 m/s to 15 m/s.
- Impactor masses from 2.5 kg to 60 kg.
- LINAC (LINear ACcelerator) available to accurately produce varying impact energies.

- Movable test frame with 3 axis linear and angular motions.
- Fast test set-up using computer controlled positioning and laser assisted targeting.
- Easily adaptable to new impactors.

Advantages:

- Wide range of possibilities to adapt impactors according to the CODAMEIN project requirements.
- Simplicity to modify the velocity or the angle of the impact.

Disadvantages:

The main weakness of this methodology is its realism. The aim of the project was to represent the impact of a ground service vehicle (high mass object) against a composite fuselage, which usually takes place at low speed. With the DITS it could probably be possible to represent an impact with the same (or similar) energy, by increasing the speed, given that the mass of the impactor is lower than the mass of the ground service vehicle.

3.3.2 Crash test laboratory

The crash laboratory facilities available for this project were designed to perform crash impact tests of vehicles in order to comply with worldwide regulations and assessment programs. The laboratory includes a numerically controlled towing system which pulls the vehicles against the impact block according to the specified conditions. This system is able to pull not only vehicles but also sled-like structures. To perform the tests according to the objectives of the CODAMEIN project, it could be possible to attach the panel on the impact block and conduct a test using a bumper-shaped impactor. The impactor could be fixed onto a crash test vehicle with a defined mass which is pulled using the towing system.

Advantages:

- Increased level of realism to represent low velocity / high energy impact conditions (up to 110 km/h and 3500 kg vehicle).
- Flexibility of the facility to change impact angles, velocities, masses, etc.

Disadvantages:

- Cost
- Accuracy of the impact velocity at low speed

3.3.3 Displacement-controlled test

Displacement controlled tests were conducted in the existing research of UCSD. This test method allows performing of a number of load cycles representing different impact energies (controlled by a specified displacement). Energy levels introduced in the test can correspond to the realistic extremes of energies occurring during ground vehicle incidents. The impact energy can be estimated as the area under the load-displacement curve.

Displacement-controlled tests would be performed at identical loading rates but each subsequent load cycle will have increased maximum displacement / skin indentation. The loading profile will consist of three phases: loading, hold and unloading, as illustrated in Figure 29(a). Phase 2 represents the period during which a ground service vehicle is pushing into the fuselage before reversing. Furthermore, two different approaches can be selected for Phase 1: quasi-static loading or slow dynamic loading as shown in Figure 29(b).

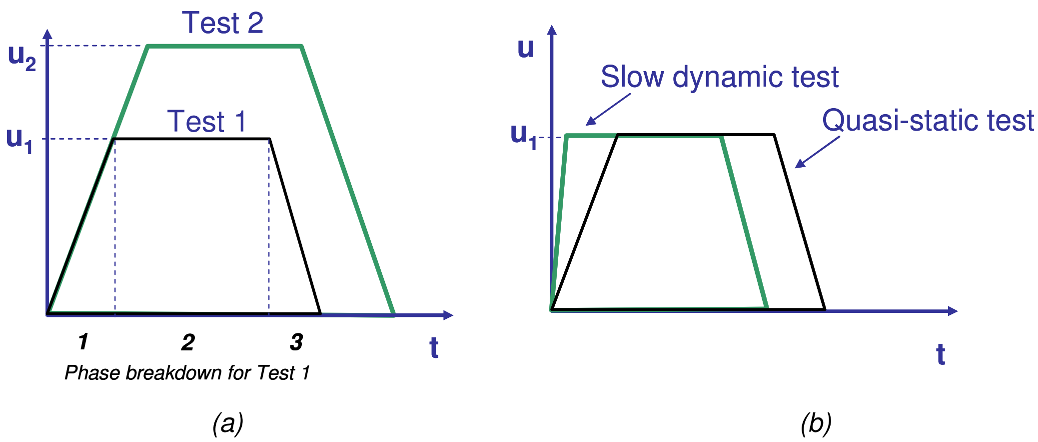

Figure 29. Displacement-controlled test: (a) comparison of displacement-time curve for two subsequent tests with identical loading rate (b) comparison of tests with two different loading rates

The quasi-static loading approach is suggested to be conducted at a loading rate of approximately 1-5 mm / min. This would allow careful monitoring during the loading of the panel. Test 1 would be terminated after the initial damage initiation.

Advantages:

- There are no requirements to specially define the test stop-points (u1 and u2) prior to each loading
- The test method is similar to the approach adopted by UCSD in their previous experimental programs on smaller scale panels

Disadvantages

- Quasi-static loading does not fully represent a real-life scenario.

The slow dynamic loading approach would be conducted at a loading rate of about 100 mm / sec. Thus, the duration of Phase 1 (loading) of the test will be relatively short, in order of one to two seconds.

Advantages

- Loading rate is more representative of the actual impact by a ground service vehicle.

Disadvantages

- Higher risk associated with challenges related to damage monitoring and performance of the test fixtures.
- Maximum displacement or skin indentation must be determined using numerical simulations.
- Test cannot be stopped when damage initiates.

3.3.4 Selection of the test method

Evaluating all aspects of the different test methods, the quasi-static displacement controlled test was selected for the first series of tests. This method was in agreement with the existing research program and due to enhanced control of test parameters and simple damage monitoring solutions, involved relatively low project risk.

After the completion of the initial test program, the performance of the test panel and test fixtures will be demonstrated. Therefore, in the subsequent test programs, a slow dynamic or crash test could be considered in order to increase the degree of realism in order to simulate a typical blunt impact scenario occurring during aircraft ground operations.

4 Numerical modelling

For numerical investigations, FE models were created using Abaqus software. The Abaqus 6.10 CAE pre-processor and Python script were used to generate the models. Two different FE models were generated: the test panel and a section of a complete fuselage barrel. Numerical simulations of the blunt impact by a rubber bumper were conducted using the Abaqus/Explicit and Abaqus/Standard solver version 6.10.

4.1 Description of the FE models

In the preliminary stage, a fully elastic FE model was created, which did not contain any material failure models, plasticity, degradation of properties nor failing part connections. The objective of the first analysis was to determine the generic elastic behaviour of the panel and the barrel FE models. These models also assisted in determining the energy level of the impact and investigating the required boundary conditions for the panel in order to replicate the behaviour of the full barrel FE model

4.1.1 General

The panel FE model was generated by modelling all parts in accordance with the engineering drawings for the test specimen. Four main parts, skin, shear ties, frames and stringers were separately modelled by shell elements with defined mid-plane offsets. An appropriate offset was specified according to the positioning of the parts to account for the actual physical thickness. The impactor consisted of the rubber bumper (forward section) and a flat plate of rigid material (aft section). The desired mass of the impacting ground vehicle was defined by the plate density. The FE model with the impactor is depicted in Figure 30.

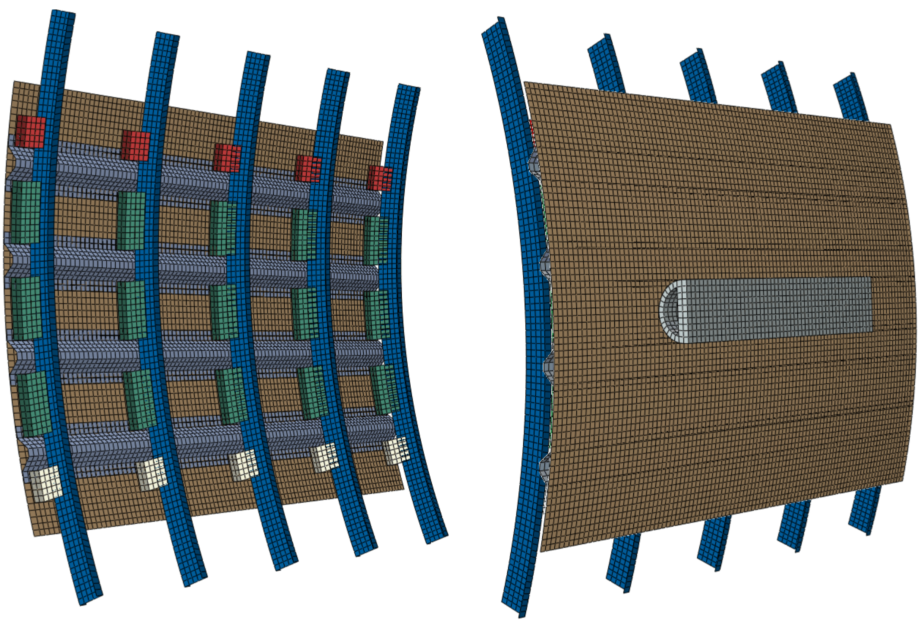

Figure 30. Test panel model: inside, outside view

As mentioned previously, in order to understand the required boundary conditions for the test which was intended to replicate the behaviour of the full fuselage, an additional FE model of the complete fuselage barrel was generated. As shown in Figure 31, the barrel FE model includes a detailed section with the properties of the test panel FE model, a transition zone and a simplified far field global section. The size of these sections is summarised in Table 5.

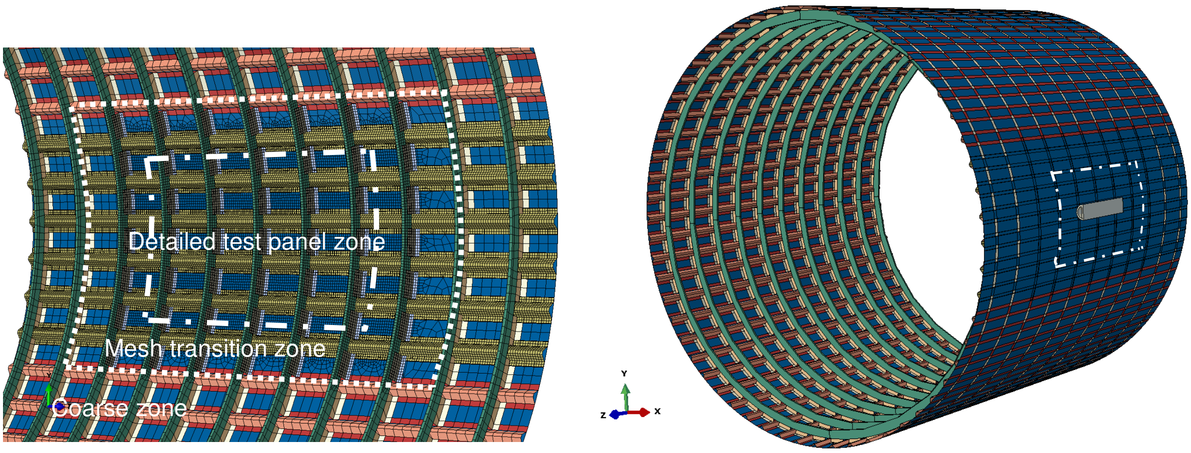

Figure 31. Different mesh density zones of the barrel model: inside detailed view, outside overview

Table 5. Number of stiffeners in the test panel and barrel model

	Test Panel Model	Barrel Model (detailed)
Number of Frames	5	11 (7)
Number of Stringers	4	58 (6)

The modelling of the global coarse zone was simplified to increase computational efficiency. This included:

- Shear ties and stringer feet plies merged within the skin lay-up
- Simple modelling of shear tie webs-to-frame attachments by merged surfaces
- Coarse zone modelled as one part, connection between the parts was done by common nodal points rather than by using contact definitions

4.1.2 Materials

As indicated previously, the hybrid design panel was manufactured using CFRP UD prepreg and CFRP fabric prepreg for the skin, stringers and shear ties. The metallic frames were made of aluminium.

4.1.3 FE Mesh

Shell parts of both models were generated using reduced integration quad shell elements (S4R). The panel FE model was meshed with elements of a nominal size of 20 mm. An identical size was also applied to the detailed zone of the barrel FE model. The coarse zone of the barrel FE model used an element size of 80 mm. For the impactor and attached plate, reduced integration hex elements (C3D8R) were selected.

4.1.4 Boundary conditions

In the initial numerical simulations, the test panel FE model was fixed in all degrees of freedom at the frame ends, see Figure 32. Compared to the aircraft-level deformation, these boundary conditions were expected to generate stiffer behaviour due to the absence of the surrounding fuselage structure. In the barrel FE model, it was assumed that the fixity of remote edges (see Figure 33) would only cause negligible error and therefore this simplified boundary condition was appropriate to simulate deformation of the aircraft fuselage subjected to high energy blunt impact.

In both FE models, the impactor mass of 2000 kg was modelled as a rigid plate attached to the rubber bumper with an appropriate density value. Based on the review, this mass represented a typical ground service vehicle such as a belt loader. The impactor was given an initial velocity of 5 km/h.

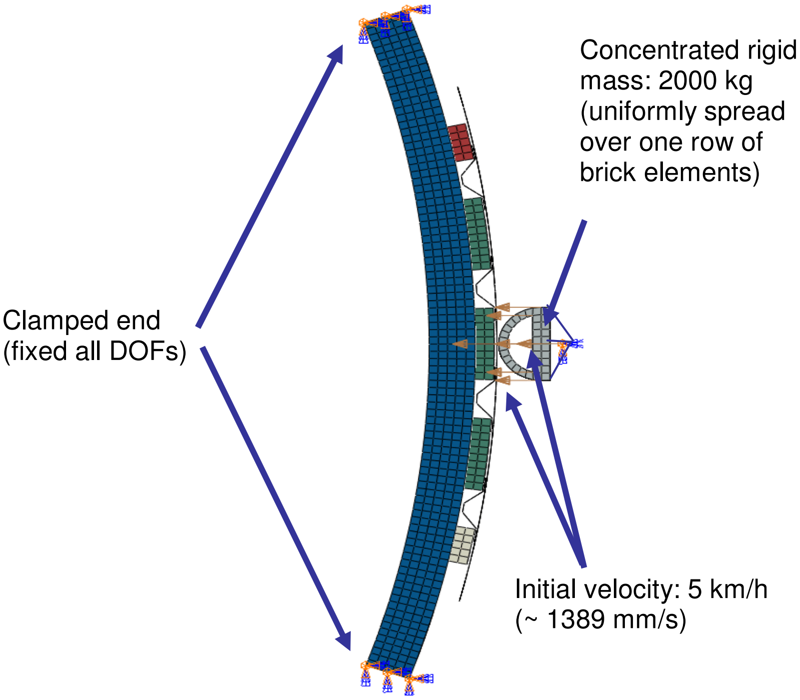

Figure 32. Boundary conditions of the panel FE model

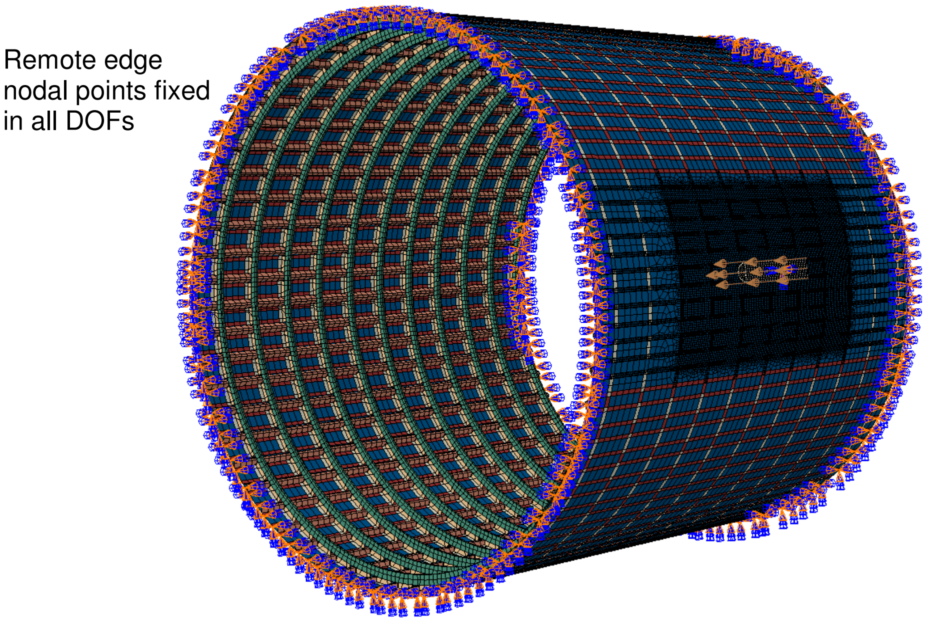

Figure 33. Boundary conditions of barrel FE model

4.1.5 Contact definitions

Contact was defined between the impactor bumper and the skin. Bonding and fastening of the parts in the initial FE models were simply generated using tie constraints. These connect degrees of freedom of contact pairs on a node-wise basis. The bondline was defined without any failure model.

4.2 Results and discussion: panel FE model vs. barrel FE model

A deformation pattern of the barrel FE model was found to cover approximately half of the circumference as shown in Figure 34. As expected, the maximum deformation occurred in the impact region; however, a small nodal displacement was also predicted at the upper fuselage.

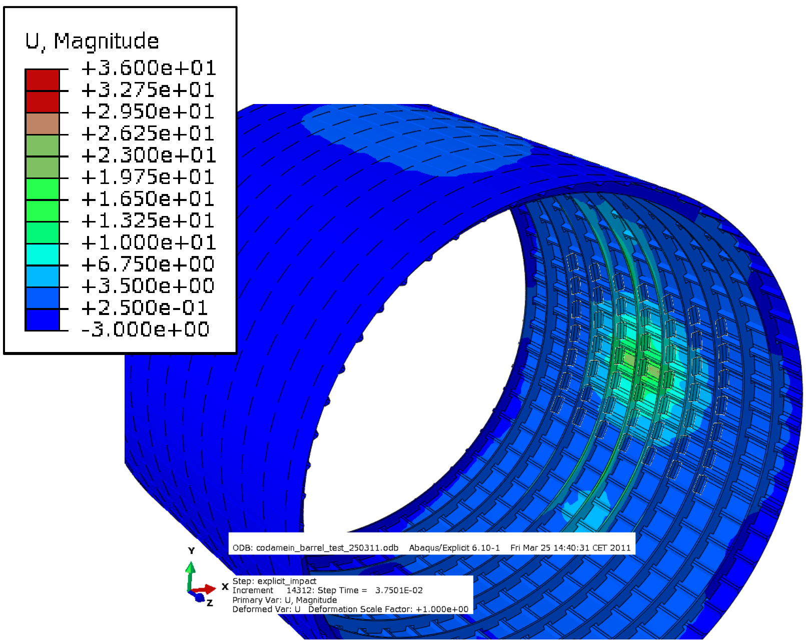

Figure 34. Barrel FE model: Displacement in the impact direction

A comparison of the overall deformation in the impact region is presented in Figure 35. The maximum displacement in the panel FE model was found to be 31.1 mm while the barrel FE model showed a maximum displacement of 35.6 mm. The displacement field in the impact direction was not entirely identical, due to the different boundary conditions. The maximum indentation was in the central skin bays, while the two outer frames showed very small displacement. The load transfer through the outer frames was found to be minimal since only the inner three frames were loaded by the impactor. The numerical prediction indicated that outer frames carried less than 10% of the total reaction load measured at the frame attachment points. Consequently, this provided a strong indication that only three frame attachments for the testing could be considered.

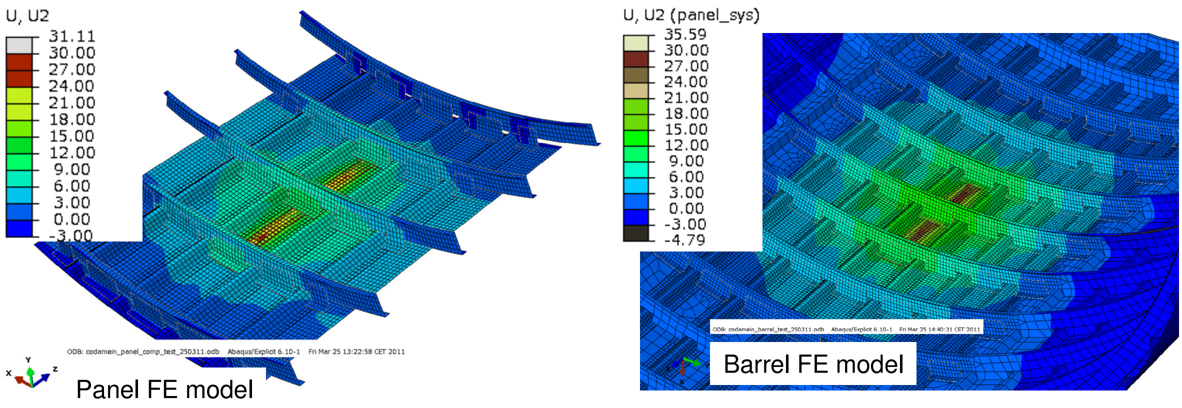

Figure 35. Displacement in impact direction: Test panel FE model and barrel FE model

Explicit FE analyses were run until 50 ms after the impact. Displacement versus time predictions for the two models are presented in Figure 36(a). The results again confirmed more flexible behaviour of the barrel FE model as well as a time shift for the maximum displacement. This was predicted at 32.5 ms in the panel FE model and at 37.5 ms in the barrel FE model. Thus, impactor displacement (movement of the rigid part of the impactor) was found to be 16% higher for the barrel model. After reaching the maximum displacement, a rebound of the impactor was predicted, confirmed by the impactor velocity vs. time plot presented in Figure 36(b).

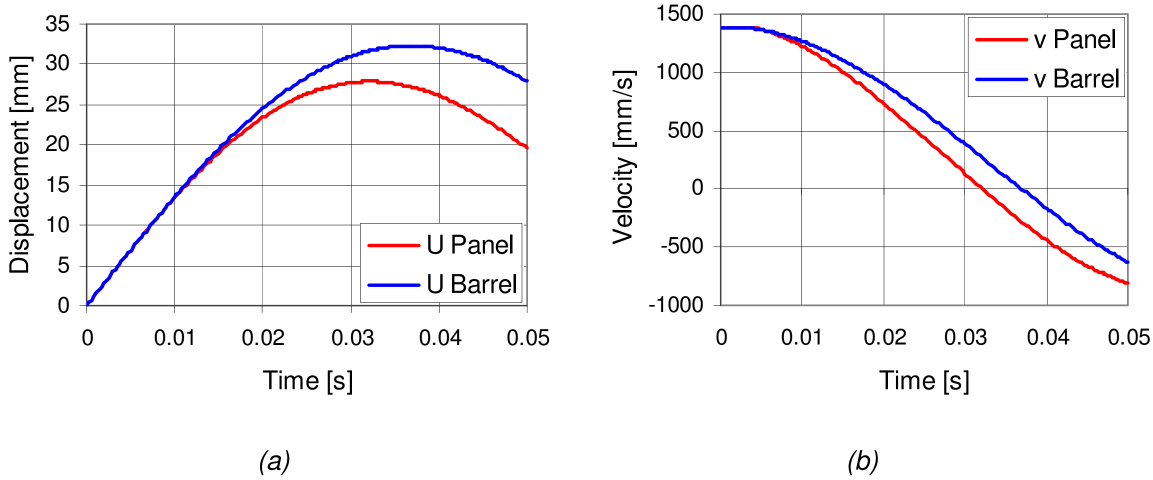

Figure 36. (a) Impactor displacement vs. time, (b) Impactor velocity vs. time for the test panel FE model and the barrel FE model

The initial kinetic energy of the impactor was compared with the expected analytical value which is given by:

$$E_k = \frac{1}{2}mv^2 = \frac{1}{2} \times 2008 \times 1.39^2 = 1940\ J$$

As shown in Figure 37, the expected initial value corresponded to the numerical predictions which validated numerical input data in the impact simulations. Note, the magnitude of the initial kinetic energy was in the upper bound of the energy level range discussed in Section 2.2.3.

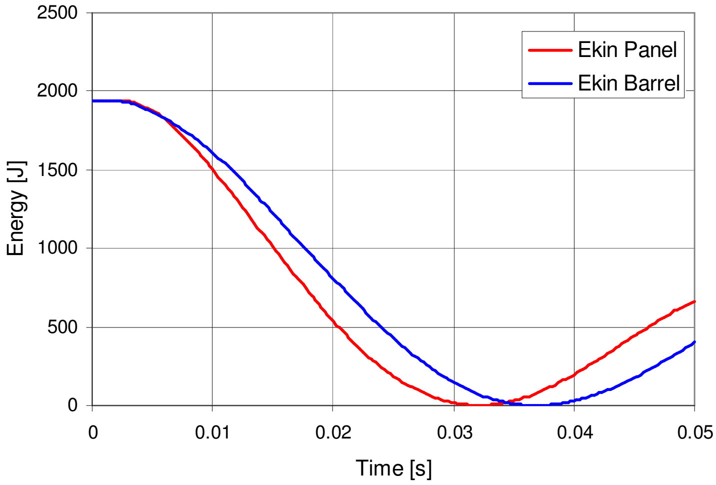

Figure 37. Impactor kinetic energy vs. time

FE simulations of the panel model and the barrel model confirmed the necessity to include some elastic deformation of the attachments at the frame ends instead of clamping them rigidly. In order to investigate the required stiffness for the test fixtures that would replicate barrel-like boundary conditions, deformation results of the frame attachment points in both models were investigated. Positions of these nodal points are highlighted in Figure 38.

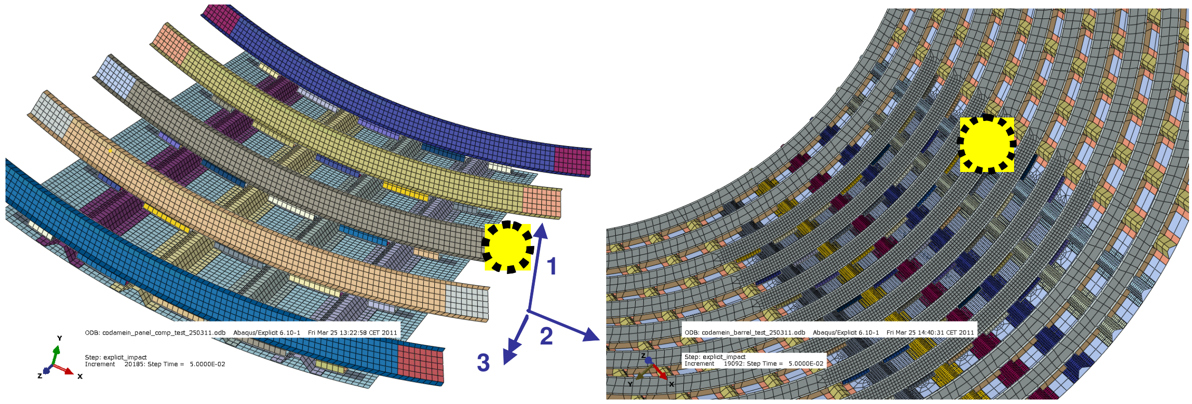

(a) (b)

Figure 38. Location of the attachment nodal points: (a) in the panel model, (b) in the barrel model

Displacement predictions for the attachment points are presented in Figure 39(a) and Figure 39(b) for the impact direction and normal direction, respectively. As expected, due to fixed BCs in the panel FE model, the displacement of the frame ends was negligible. For the given impact case, it was predicted that the test fixtures should provide an approximate 3.5 mm movement in the impact direction and 2.0 mm displacement in the normal direction. This impact case is used as a nominal event to design test fixtures to replicate aircraft-like boundary conditions.

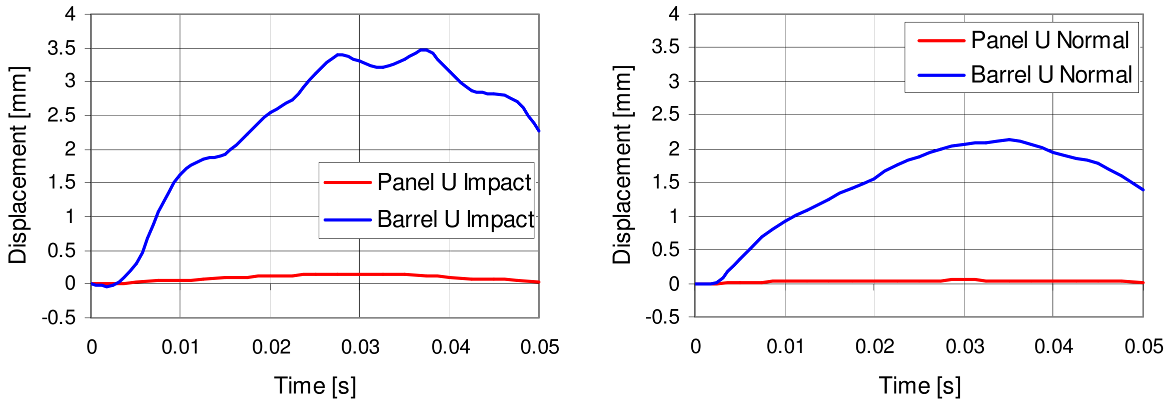

(a) (b)

Figure 39. Displacement of the single node at the end of the frame showing (a) impact direction and (b) normal direction

In conclusion, the results of the first step analysis of the test panel model and the barrel model justified the assumptions made. The impactor's kinetic energy before impact was transferred in elastic strain energy during impact. The FE model of the panel showed significantly stiffer behaviour than the barrel

FE model. Numerical predictions of deformations in the impact region as well as in the panel boundary region highlighted the necessity of developing appropriate boundary conditions for the actual test article to incorporate flexibility of the surrounding structure that was not present in the test of the stiffened panel.

4.3 Further development of the FE models

In line with the decision to perform a quasi-static test, the FE models of the test panel were modified and analysed using the Abaqus standard (implicit) solver instead of the Abaqus explicit solver. Additional modifications, summarised in the following section, were incorporated

4.3.1 Materials

The material properties were extended to incorporate plastic properties for the aluminium frames with the yield strength set to 462 MPa, plastic modulus of 3004 MPa and ultimate strength of 538 MPa. For composite material cards, Hashin fibre and matrix damage initiation criteria were included. The Hashin criteria predicts failure initiation using the following four damage mechanisms for fibre tension, fibre compression, matrix tension and matrix compression:

Fibre tension $(\hat{\sigma}_{11} \geq 0)$:

$$F_f^t = \left(\frac{\hat{\sigma}_{11}}{X^T}\right)^2 + \alpha\left(\frac{\hat{\tau}_{12}}{S^L}\right)^2$$

Fibre compression $(\hat{\sigma}_{11} < 0)$:

$$F_f^c = \left(\frac{\hat{\sigma}_{11}}{X^C}\right)^2$$

Matrix tension $(\hat{\sigma}_{22} \geq 0)$:

$$F_m^t = \left(\frac{\hat{\sigma}_{22}}{Y^T}\right)^2 + \left(\frac{\hat{\tau}_{12}}{S^L}\right)^2$$

Matrix compression $(\hat{\sigma}_{22} < 0)$:

$$F_m^c = \left(\frac{\hat{\sigma}_{22}}{2S^T}\right)^2 + \left[\left(\frac{Y^C}{2S^T}\right)^2 - 1\right]\frac{\hat{\sigma}_{22}}{Y^C} + \left(\frac{\hat{\tau}_{12}}{S^L}\right)^2$$

Where F_f^t and F_f^c are the damage criteria for fibre tension and fibre compression, while F_m^t and F_m^c are the damage criteria for matrix tension and matrix compression. The effective stress tensors $\hat{\sigma}_{11}$, $\hat{\sigma}_{22}$ and $\hat{\tau}_{12}$ are the components in fibre direction, normal to fibre direction and in-plane shear identical to σ_{11}, σ_{22} and τ_{12} prior to the first damage initiation. X^T and X^C represent the fibre direction tensile and compression strength, Y^T and Y^C are the transverse tension and compression strength while S^L and S^T are the longitudinal and transverse shear strength. The coefficient α determines the contribution of the shear stress to the fibre tensile failure initiation criterion.

4.3.2 Connector elements

Further development of the numerical models included shear ties-to-skin and shear ties-to-frames connections which were changed from surface tie connections to point-to-point constraints using fastener elements. Fastener elements in Abaqus are modelled between two surfaces using control points which were created to precisely represent the locations of the Hi Loc rivets. The fastener elements, defined with a nominal diameter of 6 mm, constrained all six degrees of freedom of the corresponding points of the connection surfaces (see Figure 40). The fasteners were assumed to be rigid elements.

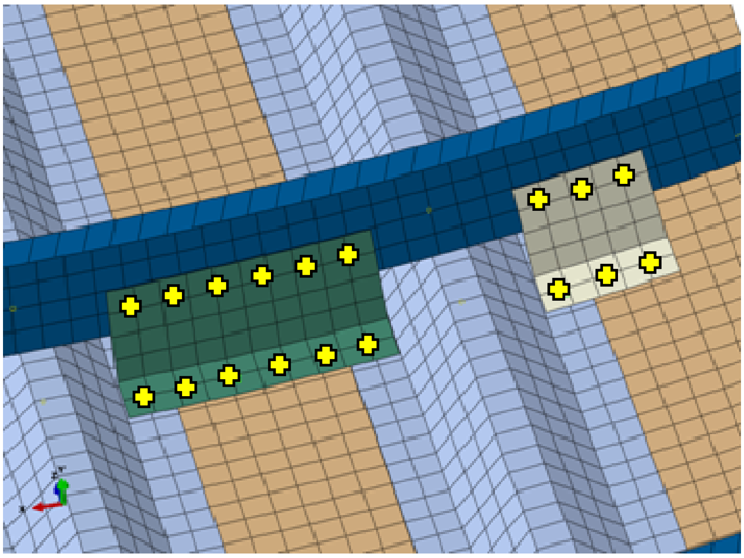

Figure 40 Fastener positions at shear ties, frames and the skin

4.3.3 Rubber bumper modelling

The D-shaped rubber bumper, which was used for the first series of analyses, was replaced by a circular bumper which represented the actual OEM part used in the tests. The circular section of the bumper was expected to completely close at a relatively low load level. In order to avoid convergence issues and avoid the use of an extremely fine mesh required for such hyperelastic simulation, a decision was made to model the bumper as a representative flat section. The mesh of the original D-shaped bumper section and the flattened bumper shape are shown in Figure 41.

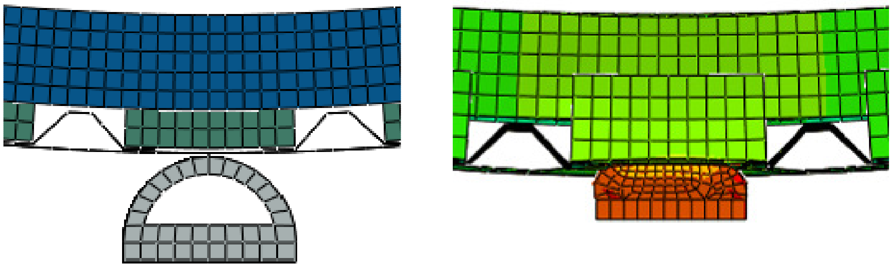

Figure 41 Mesh of the rubber bumper section: D-shape, flattened shape

4.3.4 Boundary conditions

The boundary conditions for the test were developed based on the outcomes of the dynamic FE analysis. To incorporate the flexibility of the surrounding structure in the panel FE model, hoop direction (normal to impact) spring elements were attached to one end of the three inner frames. A pinned connection allowed for axial rotation around the joint's axis and the springs permitted translational displacement which was driven by the spring stiffness. A parametric study was conducted to investigate the sensitivity of the panel's skin deformation on the spring stiffness. The spring constants were set between 40 kN / mm and 8.5 kN /mm. The frame attachments at the second end of the three central frames were constrained in all translational degrees of freedom allowing axial rotation of the joint. The defined boundary conditions, applied to the three inner frames, are illustrated in Figure 42.

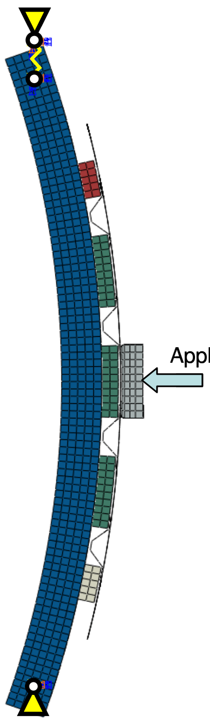

Figure 42. Modified boundary conditions

4.4 Results and discussions: FE models with spring-based BCs

The results of the parametric study are shown in Figure 43. The graph compares load vs. skin displacement for the barrel FE model and the results obtained from the four spring-based panel FE models. It can be seen that the spring stiffness significantly affected the behaviour of the panel. As expected, softer spring elements provided better correlation with the results from the barrel FE model. The FE model that contained spring elements with the spring constant of 8.5 kN / mm exhibited a good agreement with the barrel model, especially between 0 – 30 kN and later at the higher load segment between 120 kN – 140 kN. The differences between panel and barrel FE model could have been attributed to the use of simplified boundary conditions in the panel FE model as well as to the different numerical methods (the panel model was analysed using the implicit non-linear solver whereas the barrel model was analysed using the explicit solver). Therefore, it is recommended to conduct further implicit FE simulation using the barrel FE model. The FE model of the panel which used springs at one side of the three inner frames, showed a good agreement with the barrel model in terms of displacement of the frame ends. The capability of the spring-based panel model to represent the behaviour of the barrel was further investigated by a comparison of the stress distribution in the highest stressed central region. This also showed a satisfactory agreement.

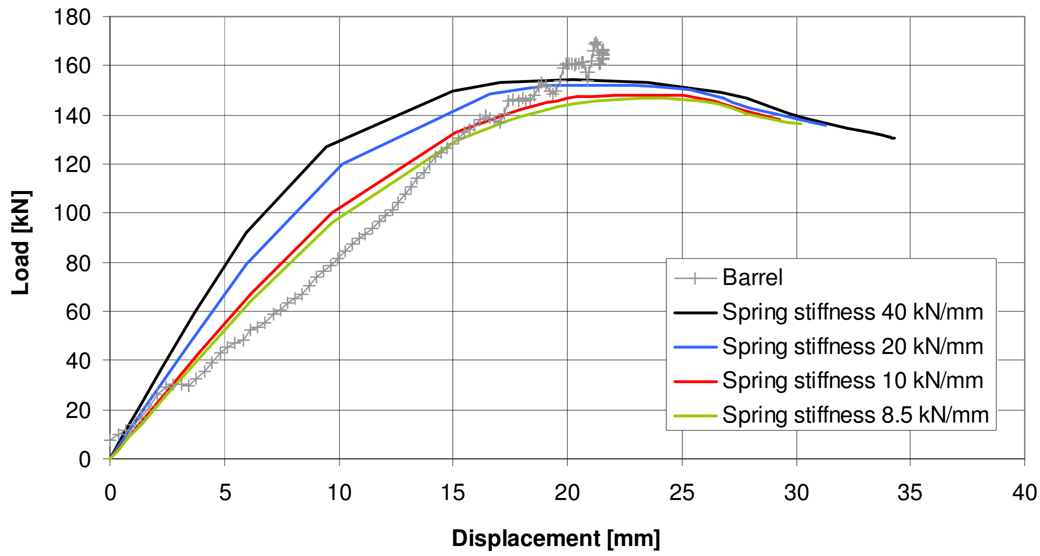

Figure 43 Load-displacement chart of the panel model using different spring stiffnesses

Previous test data from UCSD (Kim 2011b) using a three-frame test panel of a comparable design assisted in approximate analytical determination of the expected damage initiation load. In this research, damage initiation was reported to occur at 28.70 kN. The load was applied across two frames; thus the normalised failure initiation load per frame was calculated as 14.35 kN. Subsequently, this yielded a failure initiation load of 43.05 kN for the panel loaded across three frames.

The numerical analysis was conducted up to an impactor displacement of 28 mm. At this point a maximum load of 143 kN was predicted which was well beyond the expected failure initiation load. Contour plots of the displacement in the impact direction at 52 kN and at the maximum load are presented in Figure 44. Maximum skin indentation was predicted in the central skin bays between the frames. With increasing load, evident deformation of the skin was being extended towards the edges of the panel.

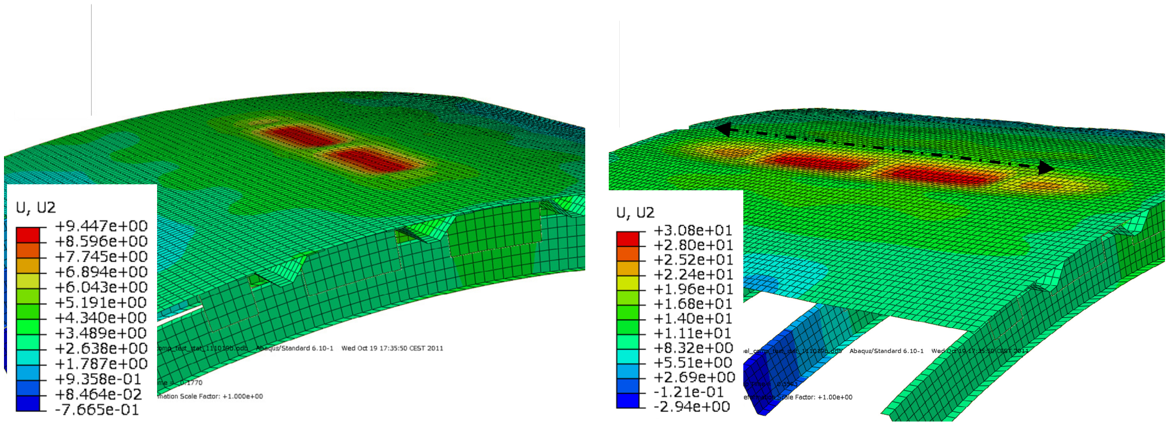

(a) (b)

Figure 44. Skin displacement in the impact direction at (a) 52 kN and (b) 143 kN

The numerical prediction of the radial strains at the load of 52 kN, shown in Figure 45 (a), indicated a maximum strain level of approximately 2600 με in compression. Accumulation of fibre strain in the shear tie flanges were observed, particularly at those located directly under the rubber impactor. A contour plot of the shear strain is shown in Figure 45 (b). While the central shear ties were mainly subjected to compression, the level of shear strain increased from the central shear ties towards the outer ones.

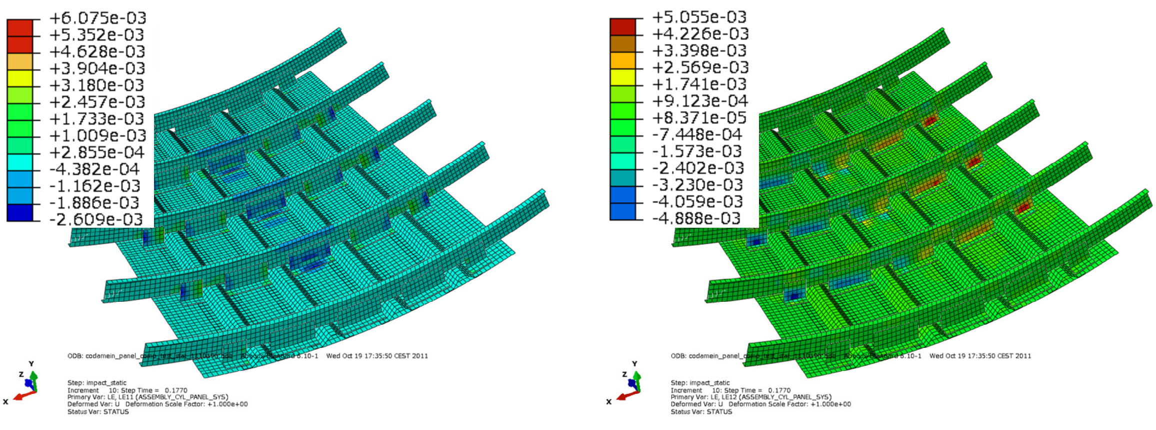

(a) (b)

Figure 45. Strain field in the shear ties (a) radial direction and (b) shear resultant

The strain field of the outer skin is presented in Figure 46. The axial strain (stringer direction) showed tensile and compression peaks at the locations of indentation. Due to the bending of the skin bays, the maximum tensile strain was reached under the shear tie feet surrounded by regions of maximum compression in the skin bay. In the circumferential direction (frame direction) the outer skin surface of the central skin bays was subjected to compression while the inner flanges of the central frames were loaded in tension. Numerical simulation additionally showed compression loading at the frame outer flanges.

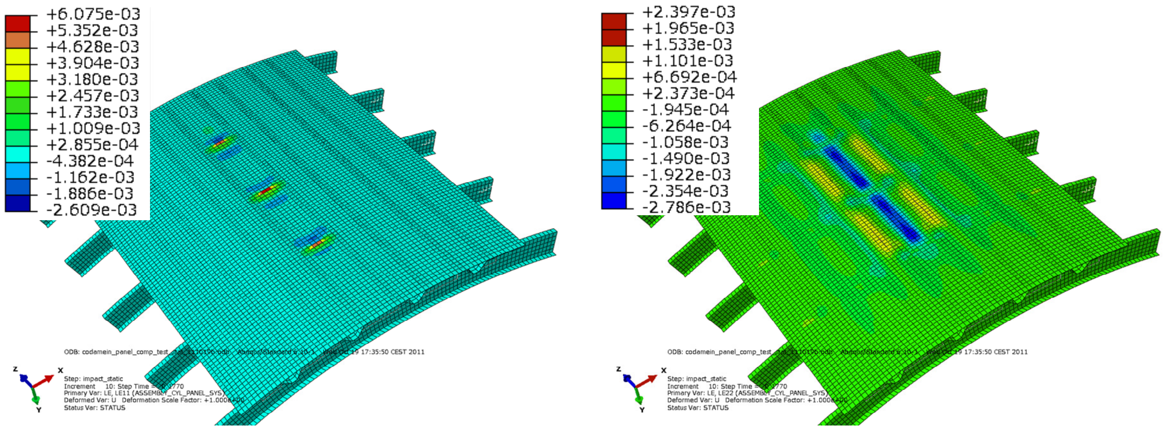

(a) *(b)*

Figure 46. Outer skin strain field in the (a) stringer direction and (b) frame direction

The FE model exhibited no plastic deformation of the frames up to the load of 123 kN. After exceeding this load level, the frames showed first signs of plasticity at the vicinity of the outer attachment points. With increasing load, progressive twisting of the Z-profile aluminium frames was observed as shown in Figure 47. Deformation of the cross-section introduced additional bending and shear load in the shear ties.

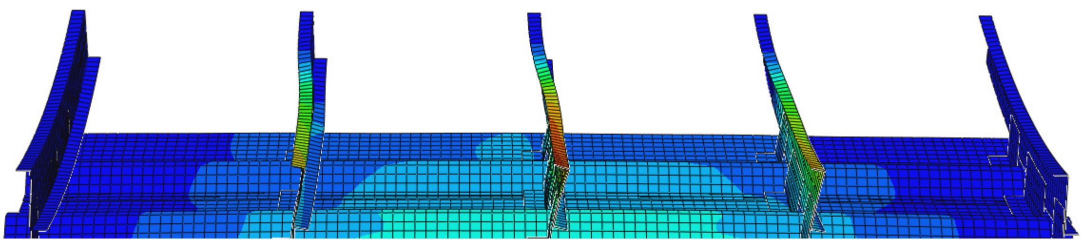

Figure 47. Twisting of the frames

Based on the results from numerical simulations, the following test predictions were made:

- Outer skin would visibly deform in the central skin bays; maximum skin displacement of 15 mm was predicted at 123 kN load
- Damage initiation at the shear ties was anticipated (predicted first failure mode)
- Twisting of the Z-profile frames was expected
- At high load levels, the increasing skin deformation was expected to cause a reduction of the clearance between the stringers and frames and therefore, a possible contact of these parts was anticipated.

5 Testing

Based on the results from the numerical simulations, test fixtures that replicate full barrel behaviour were manufactured. Details are provided in the following section.

5.1 Boundary conditions

The tooling was designed using the CATIA CAD program and Abaqus FE software. All parts were analysed considering the most critical load case and designed with a safety factor of two. Three identical fixture sets were manufactured. The tooling consisted of three main subassemblies.

The pin joint fixture was designed for one frame end. This allowed for axial frame rotation at its attachment point. A 2D illustration of the test setup, showing the pinned fixtures, is provided in Figure 48, while the 3D model and actual parts are shown in Figure 49. The fixture was made up of a base platform and two pin joint support plates welded onto the base.

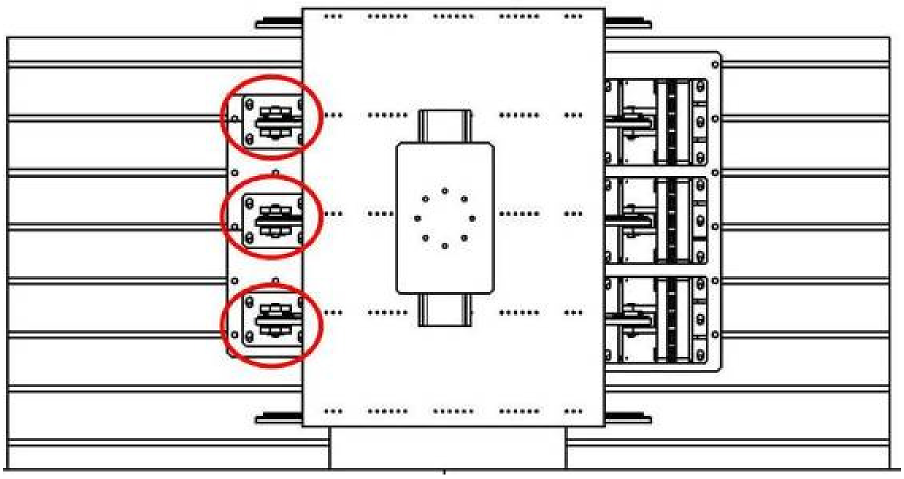

Figure 48. Pinned supports

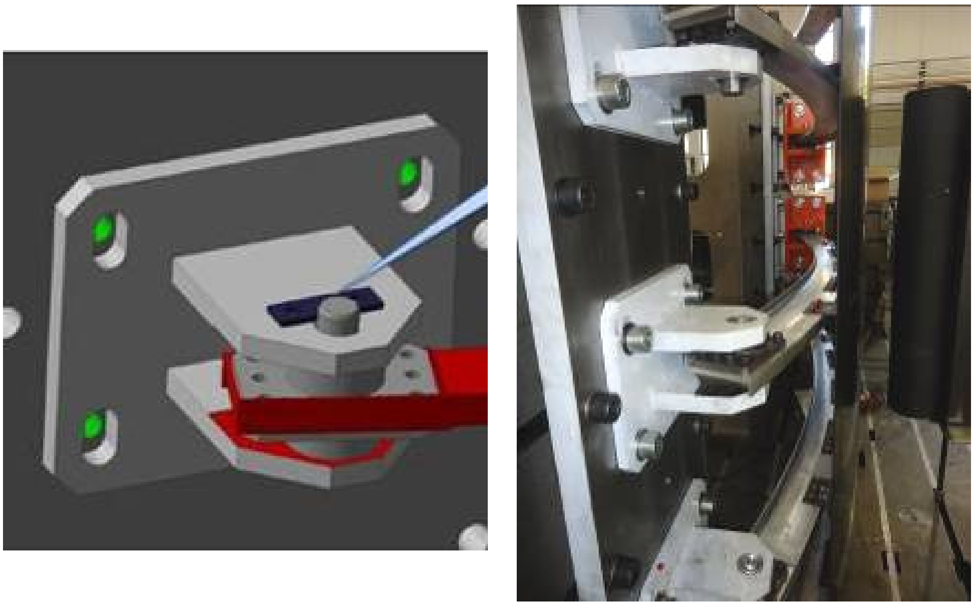

Figure 49. 3D model and the actual test fixture of the pinned supports

The second end of the frames was supported by a pin joint coupled with an elastic reaction fixture that allowed for axial frame rotation and linear displacement normal to the impact direction. Each frame attachment contained ten 850 N/mm springs mounted between a rigid plate and a sliding L-profile plate. Six inserted guide pins ensured parallel movement between the plates. A 2D illustration of the test setup, showing the pinned-spring fixtures, is provided in Figure 50 while the 3D model and the actual parts are shown in Figure 51.

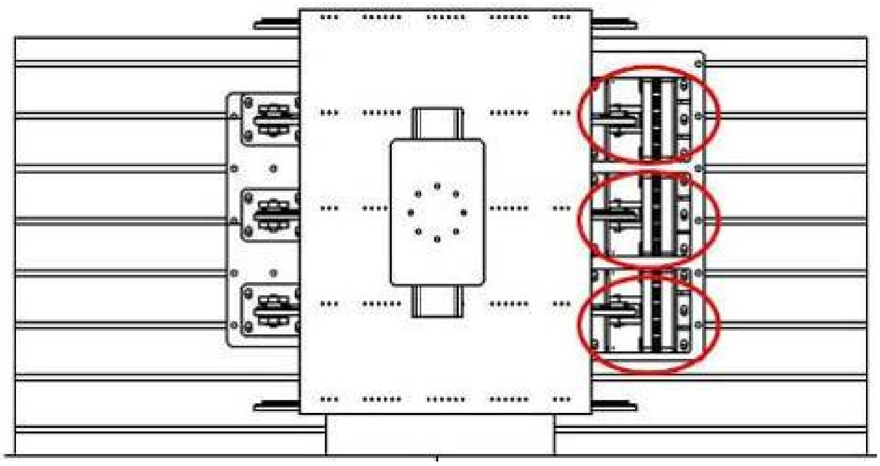

Figure 50. Pinned supports with elastic reactions

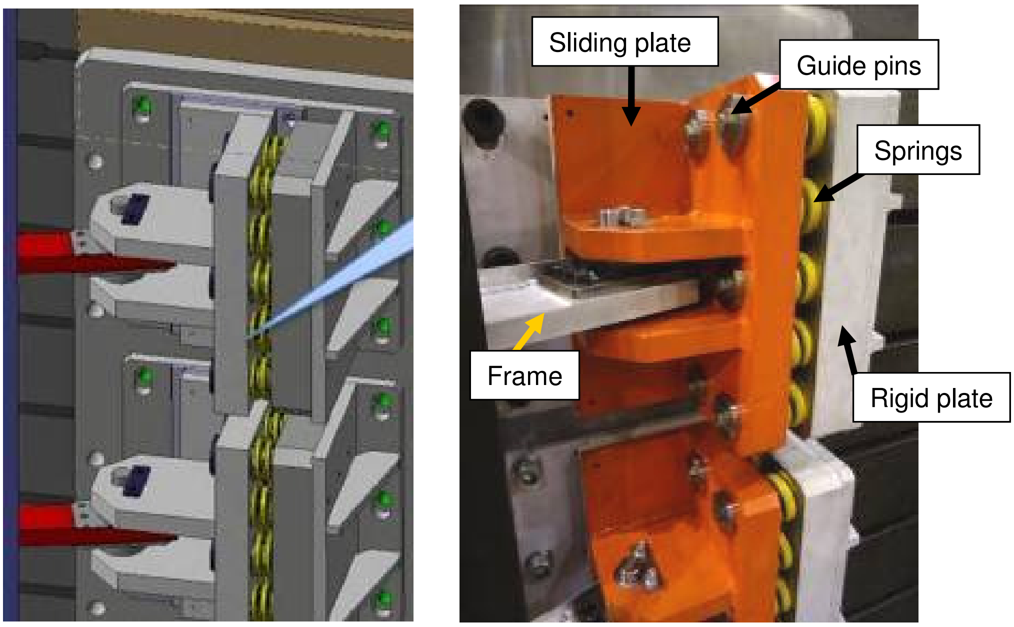

Figure 51. 3D model and the actual test fixture of the pinned supports with springs

Loading was introduced by a support structure with the bolted cylindrical rubber bumper. The bumper was bolted to the fixture using two allen screws. A 3D model of the sub-assembly and the actual rubber bumper attachment are shown in Figure 52.

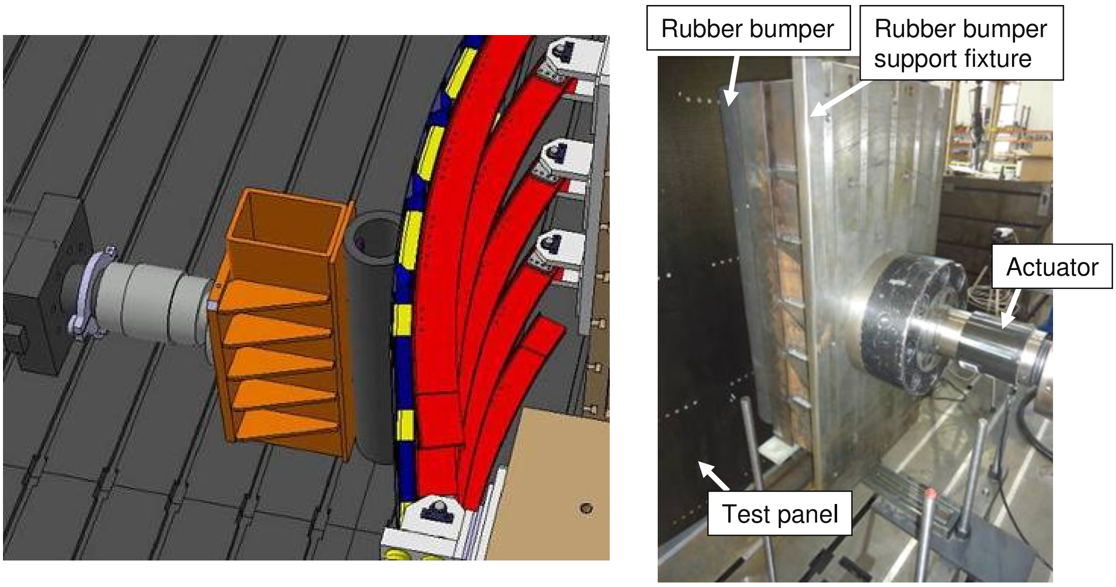

Figure 52. Rubber bumper attachment fixtures

In order to decrease the stress concentrations around the pin joints and to avoid premature failure of the frame attachments during testing, additional reinforcing steel plates were manufactured. The plates, shown in Figure 53, were bolted on each side of the frame ends using eight allen screws.

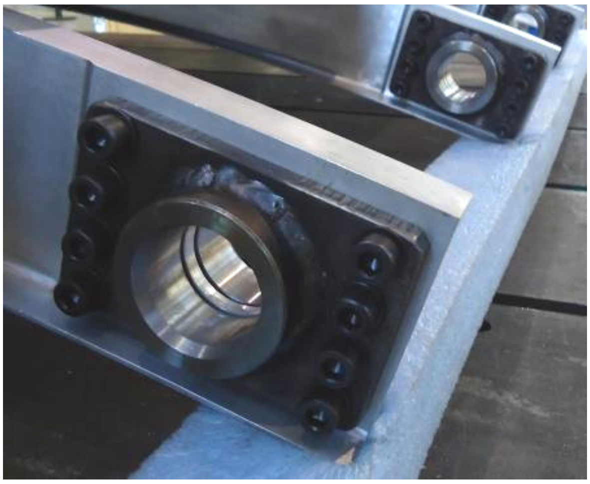

Figure 53. Reinforcement plates bolted to the frames

5.2 Test setup

The overall top view of the test setup is shown in Figure 54. The test setup consisted of three MTS strongwalls. These were rigidly mounted on the 12 x 12 m MTS strongfloor using M24 screws. Two strongwalls, separated by 1150 mm, held the frames of the test panel while the third was used to secure the base of the actuator. The test laboratory guaranteed a 0.25 mm alignment between all components of the assembly. The panel was loaded by the 1000 mm long OEM rubber bumper. The length of the bumper ensured that the load was directly applied across the three central frames. In the hoop direction, the bumper was placed symmetrically between the two central stringers. An overall view of the actual setup is shown in Figure 55.

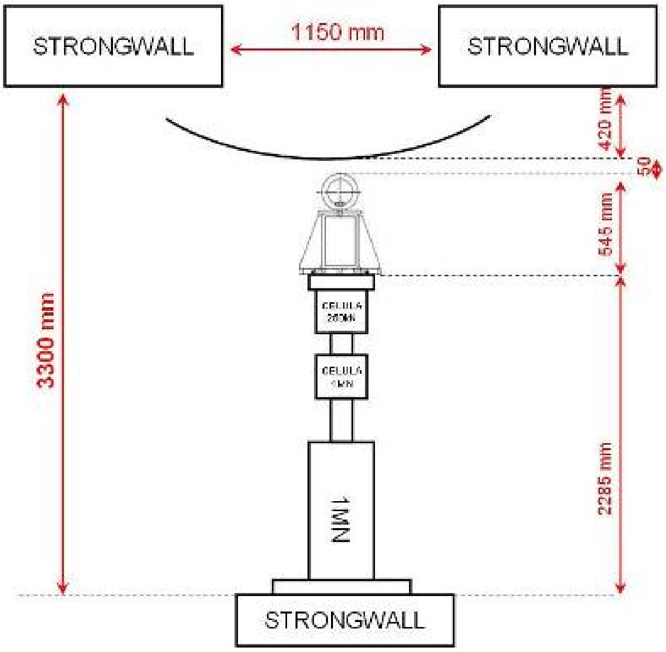

Figure 54. Top view of the test setup

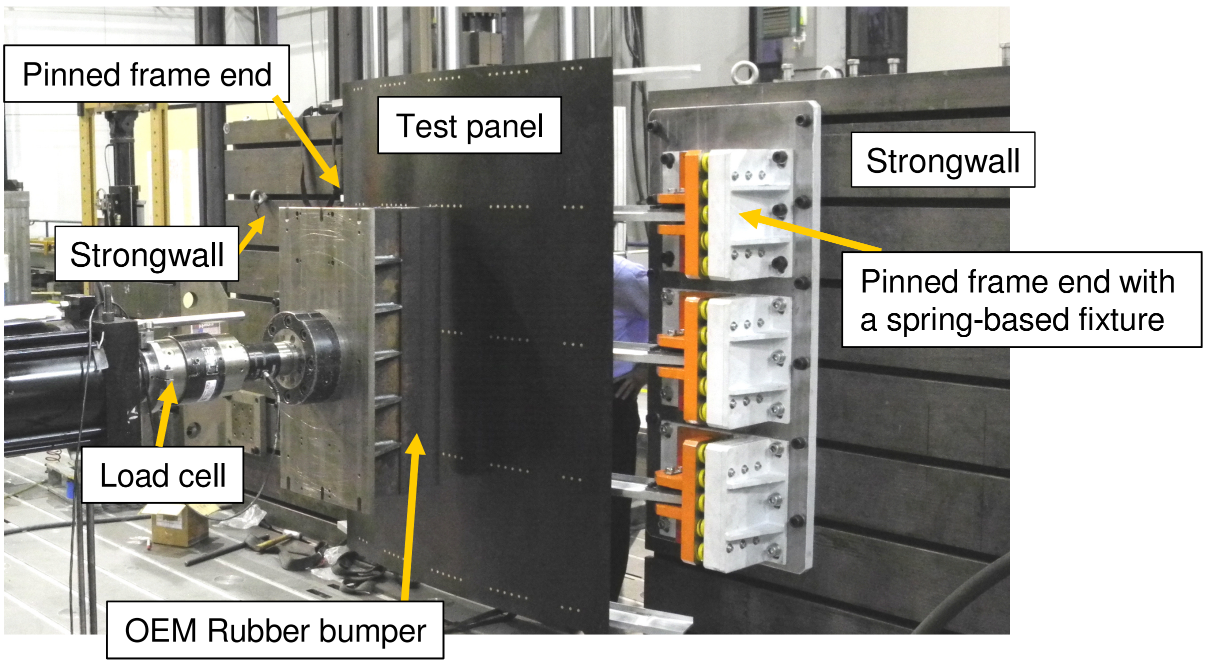

Figure 55. General test setup

5.3 Testing methodology

Panel deformation was monitored by two standard video cameras located at both the inner and outer sides of the panel. The skin displacement was measured by a linear variable differential transformer (LVDT) attached to the inner skin. The LVDT was placed 83 mm above the central frame web and it was centred in the hoop direction. A schematic of the data acquisition equipment is provided in Figure 56.

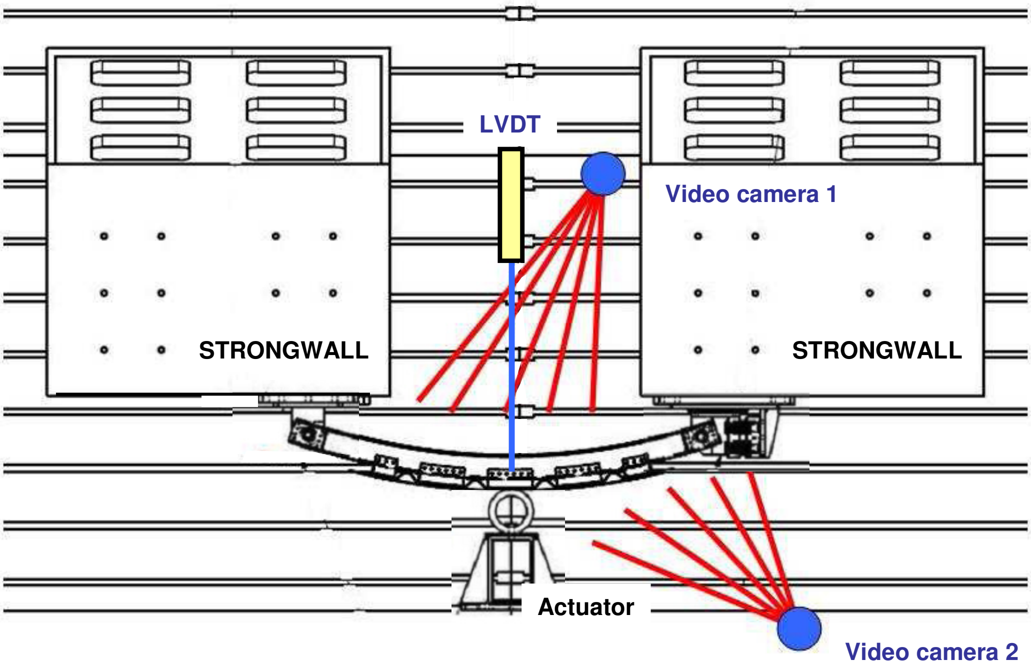

Figure 56. Location of the data acquisition equipment

Following the pre-test, which provided a final check of the test setup and the data acquisition equipment, three load cycles were applied to the panel. The panel was loaded quasi-statically according to the loading profile shown in Figure 57. An initial loading rate of 25 mm / min was selected until an actuator displacement of 100 mm was reached. At this point the rubber bumper was almost fully compacted; and therefore, the loading rate was reduced to 2 mm / min. The test machine's safety soft stop, specified by the actuator displacement, was set to halt the panel loading in case of an unexpected event. However, the actual maximum actuator displacement for each load cycle was not determined prior to testing. It was decided to stop the test at the following visual or audible events:

- Load cycle 1: First loud crack noise or pop / first measured load drop / damage initiation
- Load cycle 2: Visual damage of shear ties or stringers / damage propagation measured by a number of load drops

- Load cycle 3: Extensive shear tie or stringer damage / shear tie failure / frame-to-stringer contact / excessive rotation of the frames

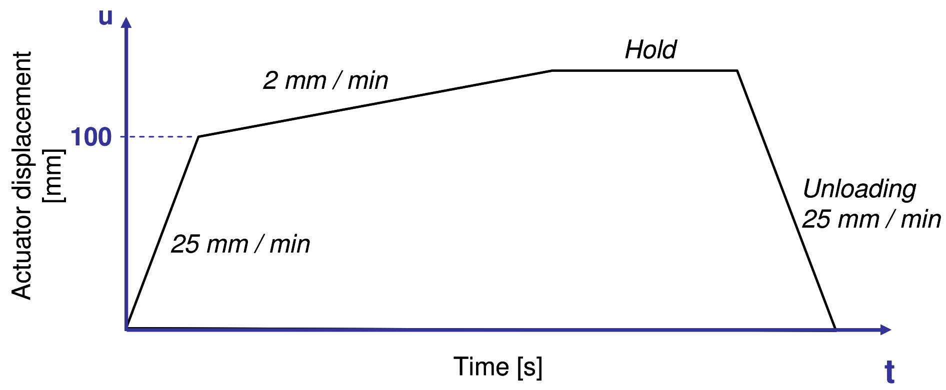

Figure 57. Loading of the panel

The data acquisition system recorded actuator displacement, load and LVDT displacement at a sampling rate of 10 Hz. Prior to testing and after each load cycle, the panel was examined visually and by non-destructive inspection using an ultrasonic 5 MHz A-scan hand held probe.

5.4 Test results

The panel was mounted on the strongwalls with the frames in the horizontal direction. In this report, the results and discussions will use a designation in which frame 1 (F1) is the bottom frame while the upper frame is denoted as frame 5 (F5). The shear tie designation scheme has a general form of shear tie X.X (STX.X), where the first digit specifies the frame attachment and the second digit indicates a frame-wise position from the left hand corner. Thus, shear tie 2.1 (ST2.1) was located on the left-hand edge of the frame 2 while shear tie 2.5 (ST2.5) was on the right-hand edge. All central shear ties were designated STX.3. Omega-profile stringers, S1 to S4, were also marked from left to right as depicted in Figure 58.

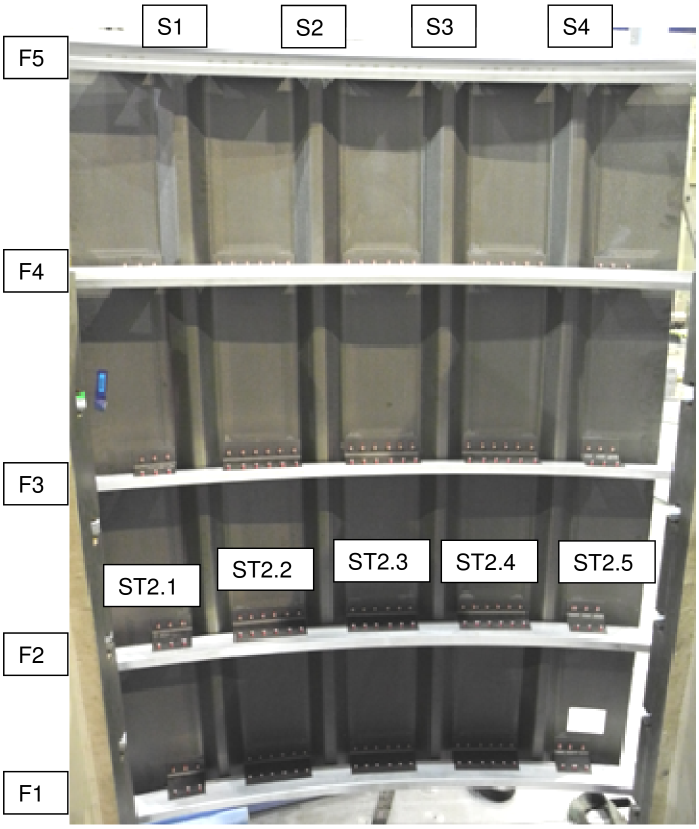

Figure 58. A numbering system for the panel

5.4.1 Load cycle 1

During the 1st loading cycle, the first slight ticking noise was recorded at 14 kN which corresponded to a displacement of 99 mm. This was followed by a visual full closure of the cylindrical bumper at approximately 110 mm actuator displacement and 20 kN load. From the load – displacement curve it was estimated that the full closure of the bumper required an energy of 740 J. The panel was steadily loaded from 20 kN to 35 kN and exhibited a relatively linear load – displacement response. Above 35 kN continuous clicking sounds were detected. The first loading was stopped after the first loud pop at a load of 46 kN and a skin displacement of 13 mm. As the actuator was kept at the maximum displacement, the load gradually decreased to 43 kN while continuous clicks were heard. The panel outer skin side, viewed from both attachment sides, at the maximum actuator displacement is shown in Figure 59. After unloading, no damage was detectable by both visual inspection and an ultrasonic A-scan examination. Although not detectable, it was presumed that the loud pop noise and the associated load drop was a result of damage initiation at a shear tie radius region which was indicated by the numerical predictions.

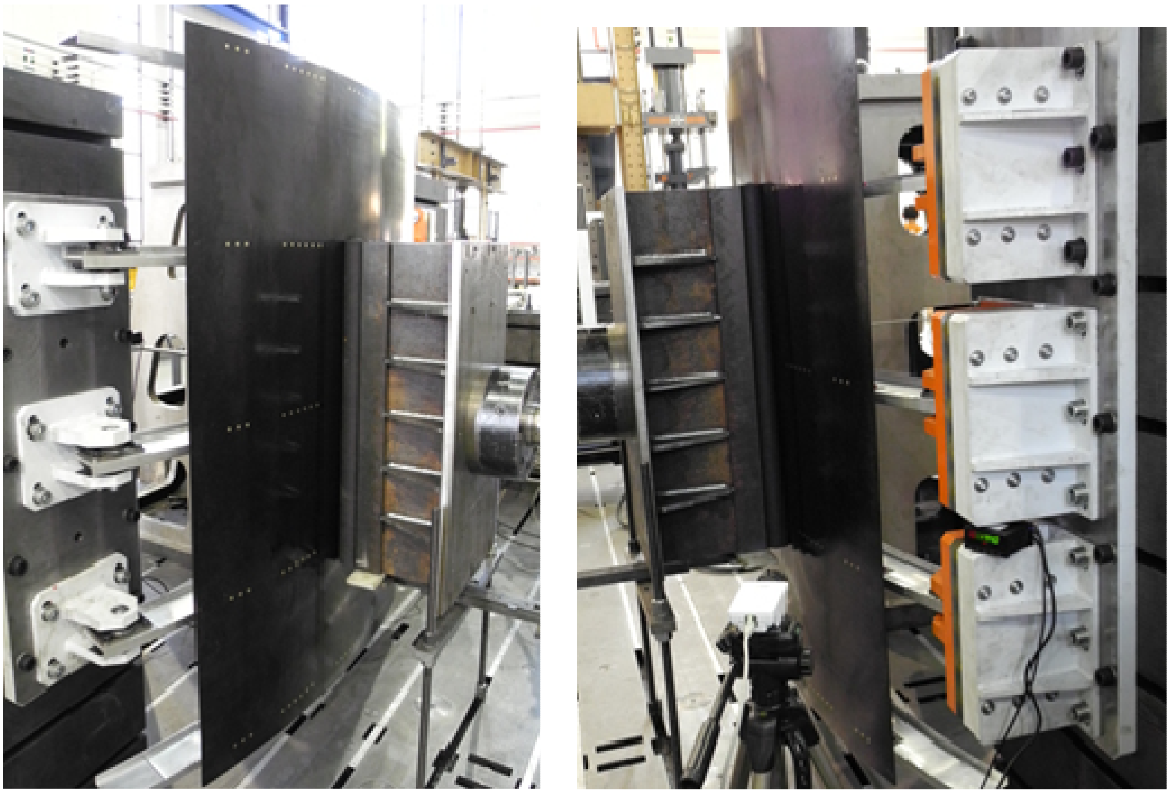

Figure 59. View of the outer skin side at the maximum displacement of the 1st load cycle

The load-displacement plot is presented in Figure 60 showing both actuator and skin displacement. The plot shows an initial nonlinear plateau region during which the rubber bumper was being compressed. After the full closure of the bumper, the stiffness increased significantly. A detailed view of the last 5 mm of actuator displacement, during which a continuous clicking noise was observed, exhibits one minor load drop at 38 kN.

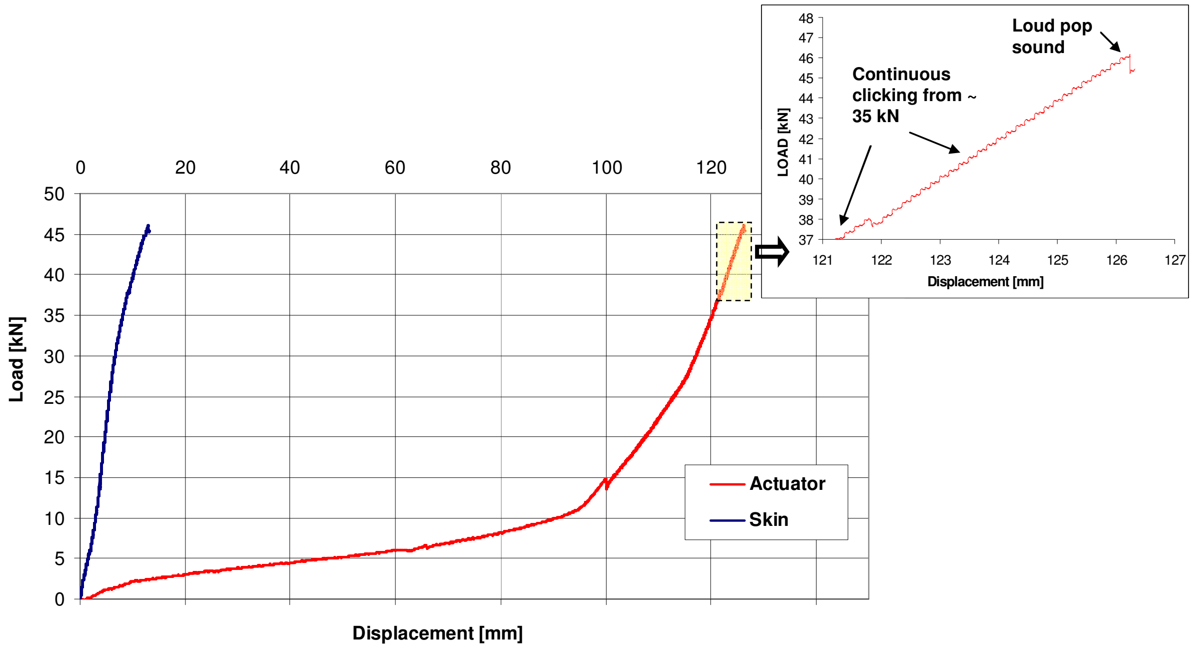

Figure 60. Load – displacement chart of the first load cycle

Figure 61 shows an identical chart with a skin displacement shift of 114 mm. The plot indicates that at an actuator displacement of 124 mm the bumper was fully closed and compressed. Thus, the displacement of the skin became aligned with the displacement of the actuator.

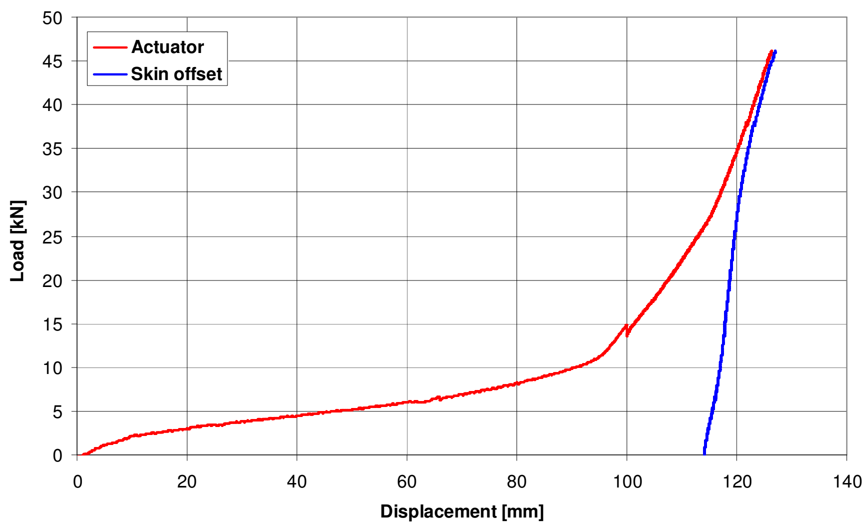

Figure 61. Offset load – displacement chart of the first load cycle

5.4.2 Load cycle 2

In the second load cycle, a number of cracking noises were observed from a load of 44 kN which was slightly above the final load level of the 1st loading cycle (prior to unloading). Between 48 kN and 52 kN minor load drops were recorded associated with four audible cracks. From approximately 54 kN the panel emitted a continuous cracking sound. At this loading, damage of the central shear ties at the frames 2, 3 and 4 was clearly visible. Shear ties ST2.3, ST3.3 and ST4.3 showed crushing and fibre breakage in the radius while these shear ties opened. The damage initiated in the centre and propagated relatively symmetrically along the length of the parts. To prevent a complete failure of the shear ties, the second loading was stopped after reaching a load of 57 kN which corresponded to 22 mm of skin displacement. The final stage of shear tie damage propagation is depicted in Figure 62. ST2.3 contained a crack of about 95 mm. The largest crack of 160 mm was observed in the central shear tie of the central frame (ST3.3) while the damage at the ST4.3 propagated to the final length of 145 mm.

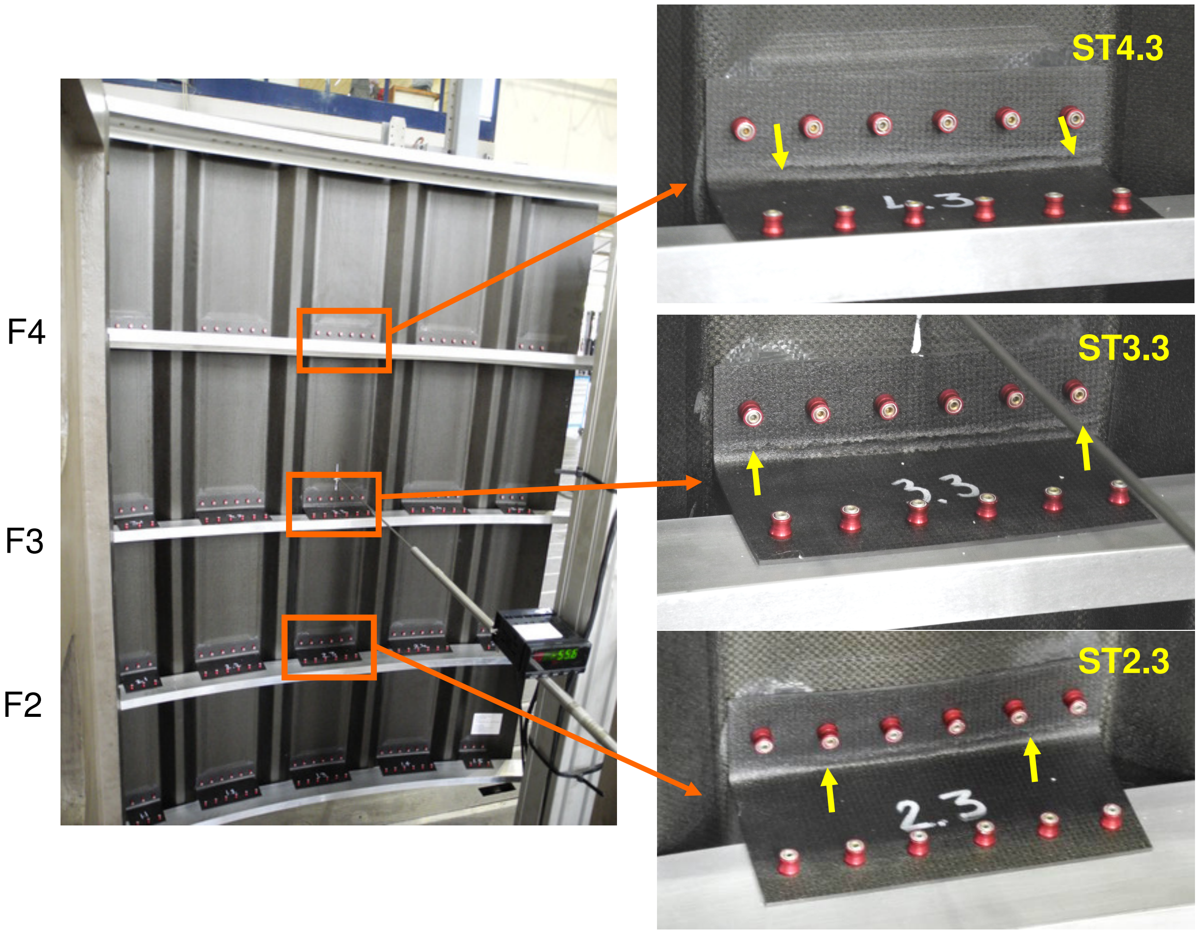

Figure 62 Cracked shear ties at maximum load

The load – displacement plot for the 2nd loading cycle is presented in Figure 63 which again shows a non-linear response with relatively low stiffness behaviour and minor skin displacement before bumper closure followed by a stiffer response after full compression of the impactor. Shear tie damage propagation resulted in several minor load drops. Furthermore, a reduction of the panel's stiffness was measured after exceeding a load of 47 kN.

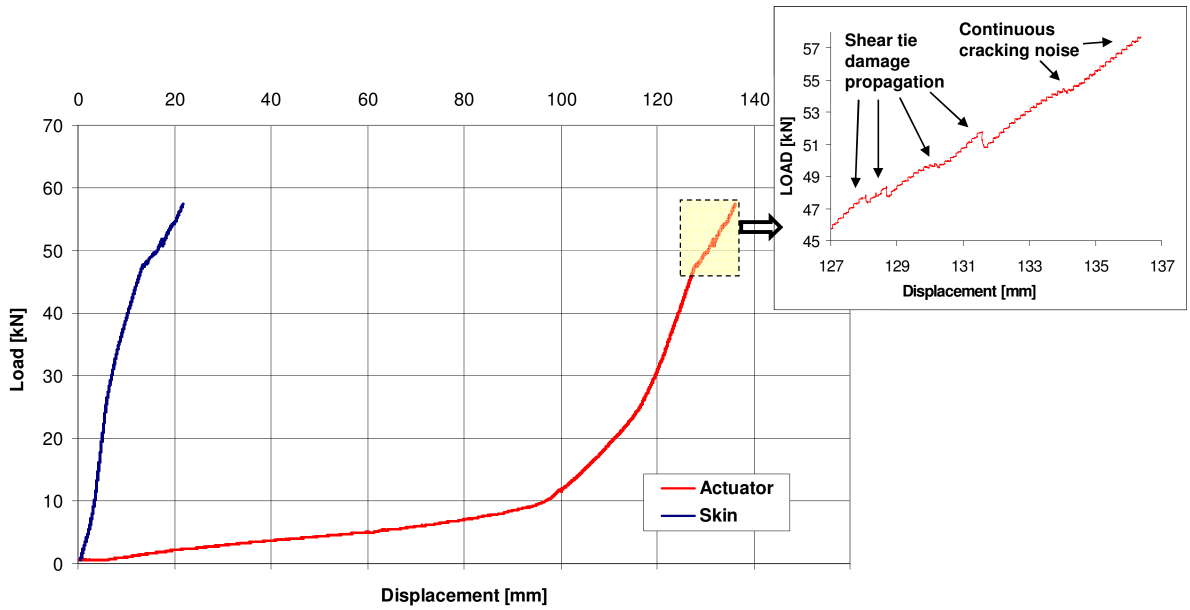

Figure 63 Load – displacement chart of the second load cycle

Similarly to the previous section, a load – displacement chart with a skin offset of 114 mm is shown in Figure 64. Based on the overlap of the curves, a full compression of the bumper occurred at an actuator displacement of 124 mm. After this point, the displacement of the actuator / bumper was equivalent to the LVDT measurements of the skin.

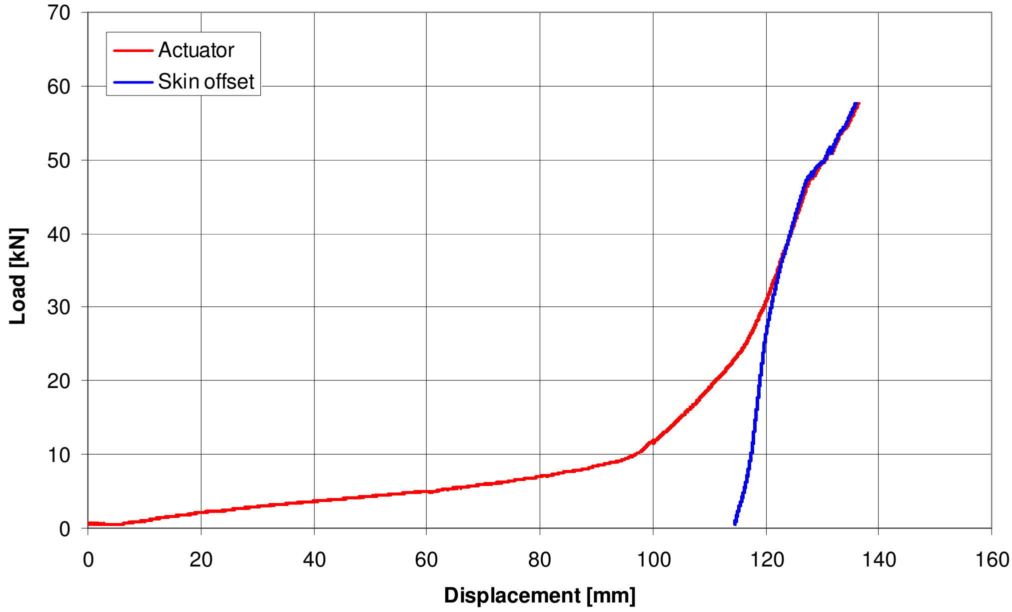

Figure 64. Offset load – displacement chart of the second load cycle

Even after developing significant fibre damage, once the panel was unloaded, the cracks in the radii of the three central shear ties were not visually detectable. The post-test visual inspection and the A-scan examination revealed no additional failures such as internal skin delamination or stringer debond. The flanges of the damaged shear ties were also inspected with no delamination reported.

5.4.3 Load cycle 3

An initial clear evidence of the re-opening of the existing cracks in the central shear ties was observed at around 14 kN. Visible delaminations / crushed fibres are shown in Figure 65. As the load increased, radius delaminations progressively opened. A continuous cracking noise was again audible from 44 kN, indicating further damage growth. The maximum damage propagation was observed in the ST 3.3 which was found to grow to almost the entire shear tie length at a load of 48 kN. The damage size is shown Figure 66 which additionally reveals a first evidence of a minor twisting of the Z-profile frame 3. The deformation of the frames resulted in additional bending and shear load transferred to the shear ties which caused a tilting of the webs.

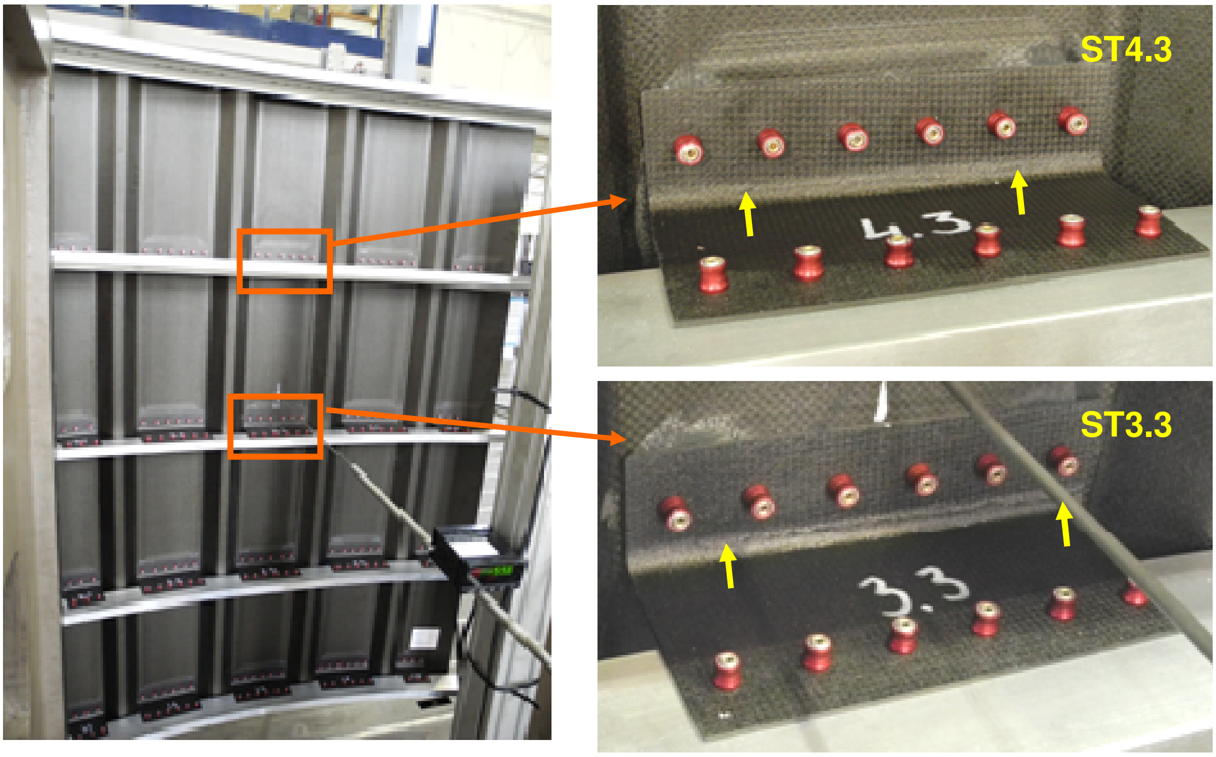

Figure 65. Shear ties delaminations visible at 14 kN

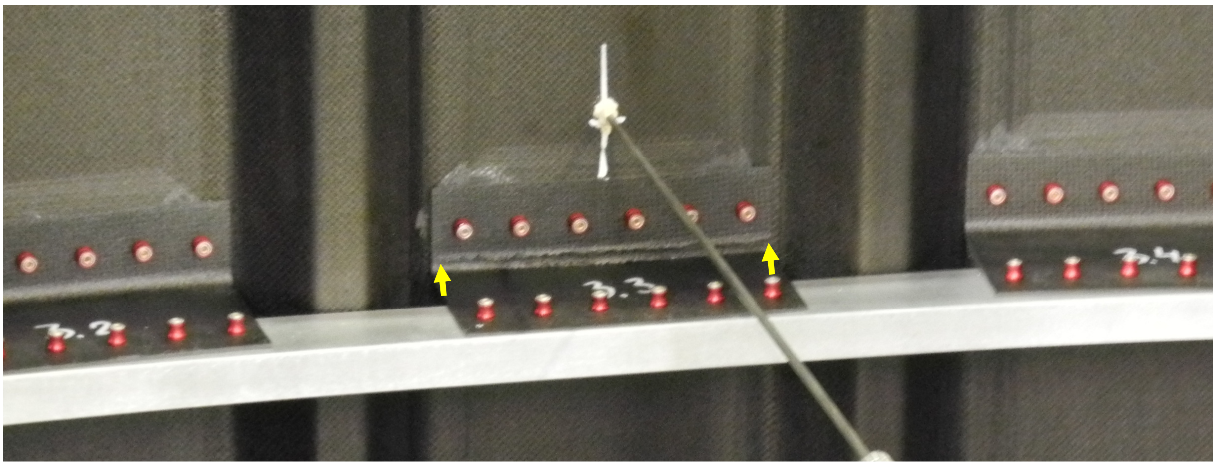

Figure 66. Shear tie ST3.3 crack at 48 kN

Once reaching 57 kN, two large popping noises were heard followed by further delamination propagation associated with a continuous clicking noise. Further crack and pop sounds were detected at 67 kN and 71 kN when a load drop of about 1 kN was recorded. The twisting of the frames and excessive bending deformation of the central shear ties became visually apparent as presented in Figure 67. Subsequently, while continuous clicks were being heard, the panel withheld a load of 75 kN when a large pop noise suggested further major shear tie damage propagation. This was also detected by a sudden 2 kN load drop. The load then increased to 76 kN when another minor load drop was measured.

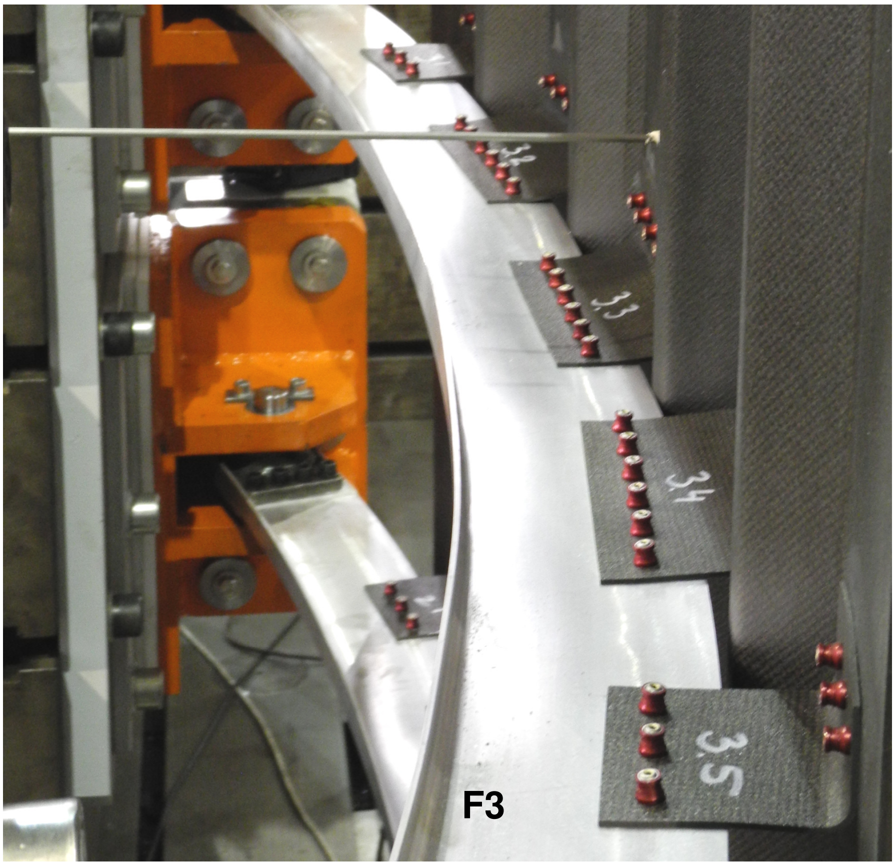

Figure 67. Deformation of frame 3 and the attached shear ties at 73 kN

At 77 kN, the clamped frames (F2, F3 and F4) showed significant profile twisting, predominantly at their centres. At this stage, all central shear tie radii delaminations (ST2.3, ST3.3, ST4.3) propagated along almost the entire length. The deformation of frame 4 is presented in Figure 68.

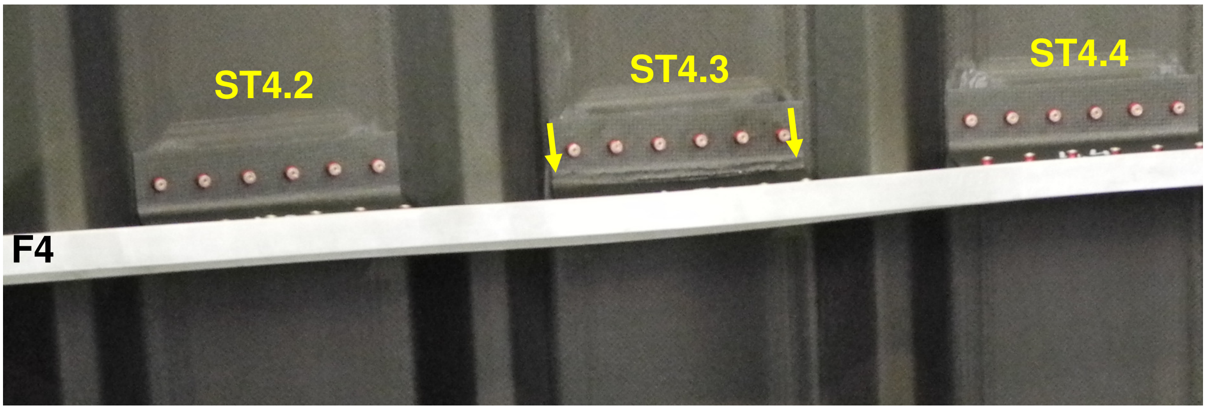

Figure 68. Shear tie damage and frame 4 deformation at 77 kN

The panel held up to a maximum load of 83 kN when a sudden collapse of several shear ties (ST2.3, ST3.2, ST3.3, ST4.2 and ST4.3) occurred. This was due to accumulation of damage in the shear ties radii and severe twisting of the frames which cause closing of the shear ties angles. Fracture of the five shear ties resulted in a large load drop to 47 kN at which point the test was stopped. As a consequence of the shear ties' collapse, the frames 2, 3 and 4 became in a contact with the caps of the stringers 2 and 3 causing some surface damage / first ply fibre crushing of the stringers. An overall view of the final frame deformation and the fractured shear ties is provided in Figure 69.

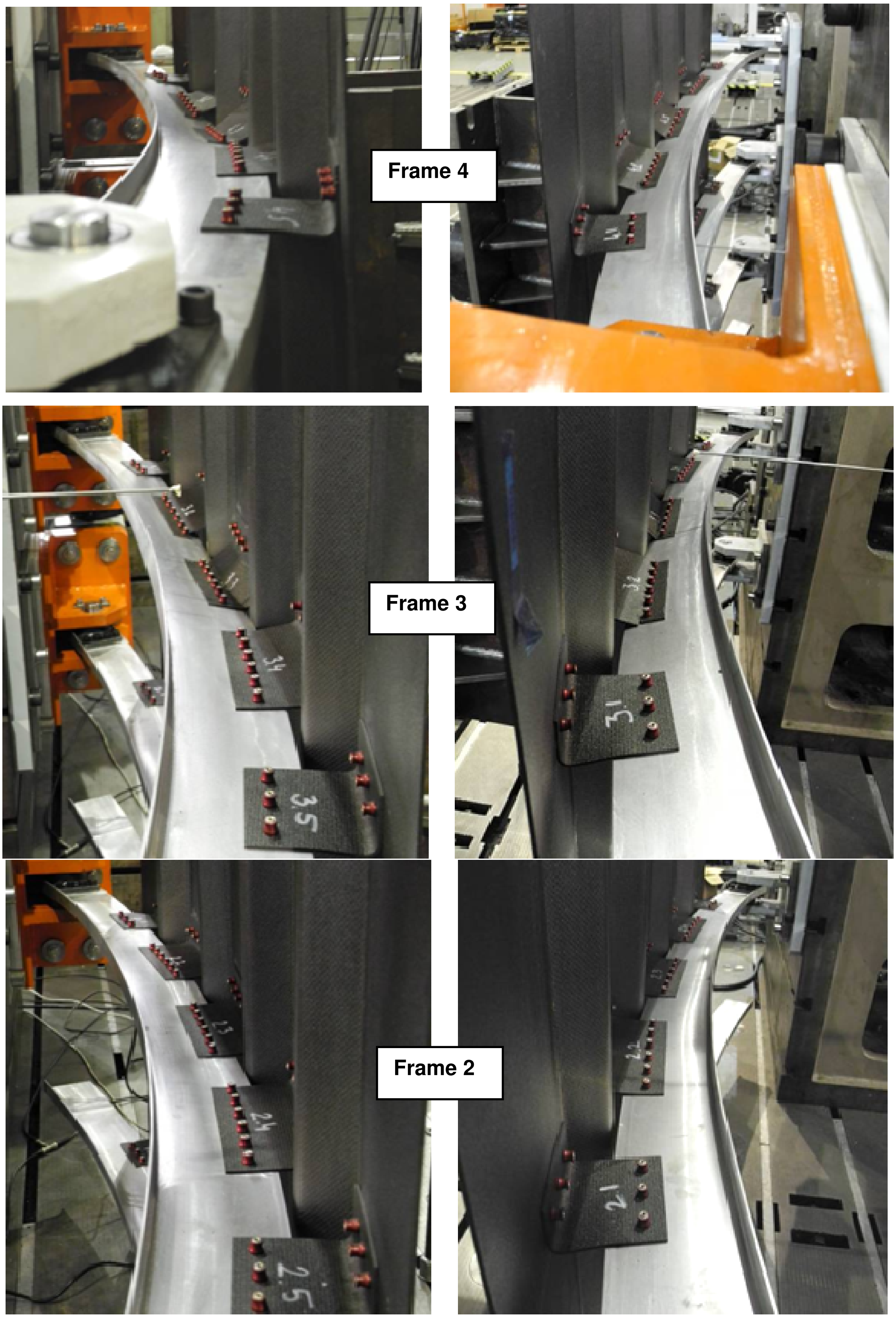

Figure 69 Final deformation of the frames 4,3,2 and attached shear ties at the maximum load

The failed shear ties and frame-stringer contact positions are provided in detail in Figure 70 to Figure 72. The central shear ties 4.3 and 3.3 failed at two locations. First fracture location was found to be at the radii due to accumulated damage (fibre breakage / crushing), the second fracture occurred along the frame rivet line. This is believed to be caused by the excessive twisting of the frames. The shear ties 4.2 and 3.2 failed at the frame rivet line only while the ST2.3 failed due to a delamination growth and fibre crushing along the radius.

Three contact locations between the frames and stringers, shown in Figure 70 and Figure 71, were observed. Although not a major failure mode, the most significant surface damage was found to be caused by frame 3 at stringer S2. Fibre crushing / breakage can be seen by a small amount of debris on the frame web.

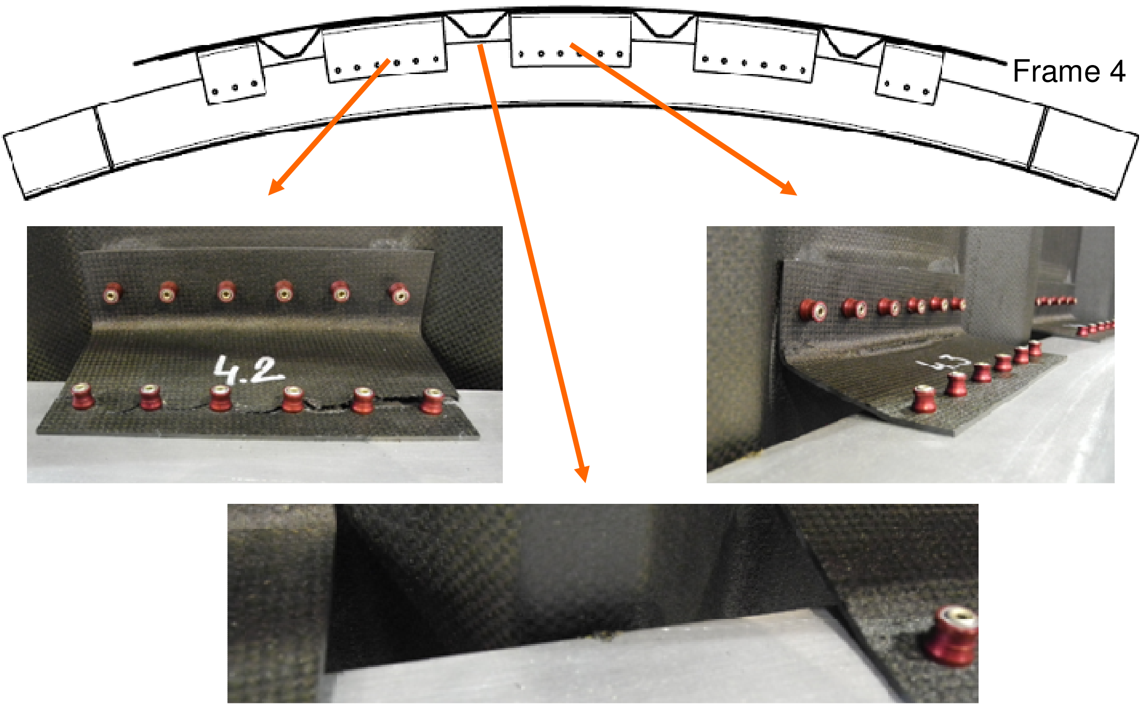

Figure 70. Detailed failure modes at the frame 4

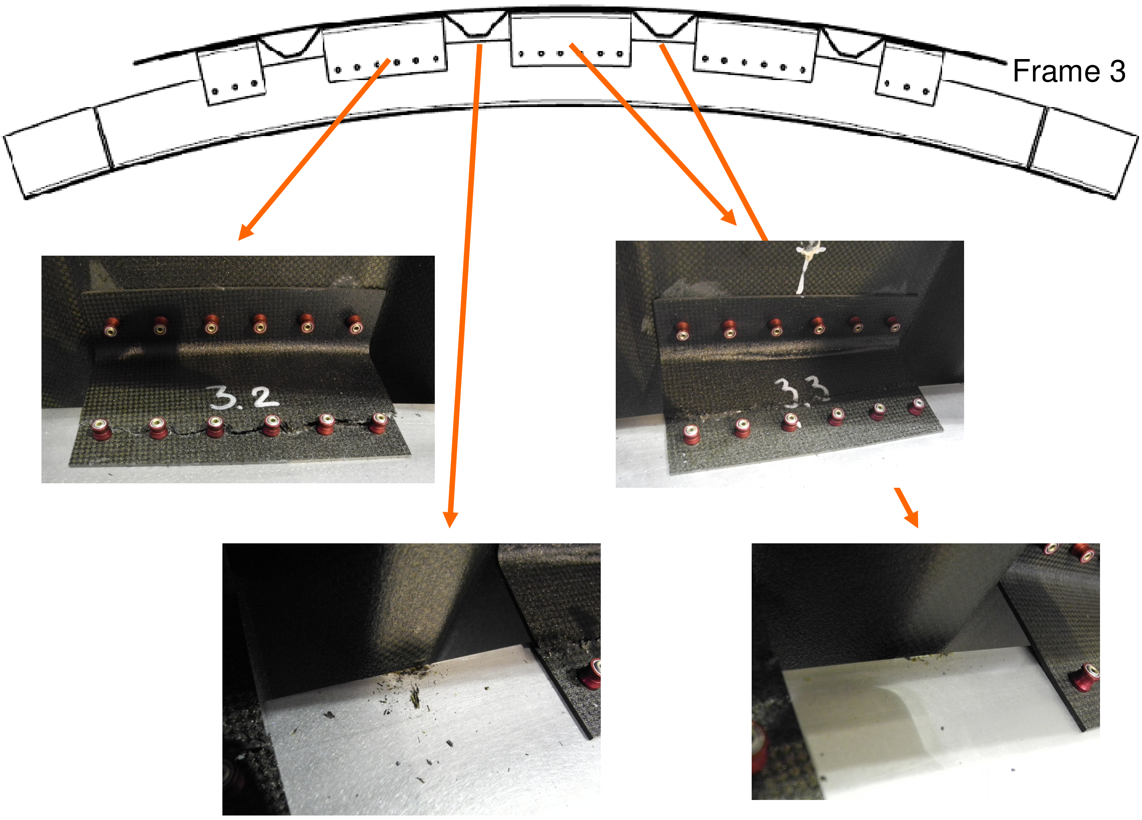

Figure 71. Detailed failure modes at the frame 3

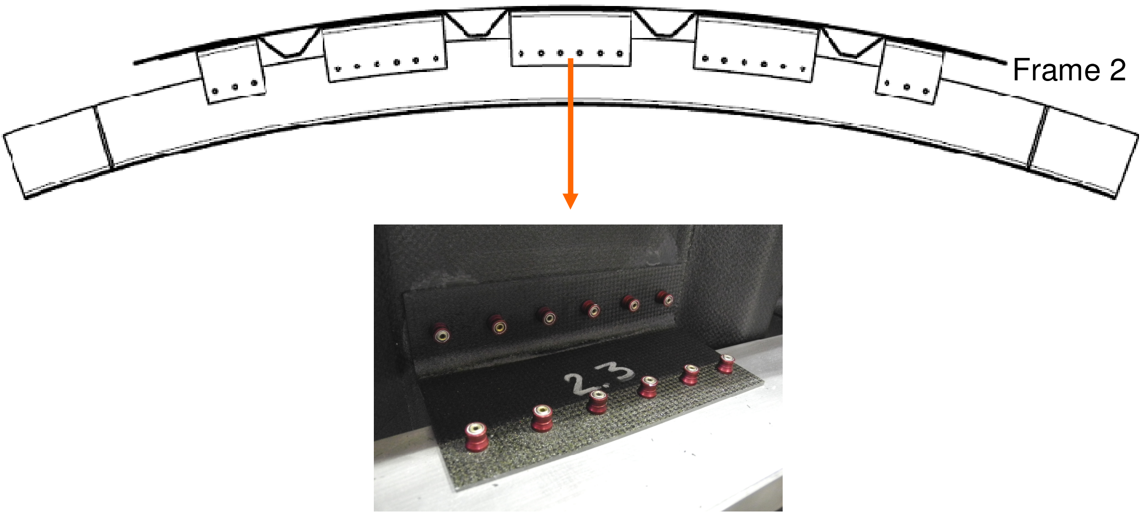

Figure 72. Detailed failure modes at the frame 2

The load – displacement curve for the 3rd loading is provided in Figure 73. The load increased almost linearly up to 100 mm actuator displacement when divergence from the linear behaviour and a stiffness increase was observed. Delamination growth in the shear ties resulted in a slight reduction of the stiffness of the panel prior to the final failure. Similar to the first two loading cycles, the offset load – displacement plot in Figure 74 indicates that the rubber bumper reached a state of full compression at a displacement of 124 mm. After this point, displacement of the bumper and skin was identical.

The visual inspection and the A-scan examination, performed after the third loading, again revealed no additional internal non-visible damage. After unloading, the panel returned to its original shape without evidence of any permanent deformation. Although severely distorted during loading, the frames showed no apparent plastic deformation.

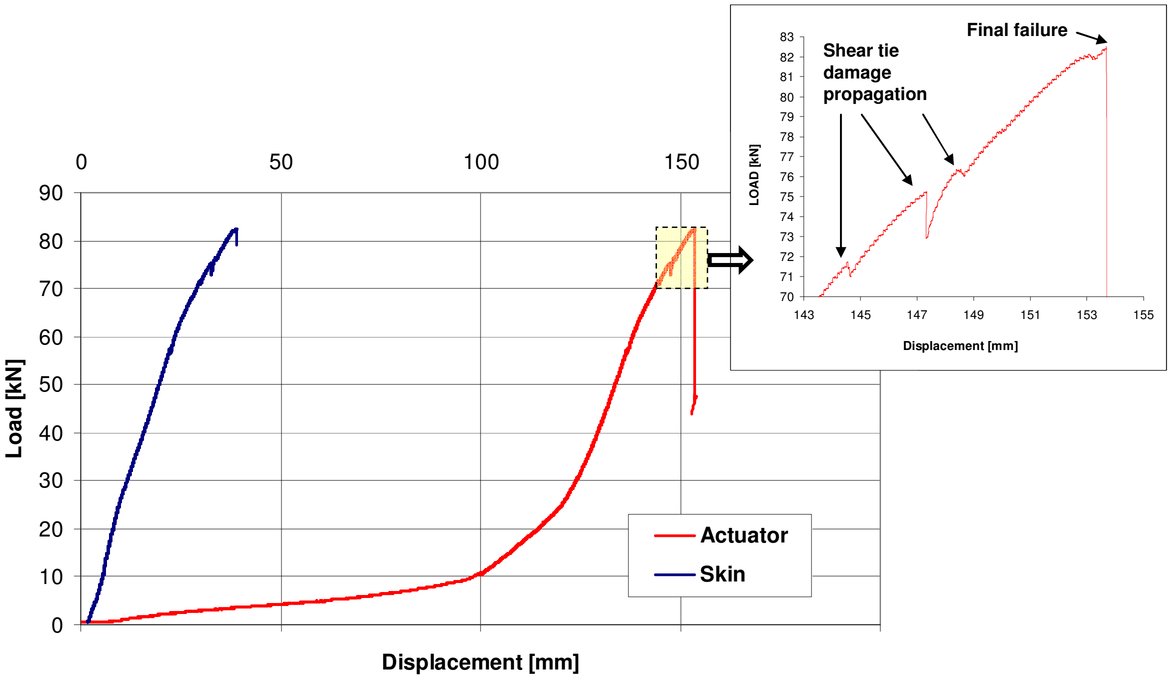

Figure 73. Load-displacement chart of the third load cycle

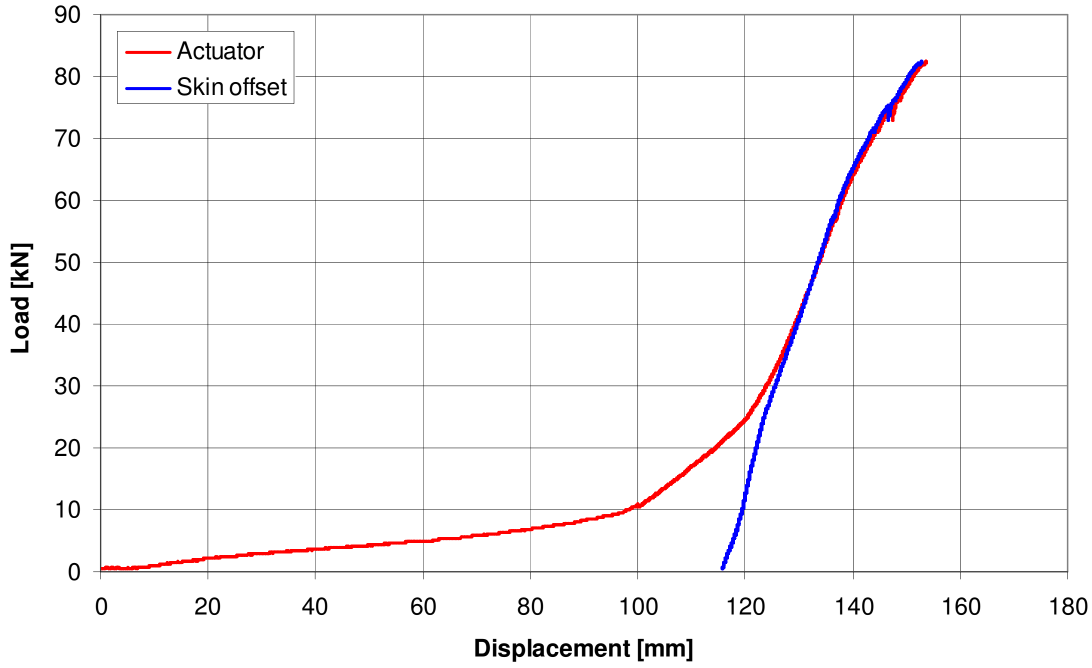

Figure 74. Offset load – displacement chart of the third load cycle

6 Discussion of the results

A summary of the failure sequence is provided in Figure 75. Failure initiated in the radius of shear tie 3.3. As the load was increased, widespread delaminations formed in several shear ties. A severe loss of stiffness was caused by accumulated damage and a sudden fracture of five shear ties. Consequently, increased skin deformation caused localised contact between the stringers and the considerably twisted aluminium Z-profile frames. This resulted in minor fibre damage and surface scores at the stringer caps.

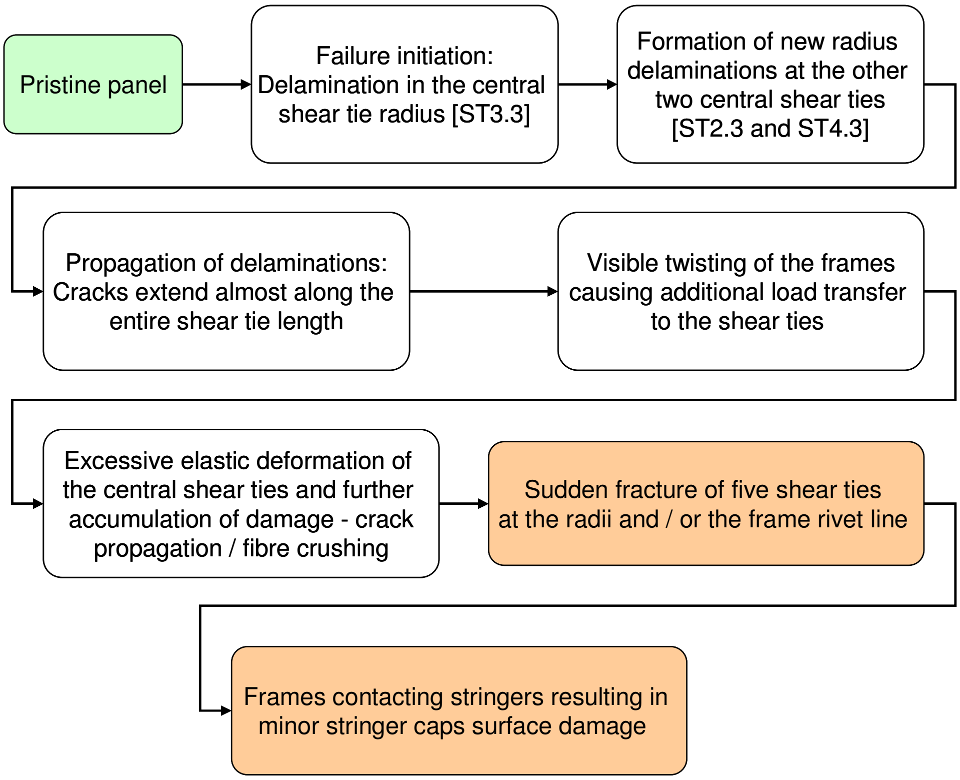

Figure 75. Damage sequence summary

As mentioned in the previous chapter, an A-scan examination was performed after each load cycle. The inspection was conducted according to the scanning pattern shown in Table 6. The non-destructive examination did not identify any internal damage such as skin delamination or skin-to-stiffener debond. The rivet hole rows and adjacent skin regions at the impact area were carefully scanned using a smaller ultrasonic probe. The inspections revealed no cracking or internal delaminations around the rivets.

Table 6. NDI scanning pattern

	Inspected areas on the outer skin side
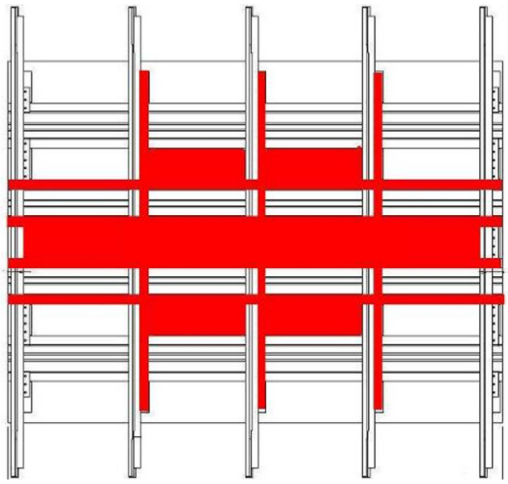	Central skin bays (stringers 2 / 3, frames 2 - 4) Feet of central stringers (2 & 3) Shear tie foot regions (frames 2 to 4) Rivet holes and surrounds at the impacted area

Visual inspection of the panel's outer skin surface showed no evident scratches or cracks which would indicate that the structure was impacted by a blunt impactor. Surface appearance of the outer skin (shiny tool side) due to the contact with the rubber bumper did not change. There was no evidence of any rubber residue or other rubber-like marks. The outer skin after testing is shown in Figure 76. A lack of any evidence of impact on the outer skin side supports general concerns that composite aircraft structures may pose risks associated with wrong assumptions regarding the criticality or extent of damage after a high energy blunt impact.

Figure 76 additionally highlights the load application region on the panel. The width of the bumper that contacted the skin was measured as 195 mm which gives the total compression area of 195000 mm^2 (the bumper was 1000 mm long).

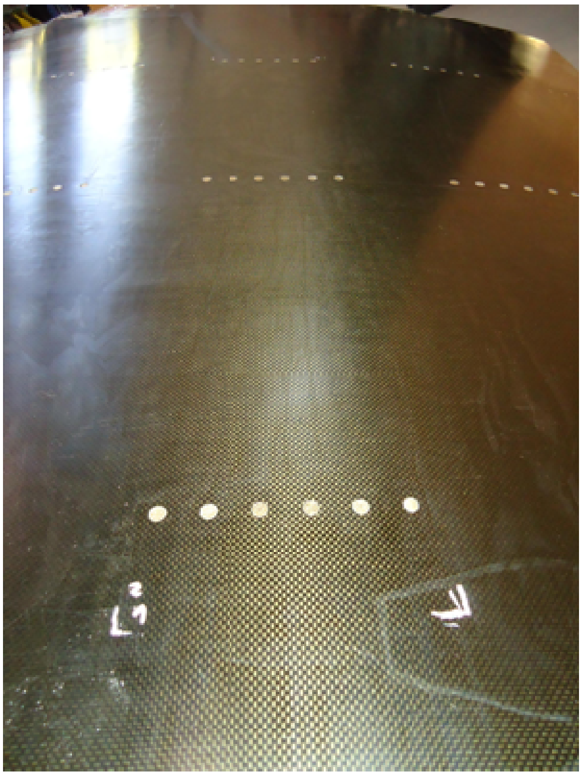
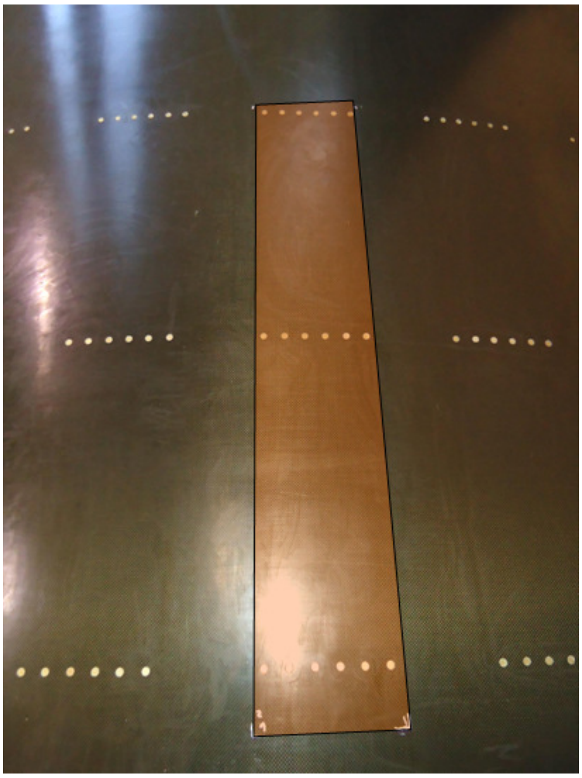

Figure 76. Outer skin surface after testing showing the load application region

A comparison of the load-displacement charts of the three load cycles is provided in Figure 77. During compression of the cylindrical rubber impactor, three significant events were observed. At an actuator displacement of 90 mm, the bumper's inner attachment plate and bolts contacted the opposite inner surface. This point is referred to as the *first contact* at which an initial indication of the non-linear increase of stiffness was measured.

While at the first contact point the bumper was significantly compressed, the resulting skin displacement was only 2.9 mm during the 1st load cycle. Due to the accumulated damage in the subsequent load cycles, the panel's behaviour was more compliant. The skin displacement in load cycle 2 and 3 at the first contact was 3.0 and 4.9 mm respectively. The area under the load – displacement curve assists in determining the energy required to compress the impactor which was calculated as 445 J for the 1st loading while during the last load cycle 359 J was absorbed.

The second significant point on the P-u chart is at an actuator displacement of 110 mm and is referred to as the *visual bumper closure*. At this point the bumper appeared to be fully flattened. Similarly to the first contact point, the corresponding load decreased in subsequent load cycles.

As already discussed, the last noteworthy point was at 124 mm when the displacement of the actuator and LVDT became aligned. Thus the bumper was fully compressed at this load and, in theory; a movement of a ground service vehicle beyond this point would be directly translated into skin deformation. This point in the P-u chart is referred to as the *full compression of the bumper*.

As expected, damage growth caused softening of the panel's behaviour with each load cycle. From the obtained result, it can be concluded that the energy threshold for failure initiation was 1269 J. A sudden fracture of multiple shear ties, which occurred at the end of the 3rd loading, required an energy of 2660 J. This energy level, however, represents the failure energy of a pre-damaged structure. Thus, in reality, it can be anticipated that a pristine panel would require a higher energy level to produce such extensive failure.

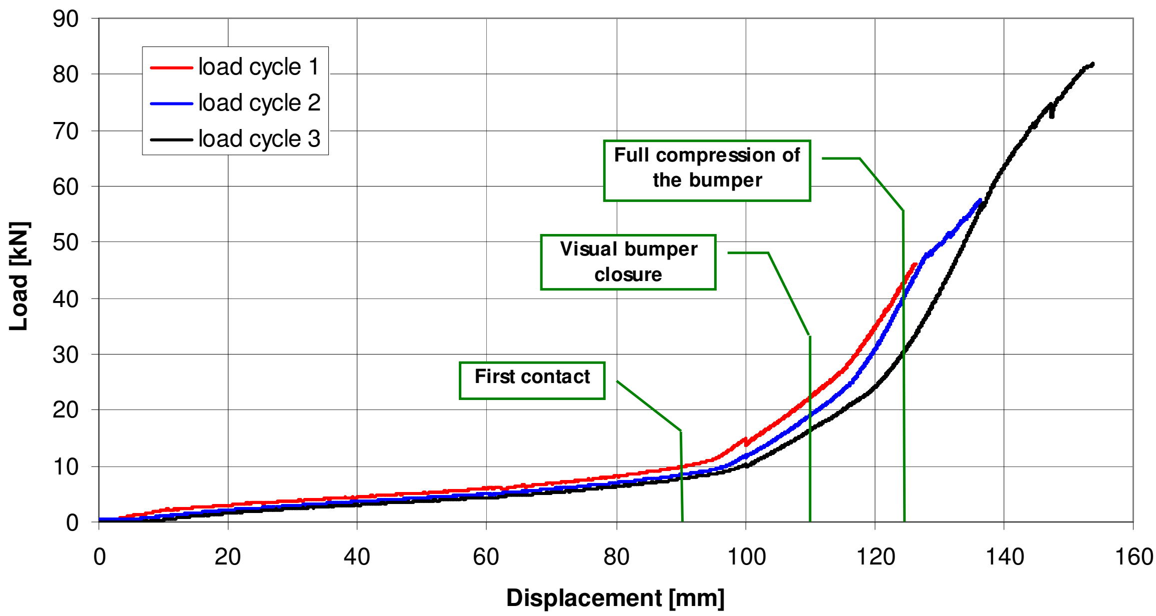

Figure 77 Load-displacement charts of the actuator in all three load cycles

A summary of the energy levels for each loading is provided in Table 7. Note that these energy levels are normalised by the bumper length. During the actual airport ground operation, the damage initiation threshold of 1269 J can be approximately reached by an impact of a ground service vehicle with a 1 m long cylindrical bumper and a mass of 2500 kg at 1 m/s. A comparable energy level would also be reached by a larger 5500 kg vehicle with an identical bumper size impacting a fuselage at 0.67 m/s. The energy level thresholds from the test data were in a very good agreement with the predicted realistic energy level boundaries discussed in Section 2.2.3.

Table 7. Summary of energy levels

Load cycle	Energy levels at First contact at 90 mm [J]	Visual closure at 110 mm [J]	Full compression at 124 mm [J]	Total energy [J]
1	445	741	1171	1269
2	364	612	991	1601
3	359	588	903	2660

The results from the numerical simulations correlated well with the actual skin displacement. A comparison of the test data and the FEA results is shown in Figure 78. Developed numerical models exhibited a reasonably linear stiffness which was also recorded during the first load cycle after the bumper closure and prior to stiffness degradation due to damage initiation. Since no degradation material models and failure criteria were implemented in the FE models, the accuracy of the FE models was limited to approximately 30 kN when the test panel's behaviour became non-linear due to damage growth.

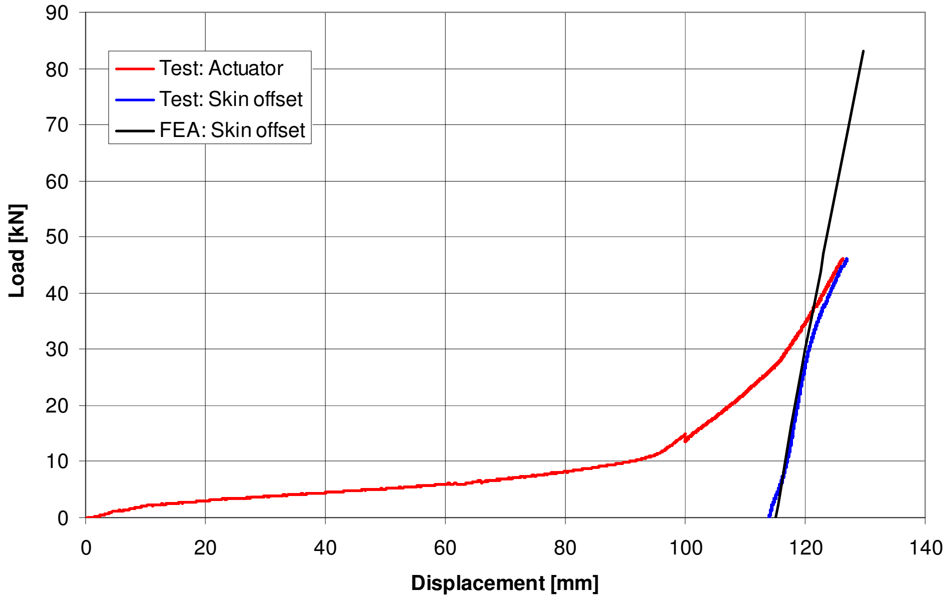

Figure 78 Load-displacement charts of test actuator and skin and of FEA skin displacement

7 Conclusion

High energy low velocity blunt impacts occur during aircraft ground operations and are typically caused by inappropriate contact of a service vehicle with the fuselage. Such events are typically very obvious to the ground crew (i.e. loud, involve severe jolt or unexpected aircraft movement, etc.) and therefore, should be immediately reported. However, if not reported, high energy low velocity blunt impact can initiate significant internal damage that may not be detected by visual inspection of external surfaces. Thus, it is important to demonstrate that a material change from metallic to advanced composite structures does not reduce the level of safety. Consequently, maintenance and operational procedures for composite fuselages must be adapted to maximise the opportunity to detect that such an event has occurred.

A comprehensive review summarising the ground operations incidents showed that the most frequent vehicles that caused damage of fuselages were cargo loaders and mobile stairs. Approximately half of the ground incidents resulted in damage of door surrounds while the remaining half resulted in damage of other parts of the aircraft (wing, empennage or engine).

Realistic impact energy levels expected in these incidents were established based on typical operational velocities of ground service vehicles while manoeuvring for ground handling operations and a representative weight of the vehicles. Considering an incident scenario involving a 2000 kg vehicle at 0.3 m/s (lower limit) and an impact of a 5000 kg vehicle at 1.2 m/s (upper limit) yielded an energy level range between 90 J and 3600 J. Further review of the actual incident data and previous test results supported the determination of reasonable failure energy threshold boundaries for high energy blunt impact which was estimated in a range between 1000 J to 3000 J. These failure threshold levels are above the energy levels considered typical of such impact events in design, i.e. e.g. thresholds up to 240J as considered in CMH-17 Rev.G (Draft) Vol. 3 Chapter 12. However, as indicated in this report, higher energy events do occur in service, thus emphasizing the importance of reporting such events (AMC 20-29), 2010.

In order to develop a credible baseline design for the test article, a review of CS-25 fuselage design was conducted. The panel design selected for this project represented the best compromise in terms of the realistic representation of a typical CS-25 fuselage construction harmonised with the activities of UCSD and other industry research groups. The hybrid composite-metallic test article consisted of four composite stringers that were co-cured to the curved skin panel and five metallic frames. This represented an intermediate level in a test and analytical pyramid. It is recognised (as suggested in Chapter 8) that higher pyramid testing is required to capture more realistic boundary condition in conjunction with the appropriate damage mode work.

Numerical simulation conducted in this study clearly showed that an accurate representation of the global aircraft-level behaviour on the test panel's scale was crucial. Based on the FE results, spring-based test fixtures were developed which provided the required flexibility of the frame attachment points. The numerical models additionally indicated no plastic deformation of the metallic frames while composite damage initiation was predicted at the central shear ties and in the skin within the impacted area.

The test panel was subjected to three load cycles, progressively increasing the maximum impactor displacement. Initialization of the damage occurred at the radius of the central shear ties which was in agreement with the FE results. The failure initiation energy threshold was found to be 1270 J. With the subsequent load cycles, widespread delaminations formed in shear ties at frames 2, 3 and 4. The aluminium frames exhibited significant twisting at high load levels. Progressive damage accumulation consequently resulted in a sudden rupture of five shear ties followed by a severe loss of load carrying capacity of the panel. Fractures occurred along the shear tie rivet lines or in the radii. As a result of such extensive failure, the three inner frames contacted with the two central stringers and caused surface damage to the stringer caps.

A significant outcome of this study is related to the composite structure damage detection. Testing of the composite panel highlighted that high energy low velocity blunt impact can cause extensive internal structural damage with low detectability when performing inspection of the external surface. Visual examination and ultrasonic A-scan inspection failed to detect growing delaminations in the shear tie radii. The outer skin surface exhibited no visual signs of impact such as scratches or dents. Furthermore, the identification of the failure of the shear ties along the frame attachment rivet line was not practically possible from an external examination. Thus, understanding of the onset and propagation of damage in composite aircraft structures is vital in order to demonstrate that equivalent safety level is provided by composite materials in comparison to the metallic counterparts. Aircraft certification as well as operation and service policies must take into account the characteristics of composite materials.

8 Implications

An experimental program was conducted in order to simulate a high energy low velocity blunt impact of a rubber bumper on a representative composite fuselage panel. The following implications are made for subsequent investigations:

Test structure and test method

Whilst only one panel was tested; additional tests are suggested in order to further increase understanding of the damage criticality / damage modes. This shall be performed in conjunction with the existing experimental program of the UCSD to maintain commonality of test panels and test methods.

In a potential future research program, the structures should be larger and more complex than the panel investigated in this study. To increase the level of realism, a representative door cut-out, reinforcement regions and floor beams should be included to take into account structural design features found in current state-of-the-art composite hulls in the regions which are classified as damage prone areas. This new complexity would lead to a better representation of stiffness and realistic behaviour of composite fuselages under high energy blunt impact.

Additional data acquisition equipment may provide useful information regarding behaviour of the test panel, displacement of the fixtures and aid in an accurate determination of damage initiation and growth. In addition to the LVDT that measures radial skin displacement near the centre frame, further LVDTs might be used to record the displacement of a skin bay as well as displacement and rotation at the boundary attachment points. The response of the test fixtures can also be monitored by clip gauges. Strain measurement could be included to monitor local behaviour of the panel. Test data would also assist in validating the numerical models by correlation of the test results with FE predictions. Advanced measuring techniques such as non-contact strain measuring could also be considered. Using a 3D surface tracking system such as ARAMIS would enable a real time global or localised strain mapping. To summarise, the following measurements and data acquisition equipment can be considered for addition in the next test campaign:

- Monitoring of the boundary displacement (e.g. spring strain, attachment rotation)
- Measuring of the skin indentation at multiple positions using mechanical or contactless laser LVDTs
- Video recording in the panel's axial view direction
- Three-dimensional surface displacement measurement system such as ARAMIS (may be difficult to implement due to test layout)

- Strain measurement (strain gauges)
- Acoustic emission monitoring to detect onset of matrix cracking, fibre breakage or debonding

An important aspect of this study was the representation of realistic boundary conditions. This was achieved by development of an elastic support that accounted for the absent stiffness of the surrounding structure. The current program focused on one particular impact case. Due to the complex behaviour of composite structures under low velocity blunt impact, damage criticality as a function of the stiffness of the boundary conditions should be investigated. This can be performed experimentally by changing the stiffness of the test fixtures or numerically through FE simulations.

Furthermore, as highlighted in Section 2.2.2, the force of the impact from a ground service vehicle can result in a movement of the aircraft which subsequently can cause a secondary impact and damage of distant aircraft sections away from the impact site. Thus, the criticality of the secondary damage and significance of the stiffness of boundary conditions to probable aircraft movement due to impact must be also fully understood.

After the quasi-static test programs are completed, the subsequent testing should include realistic low velocity crash testing by a vehicle or sled-like structure. Such a dynamic test method would enhance representation of the real life scenario.

In context of the performed investigation, regarding high energy impact on composite/hybrid structures, an equivalent metallic structure may also be studied. This can be used in comparison to the composite/hybrid structure to assess if and when damage becomes externally visible, which amount of invisible damage or failure is invoved and in which order damage occurs.

Further numerical analysis

As with the harmonisation of the test panels and test methods with the research of UCSD, a close collaboration on the development of advanced numerical approaches for low velocity high energy blunt impact is advised. The role of an accurate numerical modelling is vital to reduce the number of tests required for a full understanding of the main parameters driving the criticality of damage caused by impact of a ground service vehicle.

Based on the results of this study, it is apparent that further development of the modelling techniques is required to achieve full capability in predicting damage mode sequences and damage size. The future FE models should include:

- Detailed modelling (e.g. shear ties with rounded radius, local mesh refinement)
- Advanced composite material cards with damage evolution and failure criteria
- Fastener failure model

The focus on detailed failure investigation can be accomplished by the detailed modelling of the critical regions and specifying damage models for composite parts. It should be noted that the development of accurate material cards and damage parameters for the FE model may require a number of coupon and fracture mechanics tests to determine basic in-plane and interlaminar properties.

9 Recommendations

The outcomes of this study clearly indicated an existing threat of drawing wrong conclusions regarding the criticality and extent of damage due to high energy blunt impact on composite aircraft hulls. In order to retain the level of safety equivalent to metallic aircraft structures, the following recommendations can be given.

Airworthiness Certification

While this work represents a first measure in complete understanding of safety concerns, several certification amendments to EASA CS-25 and AMC 20-29, if deemed appropriate, should be considered:

- Create inspection requirements after a high energy low velocity blunt impact to examine the inner hidden structure as well as distant aircraft sections away from the impact site.
- Different technologies for in situ structural health monitoring (SHM) are currently being developed and could be used in future aircraft. Built-in fibre-optical sensors, strain gauges or acoustic monitoring systems could be used to enable near-term damage detection. Such devices would potentially reduce financial impact related to costly inspection of the inner fuselage. Early damage detection would also increase safety (for instance when damage is detected as Category 2 rather than Category 3) and reduce associated repair cost.
- For improved probability of visual impact detection, a contact / damage indicating paint could be used on aircraft fuselages. As for SHM above, the problem with nuisance indications / 'no-fault-founds' will need to be addressed before such an approach can be convincing.
- Built-in accelerometers in aircraft hulls or ground service vehicles would allow detection and recording of any inadmissible contact or impact.
- Establish requirements regarding accessibility for inner inspection of the fuselage. Due to the reported difficulty in detection of structural damage from outside, a maximum accessibility of the internal structure is desirable. The requirement may include inspection rules to utilize the existing maintenance access doors or service panels in the aircraft fuselage which would enable access for NDT monitoring such as video endoscopic diagnostics.

Continued Airworthiness and Maintenance

- Adopt maintenance adjustments including optimised inspection techniques for BVID detection of composite structures according to the certification requirements discussed above. As described in Baaran (2009), visual detection of dents requires precise inspection procedures under reasonable conditions. Improved probability of early damage detection must be ensured for Category 3 damage. Such damage can be generated by high energy low velocity blunt impact and therefore the maintenance procedures must assure that it is identified by the ramp personnel within a few flight cycles.

- Establish specialised qualifications and training requirements for ground staff and maintenance personnel. Specific training for ground service staff is recommended to emphasize the differences in damage criticality and its visibility in composite fuselage structures compared to metallic hulls.
- Damage from other sources (apart from ground service equipment) must be considered. These include incidents occurring during aircraft movement in airfields or hangars as well as foreign object impact.

Operational

- Improve prevention of undue impact. A contact between ground service vehicles and the fuselage is mainly protected by passive safety devices (such as rubber bumpers). Although modern ground service vehicles feature several types of electronic safety systems like proximity sensors and automatic position adjustment, there are no safety regulations that would require these systems to be fitted in vehicles involved in aircraft ground operations. Standardisation of the safety systems is necessary to reduce the impact threat.
- Based on the proven differences in detecting damages between metallic and composite fuselages, the reporting processes should cover every inadmissible contact to evaluate all potential safety risks. Although the ground service personnel are trained to follow the “report every vehicle contact” policy, the incident reporting relies strongly on visual examination of the outer skin structure. Consequently, the rate of vehicle contact reporting is approximately 50% (Kaiser, 2011). Due to a lack of visually evident damage, this rate can even further reduce for composite hulls if vehicles are not equipped with modern active safety systems.
- Ground service vehicles which repeatedly make contact with the fuselage, such as mobile stairs and cargo loaders, might be fitted with monitoring and assistance systems that would provide better visibility and assessment of the vehicle’s movement within a specified distance from the fuselage. Recording of sensor and camera data might support the complete reporting of incidents and their investigation.

References

Airbus A320 single-aisle medium-range airliner, www.aerospace-technology.com, 2011

Airbus-A320-Familie, http://de.wikipedia.org/wiki/Airbus-A320-Familie, 2011

Airbus A330, http://de.wikipedia.org/wiki/Airbus_A330, 2011

Airbus A350, http://en.wikipedia.org/wiki/Airbus_A350, 2011

Airbus A350 XWB update, Reinforced plastics, www.reinforcedplastics.com, Nov/Dec 2010

Airbus A350 XWB – work packages Premium AEROTEC, www.premium-aerotec.com, 2011

Airbus A380, http://en.wikipedia.org/wiki/Airbus_A380, 2011

Airbus website, *Innovative materials*, www.airbus.com/innovation/proven-concepts/in-design/innovative-materials, 2011

Airliners website, *Boeing provide update on 787 program*, www.airliners.net, 2008

AMC 20-29, Composite Aircraft Structure, Annex II to ED Decision 2010/003/R of 19/07/2010, 2010

ARFF website, http://www.arff.info, 2006

Ashford, H.P., Stanton, M., Moore, C.A., *Aircraft operation*, second edition, 2002

Australian Transport Safety Bureau, *Ground operations occurrences at Australian airports 1998 to 2008*, Aviation Research & Analysis AR-2009-042, 2010a

Australian Transport Safety Bureau, *Level 5 Factual Investigations: July 2010 to September 2010,* ATSB Transport Safety Bulletin, Aviation Level 5 Investigations, AB-2010-061, 2010b

Aviation explorer website, *Airbus A350 XWB aircraft airliner history pictures and facts*, www.aviationexplorer.com, 2011

Baaran, J., *Visual inspection of composite structures*, Research project EASA.2007/3, 2009

Birtles, P., *Boeing 777: Jetliner for a new century*, MBI Publishing Company, 1998

Building to fly, Flight International, May 2003

Burchell, B., *Airbus A350XWB's high-tech promise*, www.aviationweek.com, 2009

Boeing 747, http://de.wikipedia.org/wiki/Boeing_747#747-400, 2011

Boeing 777, http://de.wikipedia.org/wiki/Boeing_777, 2011

Boeing 787 Dreamliner, http://en.wikipedia.org/wiki/Boeing_787, 2011

B787 door frames, www.klune.com/casestudies/b787_doorframes, 2011

Calawa, R. et al., *Automatic stringer drilling system*, SAE Aerofast Conference, Montreal, Canada, 1994

Cantwell, W.J., Morton, J., *The impact resistance of composite materials – a review*, Composites **22**(5): 347-362, 1991

Charles, M.M., *Report on the accident to Boeing 747-121 N739PA at Lockerbie, Report No: 2/1990*, The UK Air Accidents Investigation Branch (AAIB), Department for Transport, 1990

Composites World, *ATK delivers first composite parts for A350*, www.compositesworld.com, 2010

Cutler, J., *Understanding aircraft structures*, Blackwell Publishing, 2005

Gerzanics, M., *Bringing up a baby*, Flight International, June 2003

Govindasamy, S. *ANA knocks first 787 into boarding bridge*, www.flightglobal.com, Flightglobal, October 2011

Gower, M.R.L., Shaw, R.M., Sims, G.D., *Evaluation of the repeatability under static loading of a compression-after-impact test method proposed for ISO standardisation*, DEPC-MN 036, National Physical Laboratory, Middlesex, UK, 2005

Hamilton, S., *Sole-source tanker buy favors Boeing's KC-767*, www.leeham.net, 2007

Harrison, N., *Boeing 747*, Flight International, 12 December, 1968

International Air transport Association, *Ground damage prevention programme targets 10% cost reduction*, Industry Times, Edition 7, September, Article 4, 2005

Jormac Aerospace, *Tie-rod assemblies and attachments catalogue*, www.jormac.com, 2011

Kaiser, R., *Field experience with high energy wide area blunt impact damage*, 2011 FAA/EASA/Industry Composite Transport Fatigue, Damage Tolerance, Maintenance & Crashworthiness Workshop, Atlanta, GA, 17-19 May 2011

Key to Metals website, *Aluminum Alloy Development for the Airbus A380*, www.keytometals.com, 2011

Kim H, *Blunt impacts on composite stringer-stiffened fuselage structure*, Composite Materials Handbook 17 Meeting, Costa Mesa, CA, 21 July 2010

Kim H, *Safety management initiative on high energy blunt impact*, Composite Materials Handbook 17 PMC Forum, Kansas City, MO, 1 March 2011

Kim H, High energy blunt impact damage on composite aircraft structure, 2011 FAA/EASA/Industry Composite Transport Fatigue, Damage Tolerance, Maintenance & Crashworthiness Workshop, Atlanta, GA, 17-19 May 2011b

Kim H, DeFrancisci, G., Chen, Z.M., Rhymer, J., Tippmann, J., *Impacts damage formation on composite aircraft structures*, FAA Joint Advanced Materials & Structures (JAMS) 6th Annual Technical Review Meeting, Seattle, WA, 19-20 May 2010

Kingsley-Jones, M., *Speed limit*, Flight International, October 2003

Kingsley-Jones, M., *Airbus confirms switch to A380-style nose for A350 XWB*, www.flightglobal.com, 2007

Kumar, P., Rai, B., *Delaminations of barely visible impact damage in CFRP laminates*, Composite Structures **23**(4): 313-318, 1993

Leahy, J., *Taking the Lead: The A350 XWB*, taken from www.leeham.net, 2006

Lindeman, T., *Basic airframe of a passenger jet*, The Washington Post, April 17, 2006

Luchtzak website, www.luchtzak.be, 2006

McGowan, D.M., Ambur, D.R., *Compression response of a sandwich fuselage keel panel with and without damage*, NASA TM 110302: NASA Langley Research Center, Virginia, 1997

Meo, M., Vignjevic, R., Marengo, G., *The response of honeycomb sandwich panels under low-velocity impact loading*, International Journal of Mechanical Sciences **47**(9): 1301-1325, 2005

Mitrevski, T., Marshall, I.H., Thomson, R.S., *The influence of impactor shape on the damage to composite laminates*, Composite Structures **76**(1-2): 116-122, 2006

Niu, M., *Airframe structural design*, Conmilit Press Ltd., 1995

Norris, V.G., Wagner, M., *Airbus A380: Superjumbo of the 21st century*, Zenith Press, 2005

NMC-Wollard, *Ground support equipment*, www.nmc-wollard.com, 2011

Norris, G., *Creating a titan*, Flight International, June 2005

Ostrower, J., *Breaking: Structural flaw halts production of Alenia 787 sections*, www.freerepublic.com, 2009

Poon, C., Benak, T., Gould, R., *Assessment of impact damage in toughened resin composites*, Theoretical and Applied Fracture Mechanics **13**(2): 81-97, 1990

Pringle, T., *Preventing ramp and ground accidents*, Transport Canada, www.tc.gc.ca, 2010

Razi, H., Ward, S., *Principles for achieving damage tolerant primary composite aircraft structures*, 11th DoD/FAA/NASA Conference on Fibrous Composites in Structural Design, Forth Worth, Texas, USA, 1996

Roberts, T., *Rapid growth forecast for carbon fibre market*, Reinforced Plastics, February 2007

Roskam, J., *Airplane Design - Part III: Layout design of cockpit, fuselage, wing and empennage: Cutaways and Inboard Profiles*, DAR Corporation, 2002

RTT News, *Boeing's 787 Dreamliner takes off on maiden test flight*, www.rttnews.com, 2009

Seo, H., *Boeing 747*, Littlehampton Book Services Ltd, 1984

Smith, B., *The Boeing 777*, Advanced Materials & Processes, September 2003

The Boeing 737 technical site, *Detailed technical data*, www.b737.org.uk, 2010

Tomblin, J., Lacy, T., Smith, B., Hoopes, S., Vizzini, A., Lee, S., *Review on damage tolerance for composite sandwich airframe structures.* DOT/FAA/AR-99/49: Federal Aviation Administration, Office of Aviation Research, Washington DC, 1999

TUG Technologies, *GSE products*, www.tugtech.com, 2011

Waite, S., Damage/Defect types and inspection - some regulatory concerns, MIL-17 Damage Tolerance and Maintenance Workshop, Chicago, July 2006

Warwick, G., *A320: fly-by-wire airliner*, Flight International, August 1986

Wide-body aircraft, http://en.wikipedia.org/wiki/Wide-body_aircraft, 2011

Appendix A: Assembly chart and engineering drawings of the test panel

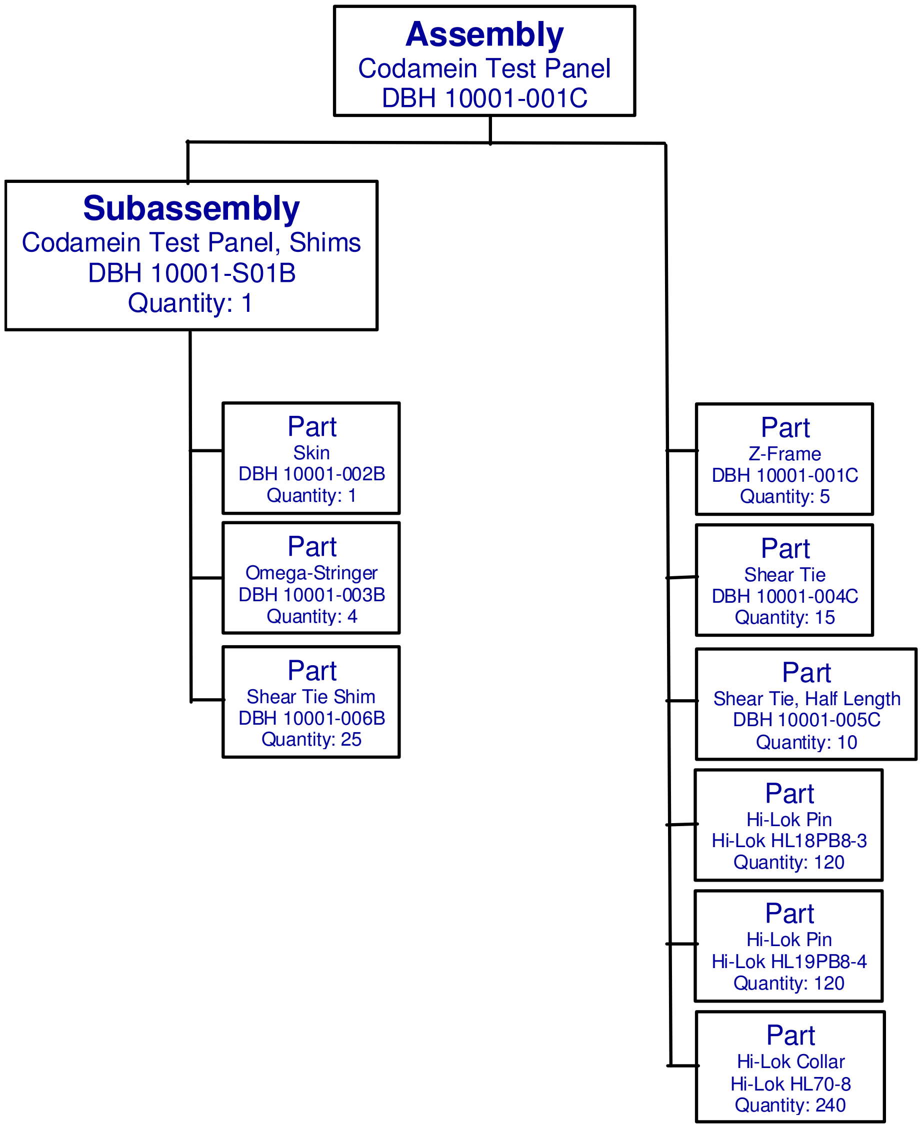

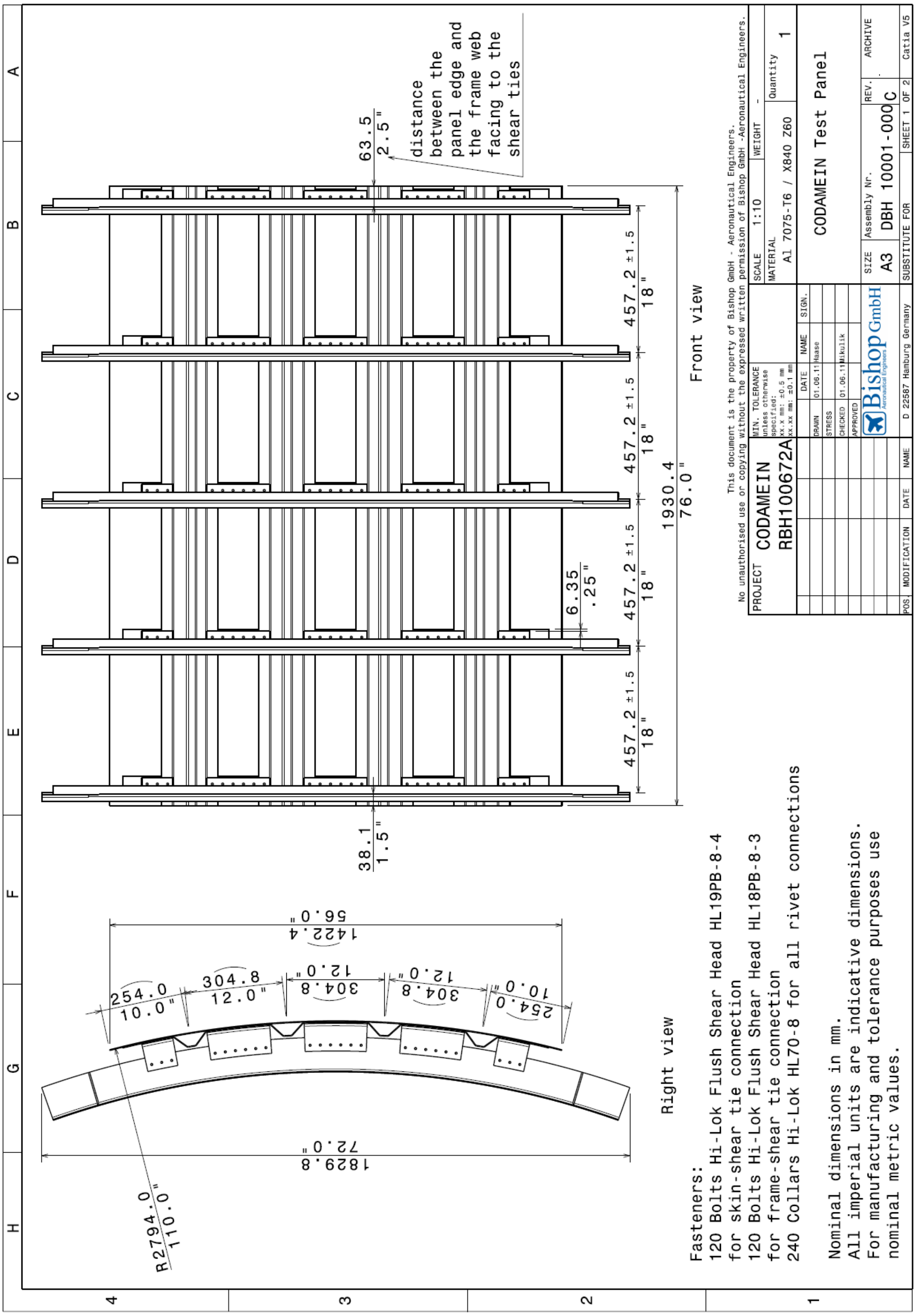
63.5
2.5"
distance between the panel edge and the frame web facing to the shear ties
457.2 ±1.5
18"
1930.4
76.0"
6.35
.25"
38.1
1.5"
Front view
1422.4
56.0"
254.0
10.0"
304.8
12.0"
1829.8
72.0"
R2794.0
110.0"
Right view
Fasteners:
120 Bolts Hi-Lok Flush Shear Head HL19PB-8-4
for skin-shear tie connection
120 Bolts Hi-Lok Flush Shear Head HL18PB-8-3
for frame-shear tie connection
240 Collars Hi-Lok HL70-8 for all rivet connections
Nominal dimensions in mm.
All imperial units are indicative dimensions.
For manufacturing and tolerance purposes use
nominal metric values.
This document is the property of Bishop GmbH - Aeronautical Engineers.
No unauthorised use or copying without the expressed written permission of Bishop GmbH -Aeronautical Engineers.
PROJECT
CODAMEIN
RBH100672A
MIN. TOLERANCE
unless otherwise specified:
xx.x mm: ±0.5 mm
xx.xx mm: ±0.1 mm
SCALE
1:10
WEIGHT
-
MATERIAL
Al 7075-T6 / X840 Z60
Quantity
1
CODAMEIN Test Panel
DATE
NAME
SIGN.
DRAWN
01.06.11
Haase
STRESS
CHECKED
01.06.11
Mikulik
APPROVED
SIZE
A3
Assembly Nr.
DBH 10001-000
REV.
C
ARCHIVE
POS.
MODIFICATION
DATE
NAME
D 22587 Hamburg Germany
SUBSTITUTE FOR
SHEET 1 OF 2
Catia V5

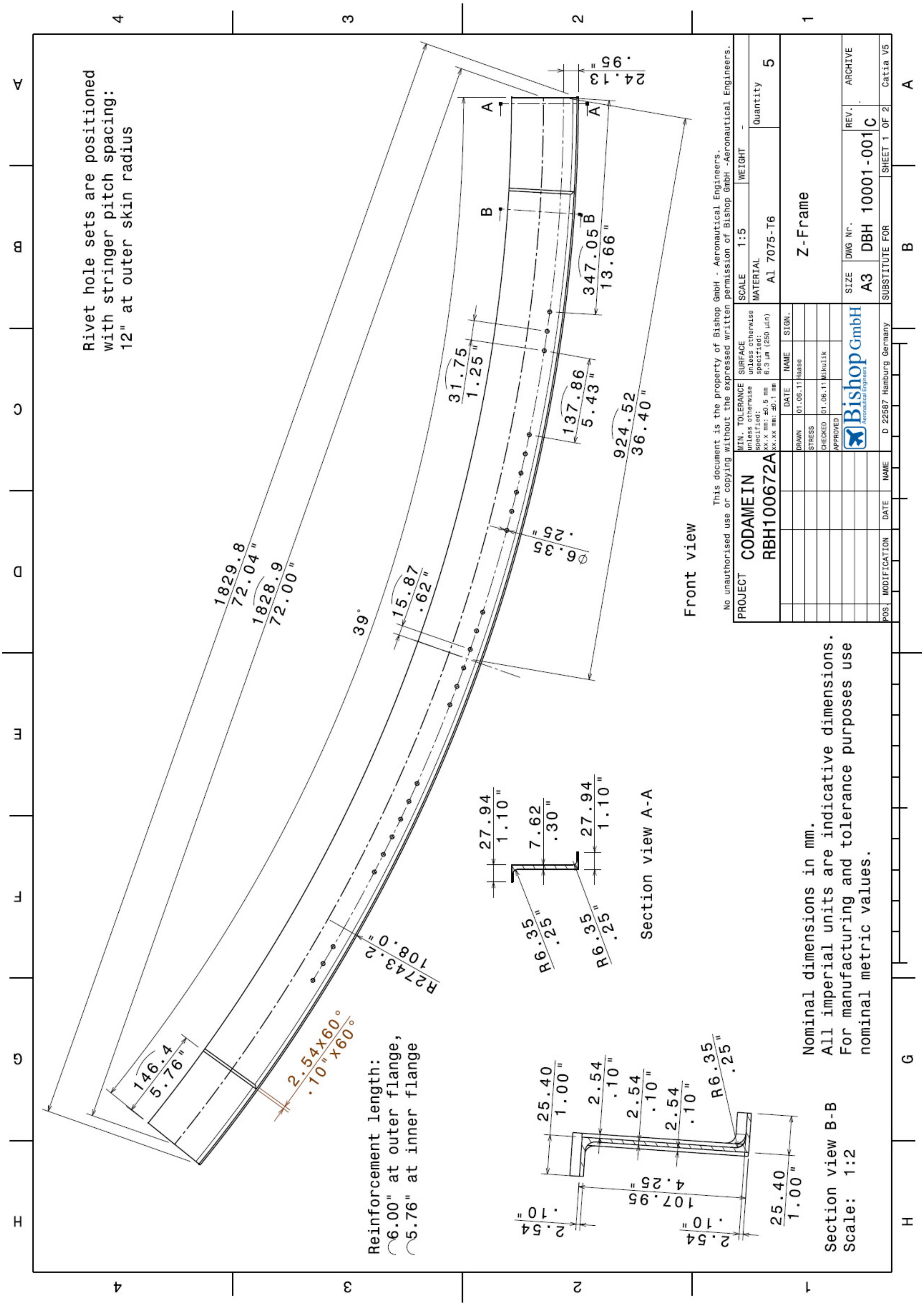

Rivet hole sets are positioned with stringer pitch spacing: 12" at outer skin radius
Front view
Section view A-A
Section view B-B Scale: 1:2
Reinforcement length: ⌒6.00" at outer flange, ⌒5.76" at inner flange
Nominal dimensions in mm. All imperial units are indicative dimensions. For manufacturing and tolerance purposes use nominal metric values.
1829.8 72.04"
1828.9 72.00"
39°
R2743.2 108.0"
924.52 36.40"
347.05 13.66"
137.86 5.43"
31.75 1.25"
15.87 .62"
24.13 .95"
146.4 5.76"
2.54x60° .10"x60°
⌀6.35 .25"
27.94 1.10"
7.62 .30"
R6.35 .25"
25.40 1.00"
2.54 .10"
107.95 4.25"
This document is the property of Bishop GmbH - Aeronautical Engineers. No unauthorised use or copying without the expressed written permission of Bishop GmbH -Aeronautical Engineers.
PROJECT CODAMEIN RBH100672A
SCALE 1:5
WEIGHT -
MATERIAL Al 7075-T6
Quantity 5
Z-Frame
DRAWN 01.06.11 Haase
CHECKED 01.06.11 Mikulik
SIZE A3
DWG Nr. DBH 10001-001
REV. C
SHEET 1 OF 2
Catia V5
D 22587 Hamburg Germany

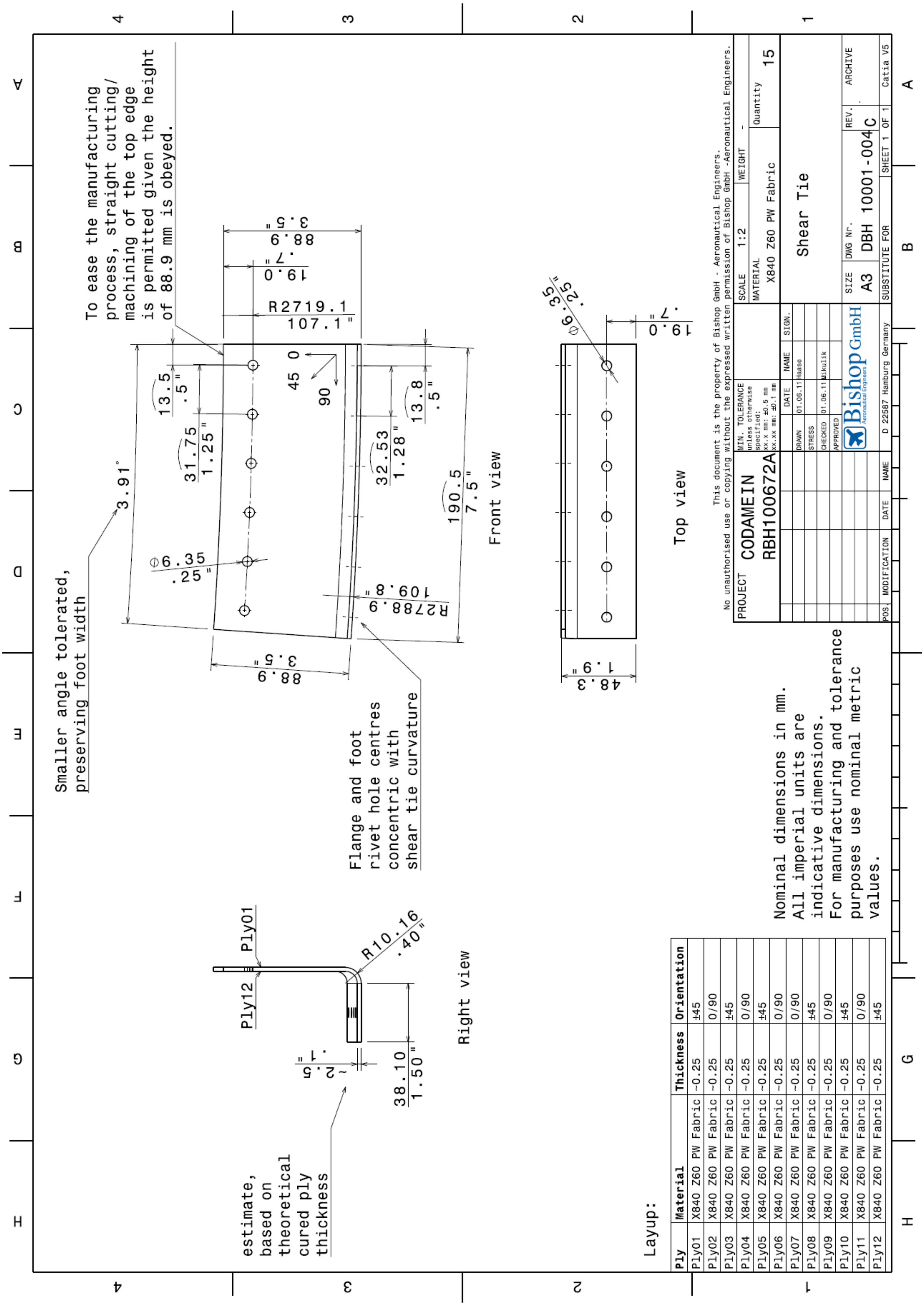

Ply	Material	Thickness	Orientation
Ply01	X840 Z60 PW Fabric	~0.25	±45
Ply02	X840 Z60 PW Fabric	~0.25	0/90
Ply03	X840 Z60 PW Fabric	~0.25	±45
Ply04	X840 Z60 PW Fabric	~0.25	0/90
Ply05	X840 Z60 PW Fabric	~0.25	±45
Ply06	X840 Z60 PW Fabric	~0.25	0/90
Ply07	X840 Z60 PW Fabric	~0.25	0/90
Ply08	X840 Z60 PW Fabric	~0.25	±45
Ply09	X840 Z60 PW Fabric	~0.25	0/90
Ply10	X840 Z60 PW Fabric	~0.25	±45
Ply11	X840 Z60 PW Fabric	~0.25	0/90
Ply12	X840 Z60 PW Fabric	~0.25	±45

Smaller angle tolerated, preserving foot width

To ease the manufacturing process, straight cutting/ machining of the top edge is permitted given the height of 88.9 mm is obeyed.

estimate, based on theoretical cured ply thickness

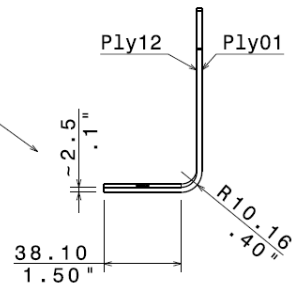

Right view

Flange and foot rivet hole centres concentric with shear tie curvature

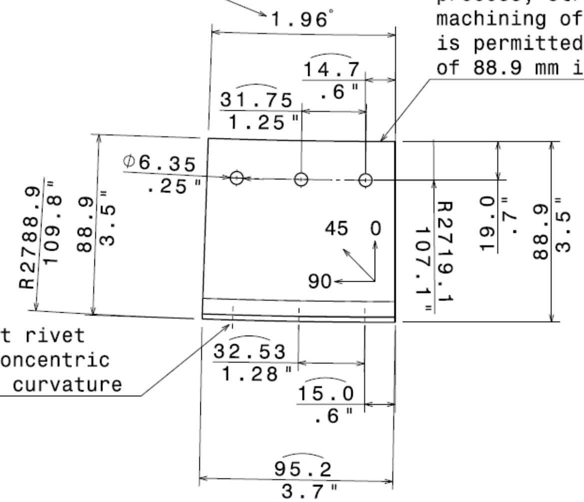

Front view

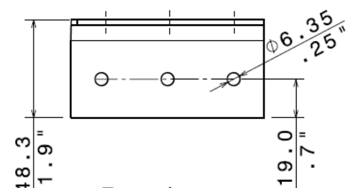

Top view

Layup:

Ply	Material	Thickness	Orientation
Ply01	X840 Z60 PW Fabric	~0.25	±45
Ply02	X840 Z60 PW Fabric	~0.25	0/90
Ply03	X840 Z60 PW Fabric	~0.25	±45
Ply04	X840 Z60 PW Fabric	~0.25	0/90
Ply05	X840 Z60 PW Fabric	~0.25	±45
Ply06	X840 Z60 PW Fabric	~0.25	0/90
Ply07	X840 Z60 PW Fabric	~0.25	0/90
Ply08	X840 Z60 PW Fabric	~0.25	±45
Ply09	X840 Z60 PW Fabric	~0.25	0/90
Ply10	X840 Z60 PW Fabric	~0.25	±45
Ply11	X840 Z60 PW Fabric	~0.25	0/90
Ply12	X840 Z60 PW Fabric	~0.25	±45

Nominal dimensions in mm.
All imperial units are indicative dimensions.
For manufacturing and tolerance purposes use nominal metric values.

PROJECT CODAMEIN RBH100672A

MIN. TOLERANCE unless otherwise specified: xx.x mm: ±0.5 mm xx.xx mm: ±0.1 mm

	DATE	NAME	SIGN.
DRAWN	01.06.11	Haase	
STRESS			
CHECKED	01.06.11	Mikulik	
APPROVED			

POS. | MODIFICATION | DATE | NAME

Bishop GmbH Aeronautical Engineers
D 22587 Hamburg Germany

SCALE 1:2 | WEIGHT -
MATERIAL X840 Z60 PW Fabric | Quantity 10

Shear Tie Half Length

SIZE A3 | DWG Nr. DBH 10001-005 | REV. C | ARCHIVE .
SUBSTITUTE FOR | SHEET 1 OF 1 | Catia V5

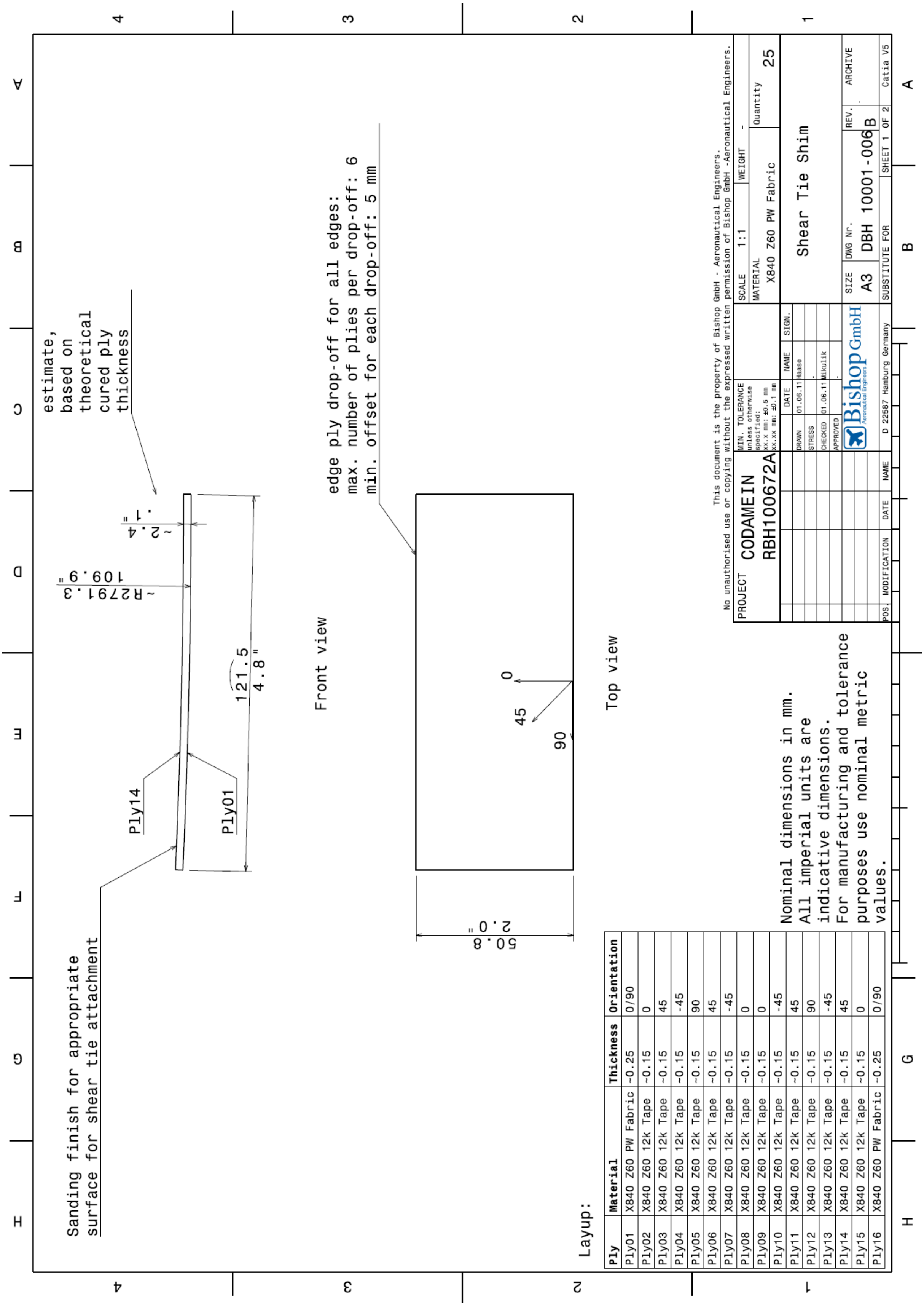

Ply	Material	Thickness	Orientation
Ply01	X840 Z60 PW Fabric	~0.25	0/90
Ply02	X840 Z60 12k Tape	~0.15	0
Ply03	X840 Z60 12k Tape	~0.15	45
Ply04	X840 Z60 12k Tape	~0.15	-45
Ply05	X840 Z60 12k Tape	~0.15	90
Ply06	X840 Z60 12k Tape	~0.15	45
Ply07	X840 Z60 12k Tape	~0.15	-45
Ply08	X840 Z60 12k Tape	~0.15	0
Ply09	X840 Z60 12k Tape	~0.15	0
Ply10	X840 Z60 12k Tape	~0.15	-45
Ply11	X840 Z60 12k Tape	~0.15	45
Ply12	X840 Z60 12k Tape	~0.15	90
Ply13	X840 Z60 12k Tape	~0.15	-45
Ply14	X840 Z60 12k Tape	~0.15	45
Ply15	X840 Z60 12k Tape	~0.15	0
Ply16	X840 Z60 PW Fabric	~0.25	0/90

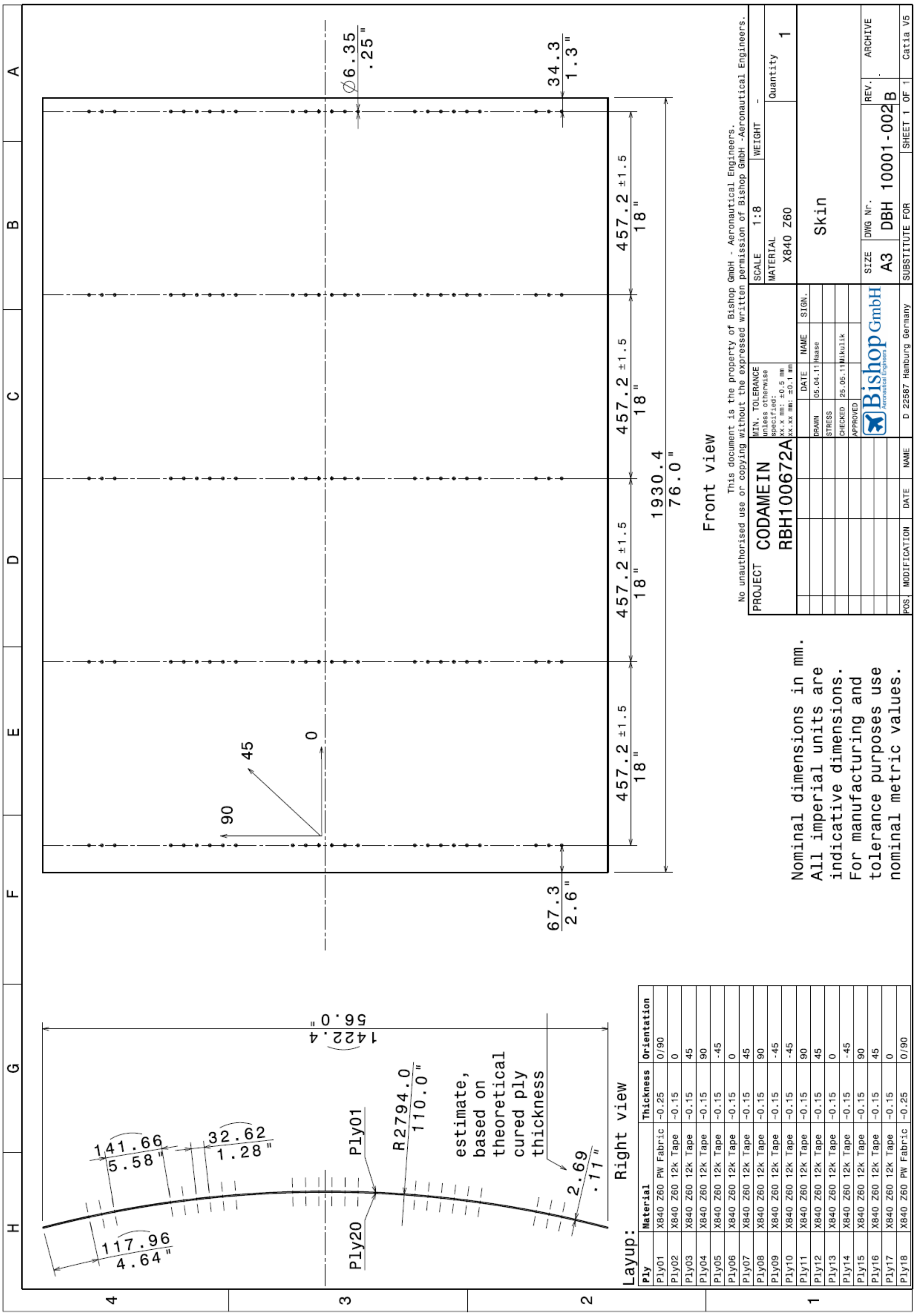

Layup:

Ply	Material	Thickness	Orientation
Ply01	X840 Z60 PW Fabric	~0.25	0/90
Ply02	X840 Z60 12k Tape	~0.15	0
Ply03	X840 Z60 12k Tape	~0.15	45
Ply04	X840 Z60 12k Tape	~0.15	90
Ply05	X840 Z60 12k Tape	~0.15	-45
Ply06	X840 Z60 12k Tape	~0.15	0
Ply07	X840 Z60 12k Tape	~0.15	45
Ply08	X840 Z60 12k Tape	~0.15	90
Ply09	X840 Z60 12k Tape	~0.15	-45
Ply10	X840 Z60 12k Tape	~0.15	-45
Ply11	X840 Z60 12k Tape	~0.15	90
Ply12	X840 Z60 12k Tape	~0.15	45
Ply13	X840 Z60 12k Tape	~0.15	0
Ply14	X840 Z60 12k Tape	~0.15	-45
Ply15	X840 Z60 12k Tape	~0.15	90
Ply16	X840 Z60 12k Tape	~0.15	45
Ply17	X840 Z60 12k Tape	~0.15	0
Ply18	X840 Z60 PW Fabric	~0.25	0/90

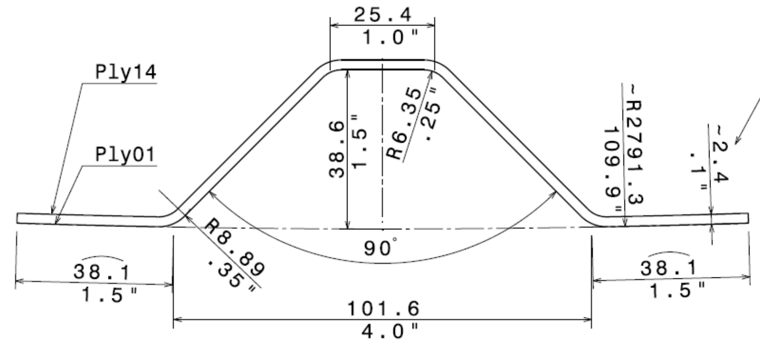

Front view

estimate, based
on theoretical
cured ply
thickness

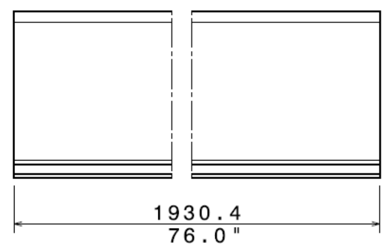

Left view

Edge ply drop-off for
stringer feet:
max. number of plies
per drop-off: 6
min. offset for each
drop-off: 5 mm

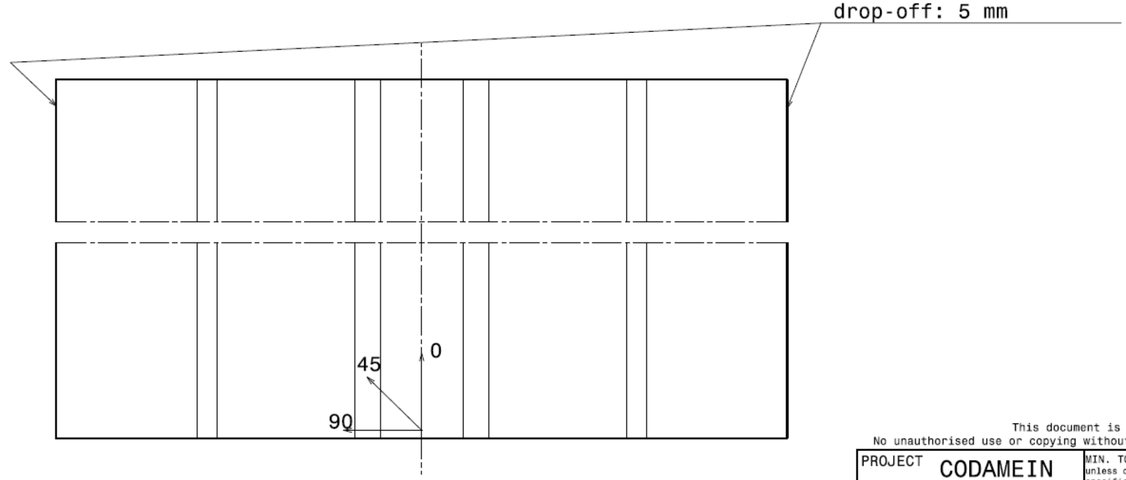

Top view

Layup:

Ply	Material	Thickness	Orientation
Ply01	X840 Z60 PW Fabric	~0.25	0/90
Ply02	X840 Z60 12k Tape	~0.15	0
Ply03	X840 Z60 12k Tape	~0.15	45
Ply04	X840 Z60 12k Tape	~0.15	-45
Ply05	X840 Z60 12k Tape	~0.15	90
Ply06	X840 Z60 12k Tape	~0.15	45
Ply07	X840 Z60 12k Tape	~0.15	-45
Ply08	X840 Z60 12k Tape	~0.15	0
Ply09	X840 Z60 12k Tape	~0.15	0
Ply10	X840 Z60 12k Tape	~0.15	-45
Ply11	X840 Z60 12k Tape	~0.15	45
Ply12	X840 Z60 12k Tape	~0.15	90
Ply13	X840 Z60 12k Tape	~0.15	-45
Ply14	X840 Z60 12k Tape	~0.15	45
Ply15	X840 Z60 12k Tape	~0.15	0
Ply16	X840 Z60 PW Fabric	~0.25	0/90

Nominal dimensions in mm.
All imperial units are indicative dimensions.
For manufacturing and tolerance purposes use
nominal metric values.

PROJECT CODAMEIN RBH100672A

MIN. TOLERANCE unless otherwise specified: xx.x mm: ±0.5 mm xx.xx mm: ±0.1 mm

SCALE 1:1 | WEIGHT - | MATERIAL X840 Z60 | Quantity 4

	DATE	NAME	SIGN.
DRAWN	01.06.11	Haase	
STRESS			
CHECKED	01.06.11	Mikulik	
APPROVED			

Omega-Stringer

Bishop GmbH Aeronautical Engineers D 22587 Hamburg Germany

SIZE A3 | DWG Nr. DBH 10001-003 | REV. B | ARCHIVE

POS. | MODIFICATION | DATE | NAME

SUBSTITUTE FOR | SHEET 1 OF 1 | Catia V5

REPORT

Department: Internal Projects	Report No.: PBH300261B
Analysis type: Non-linear Static Explicit Dynamic	Classification: Public

Subject: EASA.2010.C.13 CODAMEIN (Composite Damage Metrics and Inspection) Final Report

Summary: This report describes the outcomes of the EASA CODAMEIN project. The main objective of this research was to improve the understanding of high-energy low velocity blunt impact damage on hybrid composite-metallic aircraft structures. A five-frame, four-stringer panel was manufactured based on a review of the CS-25 fuselage designs and existing research of the University of California San Diego. The test panel was subjected to three load cycles whilst progressively increasing the maximum impactor displacement. Initialization of the damage occurred at the radius of the central shear tie and the associated failure initiation energy threshold was calculated to be 1270 J. With the subsequent load cycles widespread delaminations formed in several locations which consequently resulted in a severe loss of load carrying capacity of the panel and a sudden fracture of five shear ties. The outcome of this research demonstrated a potentially significant safety threat of high energy low velocity blunt impacts on composite aircraft fuselages, which may cause extensive internal structural damage without clear visual detectability from the external skin surface. Based on the findings of this research, recommendations for amending safety regulations for composite CS-25 fuselages are proposed.

Date: 12.03.2012	Prepared:	Checked:	Approved:	Archive:
	Z. Mikulik	P. Bishop	E. Isambert	Internal Projects\EASA CODAMEIN (RBH100672A)_RBH100672A\D_Documentation\1_Report
Signature				

Distribution		Issue:	Date:	N.Pages:	Changed pages:	Valid from/for:
P. Bishop	Bishop-GmbH	1.	28.11.2011	101		
Z. Mikulik	Bishop-GmbH	2.	31.01.2012	106	Changes addressed according to the EASA's comments	31.01.2012
P. Haase	Bishop-GmbH	3.	12.03.2012	106	Changes addressed according to the EASA's comments	12.03.2012
E. Isambert	EASA					
S. Waite	EASA					
E.B.Garcia Sanchez	EASA					

EUROPEAN AVIATION SAFETY AGENCY
AGENCE EUROPÉENNE DE LA SÉCURITÉ AÉRIENNE
EUROPÄISCHE AGENTUR FÜR FLUGSICHERHEIT

Postal address
Postfach 101253
50452 Cologne
Germany

Visiting address
Ottoplatz 1
50679 Cologne
Germany

Tel +49_221_89990-000
Fax +49_221_89990-999
Mail info@easa.europa.eu
Web easa.europa.eu